

**MULTISCALE NANOCOMPOSITES AND LAMINATES REINFORCED
BY CARBON NANOTUBES AND FIBRES**

by

Morné Zeeman

Submitted in fulfilment of the academic requirements of

Master of Science

in Mechanical Engineering

School of Engineering

College of Agriculture, Engineering and Science

University of KwaZulu-Natal

Durban

South Africa

July 2020

Supervisor: Prof. Sarp Adali

COLLEGE OF AGRICULTURE, ENGINEERING AND SCIENCE

DECLARATION 1 - PLAGIARISM

I, Morné Zeeman, declare that

1. The research reported in this dissertation, except where otherwise indicated, is my original research.
2. This dissertation has not been submitted for any degree or examination at any other university.
3. This dissertation does not contain other persons' data, pictures, graphs or other information, unless specifically acknowledged as being sourced from other persons.
4. This dissertation does not contain other persons' writing, unless specifically acknowledged as being sourced from other researchers. Where other written sources have been quoted, then:
 - a. Their words have been re-written, but the general information attributed to them has been referenced
 - b. Where their exact words have been used, then their writing has been placed in italics and inside quotation marks and referenced.
5. This dissertation does not contain text, graphics or tables copied and pasted from the Internet, unless specifically acknowledged, and the source being detailed in the dissertation and in the References sections.

_____ Date: 12 July 2020

Signed: Mr Morné Zeeman

As the candidate's supervisor I agree to the submission of this dissertation.

_____ Date: 05 August 2020

Signed: Prof. Sarp Adali

COLLEGE OF AGRICULTURE, ENGINEERING AND SCIENCE

DECLARATION 2 - PUBLICATIONS

The paper titled “Multiscale nanocomposites and laminates reinforced by carbon nanotubes and fibres” has been published in the Journal titled “Advances in Engineering Materials, Structures and Systems: Innovations, Mechanics and Applications”. The paper was also a part of the seventh international conference of Structural Engineering, Mechanics and Computation proceedings. I am the primary author of that paper and information in it overlaps with information in this dissertation. All results are obtained by me.

The paper titled “Effect of randomly and agglomerated nanotube reinforcements on the deflection of multiscale FRP composite laminates” is in preparation to be submitted. I am the primary author of that paper and information in it overlaps with information in this dissertation. All results are obtained by me.

Signed: Mr Morné Zeeman

Date: 12 July 2020

Acknowledgements

Firstly, thanks to Prof. Sarp Adali for his continued guidance and technical assistance.

Lastly, I would like to give special thanks to my mom, Adele Zeeman. Without her motivation and support I would never have been able to get to this stage; may you rest in peace.

Abstract

The addition of nanomaterials to conventional composites as reinforcement results in a new generation of composites, namely, multiscale composites. Multiscale composites comprise of reinforcements from two or more different length scales such as macro, micro and nano hence the name multiscale. Developing a computational modelling approach which analyses the flexural response of nanocomposites at the nanoscale, which is not restricted by time scales, would benefit future studies in the field of nanotechnology.

The dissertation details the analysis of carbon nanotube reinforced composites. The key focus areas include micromechanical modelling of both two and three phase nanocomposites along with their applications to structural elements. Furthermore, the flexural behaviour of a simply supported hybrid plate element subjected to a uniform transverse pressure is analysed under various conditions.

Firstly, both carbon and glass fibre reinforced composites are investigated along with a nanomaterial such as carbon nanotubes (CNT) to form a multiscale epoxy composite. Modelling techniques such as Mori-Tanaka and Halpin-Tsai approaches are furthered in order to investigate the mechanical properties of both two-phase and three-phase composites. The results obtained from these models are compared to theoretical and experimental results available in the literature.

Secondly, the material properties obtained are then used to investigate the bending behaviour of a CNT/fibre/polymer cross-ply laminate by incorporating micromechanical modelling techniques with structural mechanics. Numerical results are then obtained and used to study the effect of various problem parameters such as agglomeration, different fibre reinforcements, material layup and nanotube diameter.

The numerical results given in this study provides a quantitative analysis of the effects of different types of CNT parameters, fibre reinforcements and the volume fractions on the static behaviour of laminated composites.

Table of Contents

List of figures	iv
List of tables	vii
Nomenclature	viii
Acronyms and contractions	x
1. Introduction	1
1.1. Topic description.....	1
1.2. Background	1
1.3. Aims and objectives	2
2. Literature review.....	4
2.1. Carbon nanotubes.....	4
2.2. Carbon nanotube classification.....	7
2.3. Carbon nanotube’s structure	8
2.4. Synthesis of carbon nanotubes.....	11
2.4.1. Arc discharge method	12
2.4.2. Laser ablation method	14
2.4.3. Chemical vapour deposition approach	15
2.4.4. Methane decomposition synthesis method	18
2.4.5. Self-assembly of single crystals of SWCNTs	19
2.4.6. Carbon nanotube purification.....	19
2.5. Carbon nanotubes mechanical properties.....	20
2.5.1. Strength of carbon nanotubes	21
2.5.2. Carbon nanotube elastic properties	22
2.6. Computer simulation modelling techniques.....	23
2.6.1. Atomistic modelling	25
2.6.2. Continuum modelling.....	25
2.6.3. Nano-scale continuum modelling	27
3. Two-phase micromechanical analysis.....	29

3.1.	Material properties and considerations	30
3.2.	Carbon nanotube critical length and aspect ratio	32
3.3.	Reinforcement using straight, aligned carbon nanotubes.....	34
3.4.	Reinforcement using straight, randomly orientated carbon nanotubes	39
3.5.	Effect of agglomerated carbon nanotubes	43
3.6.	Chapter summary.....	50
4.	Three-phase micromechanical analysis	53
4.1.	Three-phase, aligned CNT micromechanical analysis.....	53
4.1.1.	Evaluating the engineering constants.....	54
4.1.2.	Results	56
4.2.	Three-phase, randomly orientated CNT micromechanical analysis	60
4.2.1.	Evaluating the engineering constants.....	60
4.2.2.	Results	62
4.3.	Effect of CNT agglomeration on the mechanical properties of hybrid nanocomposites	65
4.3.1.	Evaluating the engineering constants.....	66
4.3.2.	Results	68
4.4.	Chapter summary.....	71
5.	Three-phase composite structural application	74
5.1.	Notation and sign convention.....	75
5.2.	Plate theory.....	75
5.3.	Calculation of shear forces and moments	78
5.4.	Boundary conditions	80
5.5.	Plate analysis.....	81
5.6.	Results	83
5.7.	Chapter summary.....	96
6.	Discussion.....	97
7.	Conclusion.....	100

8. References.....	103
Appendix A.....	114
A.1.1. Reinforcement using straight, aligned carbon nanotubes on two-phase nanocomposites.....	114
A.1.2. Effect of carbon nanotube agglomeration on two-phase nanocomposites.....	115
A.1.3. Three-phase, randomly orientated CNT micromechanical analysis.....	117
A.1.4. Effect of nanotube agglomeration on the mechanical properties of three-phase hybrid composites.....	124
A.1.5. Fibre reinforced deflection contour for increasing reinforcement volume fraction (randomly orientated CNT).....	132
A.1.6. Effect of nanotube diameter on the mechanical properties of a reinforced structural element.....	135

List of figures

Figure 2-1: Carbon nanotube structure (Aqel et al. 2012).....	4
Figure 2-2: Carbon nanotube chiral vector (Amiot et al. 2008).....	6
Figure 2-3: SEM of multiple walled carbon nanotubes (Carbannonano 2018)	7
Figure 2-4: SWCNT and MWCNT typical dimensions (Roldo et al. 2013)	7
Figure 2-5: CNT unit cell and chiral vector (Quantopticon 2018)	9
Figure 2-6: Nanotube chirality (Ávila 2008)	10
Figure 2-7: TEM of MWCNT with internal cap (Harris 1999)	10
Figure 2-8: TEM of SWCNT bundle (Journet et al. 1997)	11
Figure 2-9: Carbon nanotube arc discharge physical synthesis method (Szabó et al. 2010).....	13
Figure 2-10: Laser ablation CNT synthesis method (Janas et al. 2016).....	14
Figure 2-11: Chemical vapour deposition method	16
Figure 2-12: Plasma assisted chemical vapour deposition (Cho et al. 2012).....	17
Figure 2-13: Microwave plasma enhanced chemical vapour deposition (Hassan et al. 2013)...	18
Figure 2-14: Methane decomposition fixed bed reactor system (Prasek et al. 2011)	19
Figure 3-1: Two-phase micromechanical modelling approach.....	30
Figure 3-2: Graph of interfacial shear strength vs nanotube diameter (Hassan et al. 2011)	33
Figure 3-3: Effective elastic moduli for composite with straight, aligned nanotubes	37
Figure 3-4: Effective Poisson's ratio for composite with straight, aligned nanotubes	38
Figure 3-5: Effective shear modulus for composite with straight, aligned nanotubes.....	38
Figure 3-6: Euler angles of randomly orientated, straight carbon nanotubes (Foroughi 2013). 39	
Figure 3-7: Randomly orientated carbon nanotube effective elastic moduli.....	42
Figure 3-8: Randomly orientated carbon nanotube effective Poisson's ratio	42
Figure 3-9: Randomly orientated carbon nanotube effective Shear modulus	43
Figure 3-10: Eshelby's cluster model of CNTs (Kamarian 2016)	44
Figure 3-11: Contour plot depicting the effect of nanotube agglomeration on the Young's modulus with respect to a uniformly distributed composite ($E_{\text{agglomerated}}/E_{\text{distributed}}$).....	48
Figure 3-12: CNT agglomeration effect on the composite longitudinal modulus	48
Figure 3-13: CNT agglomeration effect on the composite shear modulus.....	49
Figure 3-14: CNT agglomeration effect on the composite Poisson's ratio	49
Figure 3-15: Nanotube agglomeration versus elastic modulus	50

Figure 3-16: Randomly orientated CNT Young's modulus vs experimental data (Shokrieh et al. 2017)	51
Figure 4-1: Three-phase, aligned CNT modelling approach.....	54
Figure 4-2: Three-phase aligned nanocomposite effective longitudinal modulus	58
Figure 4-3: Three-phase aligned nanocomposite effective transverse modulus	58
Figure 4-4: Three-phase aligned nanocomposite effective shear modulus	59
Figure 4-5: Three-phase aligned nanocomposite effective Poisson's ratio	59
Figure 4-6: Micromechanical modelling of three-phase composite reinforced by randomly orientated CNTs and fibres	60
Figure 4-7: Three-phase randomly orientated nanocomposite effective longitudinal modulus	63
Figure 4-8: Three-phase randomly orientated nanocomposite effective transverse modulus..	64
Figure 4-9: Three-phase randomly orientated nanocomposite effective shear modulus.....	64
Figure 4-10: Three-phase randomly orientated nanocomposite effective Poisson's ratio	65
Figure 4-11: Micromechanical modelling approach of three-phase composites reinforced by agglomerated CNTs and fibres.....	66
Figure 4-12: Effect of nanotube agglomeration on three-phase longitudinal modulus.....	69
Figure 4-13: Effect of nanotube agglomeration on three-phase transverse modulus	70
Figure 4-14: Effect of nanotube agglomeration on three-phase shear modulus	70
Figure 4-15: Effect of nanotube agglomeration on three-phase Poisson's ratio.....	71
Figure 4-16: Conventional micromechanical approach vs experimental data	72
Figure 4-17: Modified micromechanical approach vs experimental data	73
Figure 4-18: Effect of nanotube agglomeration vs experimental data.....	73
Figure 5-1: Plate sign convention (Birman 2011).....	75
Figure 5-2: Kirchhoff plate bending (Saetta 1990).....	76
Figure 5-3: Plate notation (Saetta 1990).....	77
Figure 5-4: Stresses within a plate (Vidya-mitra 2018).....	79
Figure 5-5: Forces and moments within a plate (Vidya-mitra 2018)	79
Figure 5-6: Plate dimensions and notation.....	81
Figure 5-7: Plate with distributed load	83

Figure 5-8: Effect of nanotube diameter on the deflection at the centre of the plate (W_c) as a function of a pure epoxy plate in bending (W_0) on carbon fibre reinforced nanocomposites for increasing nanotube volume fraction	85
Figure 5-9: Effect of nanotube diameter on the deflection at the centre of the plate (W_c) as a function of a pure epoxy plate in bending (W_0) on glass fibre reinforced nanocomposites for increasing nanotube volume fraction	85
Figure 5-10: Deflection ratio plotted against CNT content for various fibre contents, randomly oriented CNTs.....	86
Figure 5-11: Deflection ratio plotted against CNT content for various fibre contents, agglomerated CNTs.....	87
Figure 5-12: Deflection ratio plotted against CNT content with and without agglomeration and with 30% carbon fibre content	88
Figure 5-13: Deflection ratio plotted against CNT content with and without agglomeration and 45% carbon fibre content	88
Figure 5-14: Deflection ratio plotted against CNT content with and without agglomeration and 60% carbon fibre content	89
Figure 5-15: Effect of nanotube agglomeration on glass fibre reinforced nanocomposites.....	89
Figure 5-16: Carbon fibre reinforced nanocomposites.....	90
Figure 5-17: Glass fibre reinforced nanocomposites.....	91
Figure 5-18: Fibre reinforced nanocomposite with various layups	92
Figure 5-19: Carbon fibre reinforced three-phase vs two-phase nanocomposite	93
Figure 5-20: Glass fibre reinforced three-phase vs two-phase nanocomposite.....	93
Figure 5-21: Carbon fibre reinforced deflection contour for increasing reinforcement volume fraction (randomly orientated CNT)	94
Figure 5-22: Glass fibre reinforced deflection contour for increasing reinforcement volume fraction (randomly orientated CNT)	94
Figure 5-23: Carbon fibre reinforced deflection contour for increasing reinforcement volume fraction with agglomeration	95
Figure 5-24: Glass fibre reinforced deflection contour for increasing reinforcement volume fraction with agglomeration	95

List of tables

Table 2-1: Differences between SWCNTs and MWCNTs (Loos 2014).....	8
Table 3-1: Mechanical properties of composite constituents (Smith et al. 1974).....	30
Table 3-2: Mechanical properties of carbon nanotubes (Al-Saleh et al. 2011)	31
Table 3-3: Randomly orientated CNT Young's modulus vs experimental data (Shokrieh et al. 2017)	52
Table 5-1 : Plate properties.....	84

Nomenclature

a_{c-c}	Distance between neighbouring atoms
\hat{a}	Unit vector
C	Effective elastic moduli
[C]	Stiffness matrix
C_h	Chiral vector
d	Outer diameter
d_{CNT}	Nanotube diameter
D_p	Flexural rigidity
d_i	inner diameter
D_{ij}	Bending stiffness
E_{11}	Elastic modulus
G	Shear modulus
K	Bulk modulus
k	Plane-strain bulk modulus normal to the fibre direction
l	Cross modulus
l_c	Critical length
m	In-plane shear modulus normal to the fibre direction
M	Moment
n	Uniaxial tension modulus in the fibre direction
nm	Nanometre
p	In-plane shear modulus parallel to the fibre direction
S	Eshelby's tensor

[S]	Compliance matrix
V	Volume
W_{CNT}	CNT weight fraction
α	Orientation factor
α_c	Critical aspect ratio
γ	Shear strain
ε	Direct strain
ε^o	Overall strain
ζ	Curvature fitting parameter
θ	Chiral angle
ν	Poisson's ratio
ρ	Density
σ^o	Overall stress
σ_{CNT}	Ultimate strength of the CNT
ζ	Geometric parameter
τ_{CNT}	Interfacial shear strength between the CNT and matrix
χ	Curvature

Acronyms and contractions

1D	One-dimensional
2D	Two-dimensional
3D	Three-dimensional
AFM	Atomic force microscope
CM	Continuum modelling
CNT	Carbon nanotubes
CNTFEC	CNT/ fibre reinforced epoxy composite
CVD	Chemical vapour deposition
DFT	Density functional theory
FEA	Finite element analysis
FEM	Finite Element Methods
LD	Local density
MC	Monte Carlo
MCNT	Matrix-carbon nanotube
MD	Molecular dynamics
MWCNT	Multiwalled carbon nanotube
NCM	Nano-scale continuum modelling
RoHM	Rule of Hybrid Mixture
RVE	Representative volume element
SWCNT	Single walled carbon nanotube
TBMD	Tight binding molecular dynamics
TEM	Transmission electron microscope

1. Introduction

This dissertation details the analysis of carbon nanotube reinforced composites. The key focus areas include micromechanical modelling of both two and three phase nanocomposites along with their applications to structural elements. Furthermore, the flexural behaviour of a simply supported hybrid plate element subjected to a uniform transverse pressure will be analysed under various conditions.

The dissertation begins with a review of current literature with emphasis placed on carbon nanotubes and popular modelling techniques. Next, micromechanical modelling techniques will be examined with consideration given to computational costs due to the nanoscale size of the analysis. Two-phase and three-phase multi-stage analyses will be performed to study the associated engineering constants. Once satisfactory results are attained and by comparing the data obtained to existing literature, the dissertation will be extended to a structural application. A composite plate reinforced with nanotubes and various fibres will be studied.

A nanoscale continuum modelling approach will be implemented to examine the deformation of the nanocomposite. Factors such as nanotube diameter and volume fraction, fibre type and orientation, laminate layup and nanotube agglomeration effects will be investigated throughout the dissertation.

1.1. Topic description

Carbon nanotubes possess advantageous properties for high-strength low-density applications which make them ideal for material reinforcement. Therefore, the research in this dissertation is geared towards improving material reinforcement and more specifically towards elements such as plates which are commonly used in fields where the much sought-after material properties possessed by carbon nanotubes are often required. A solution to the problem where conventional composites and traditional materials often fall short is to develop tailor made materials for problem specific solutions. As such a composite reinforced with both fibre and carbon nanotubes are suggested and due to the high cost of performing such an analysis experimentally and at an atomistic scale, conventional computational approaches need to be modified and implemented.

1.2. Background

More and more composite materials are being utilised in engineering applications as they offer improved mechanical properties such as stiffness and strength without incurring extra weight

as compared to their metallic equivalents. This can prove to be advantageous as it allows for tailored designs for problem specific applications. Properties such as carbon nanotube content, fibre direction and layering can be manipulated to achieve the optimal material properties for the given demands.

Composite materials are especially of interest as they offer high strength-to-mass ratios, and with the progression of technology and science it has stretched to the field of nanomaterials. The development of carbon nanotube-based structures requires a good understanding of carbon nanotubes' properties. An important first step in analysing the development of structural composites would be to perform an accurate assessment of the flexural behaviour of two-phase nanocomposites. The assessment of nanocomposite mechanical properties such as buckling resistance, tensile strength and elastic modulus presents challenges to academics in nano-mechanics as a result of their particularly small size. Problems associated with the experimental analyses include high manufacturing and testing costs as well as technological difficulties when attempting to manipulating nanometre-sized objects. Researchers have since looked to employing computational methods for modelling the behaviour of nanostructures. Hence, there is a need for developing a modelling approach which analyses the flexural response of nanocomposites at the nanoscale which is not restricted by time scales. Such a modelling technique would benefit the industry in understanding, designing and analysing nanotechnology.

1.3. Aims and objectives

The objective of the dissertation is to model both two-phase and three-phase nanocomposites and to apply the information obtained to a structural element such as a laminate plate by incorporating micromechanical modelling techniques with structural mechanics. To gain a better understanding of hybrid composites and their applications, the following objectives are defined:

- Research carbon nanotubes
- Research computer simulation modelling techniques for the purpose of analysing nanotubes
- Analyse two-phase nanocomposites using micromechanical techniques
- Develop computational models for two-phase nanocomposites to analyse the engineering constants
- Analyse three-phase nanocomposites using micromechanical techniques

- Analyse the effects of nanotube orientation and agglomeration on both two and three-phase nanocomposites
- Compare results obtained from two and three-phase analyses to experimental data
- Research composite plates
- Develop computational models for the purpose of analysing the flexural behaviour of hybrid composite plates
- Analyse the impact of various factors such as nanotube diameter and agglomeration for increasing nanotube volume fraction
- Discuss the effectiveness of using three-phase nanocomposites

2. Literature review

Carbon nanotubes (CNTs) have rapidly evolved over the years since their discovery by Iijima et al. (1993). Since then CNTs have been the focus of substitution material in fields of study such as material reinforcement, electronics, electronic transport, elasticity, chemical sensing, drug delivery and vibration analyses in both the practical and theoretical fields (Saito et al. 1998). The following literature review presents some of the current research relating to carbon nanotubes and their application to composite structures.

2.1. Carbon nanotubes

Composite materials have developed over the years to establish itself as a worthy alternative to traditional materials. Composite materials possess unique mechanical, electrical and chemical characteristics which can be altered for specific scenarios. Composite materials generally consist of at least two constituent materials to form a reinforcement and matrix, both of which can vary types and ratio. The application usually dictates the composite material required as a variety of properties can be obtained by altering the composite constituents.

Nanotechnology has widened the scope and possibilities in the composite field. Nanocomposites make it possible to control the material properties at not only a micro and macroscopic level but now at a nanoscale. CNTs make it possible to reach even higher strength-to-mass ratios through structural reinforcement. The outstanding characteristics made available by CNTs is as a result their atomic-structure, which can be visualised as graphene sheets that have been rolled into cylindrical shapes and capped at the ends as seen in Figure 2-1 (Ray et al. 2002).

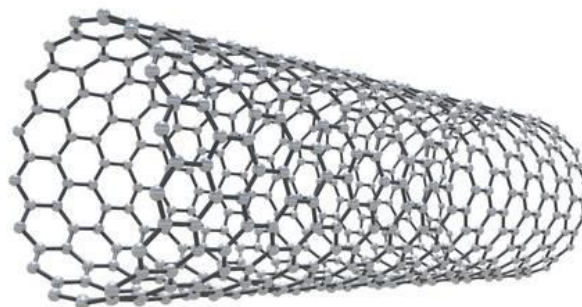


Figure 2-1: Carbon nanotube structure (Aqel et al. 2012)

Since their discovery, CNTs have been the primary focus of substitution materials in fields of study ranging from medical to aeronautical for both theoretical and practical considerations. Carbon nanotube's phenomenal physical properties are due to their near perfect microstructure. Their properties attract numerous researchers' interest for their plausibility in many advanced technological applications. Carbon nanotube density is found to be half that of aluminium, transmit heat twice as well as pure diamond, have current carrying capabilities 1000 times that of copper and have tensile strengths twenty times that of high-strength steel alloys (Collins et al. 2000). Also, CNTs are found to be more stable at higher temperatures compared to metal wires when used in microchips (Dekker 1999). Due to their strong covalent bonds between in-planar carbon atoms, the desired high-strength low-density property of the nanotube reinforced composite can be achieved.

Graphene sheets are two-dimensional arrangements of carbon atoms packed in a hexagonal arrangement. Each atom is attached to 3 neighbouring atoms through sp^2 hybridised orbitals at 120° to each other. The sp^2 orbitals form strong, covalent σ -bonds between the atoms in the graphene plane, whereas the remaining orbitals normal to the graphene plane form weak van der Waals bonds with neighbouring graphene planes. The cylinders forming CNTs are typically closed at each end with hemispherical caps, the curvature of which is created by the addition of pentagons to the hexagonal lattice. Properties of CNTs hinge on the atomic arrangement, length, diameter, and the nanostructure of the nanotube (Ray et al. 2002).

Previous studies on CNTs have predicted tensile moduli around 1 TPa and elastic strains of 5% (Wuite 2005). Despite the difficulties associated with manipulating objects on the nanoscale, experimental results have been obtained verifying the predicted material properties. Experimentally, to contest the properties of traditional materials, only a low volume fraction of nanotubes is needed. Additionally, increasing the volume fraction of CNTs may result in a nanocomposite with improved stiffness and strength ratios which are unachievable with conventional composites. Both scenarios allow for a substantial decrease in weight, making it ideal for weight-critical applications. As a result of their increased modulus-to-weight and strength-to-weight ratios, research performed by NASA (2015) have shown that single-walled carbon nanotube (SWCNTs) composites could reduce the overall weight of a spacecraft by more than 50%. Additional benefits of carbon nanotube-reinforced composites are not only structural but an increase in the working temperature range can also be achieved as well as the electrical conductivity and thermal stability of the composite can also be manipulated using nanotubes. This multi-functionality of CNTs allows for designs to meet both primary

material specifications as well as secondary material property requirements. Another benefit offered by nanotubes over traditional composites is that they can be manipulated at a nanoscale in the manufacturing process which allows for more flexibility in the shape of the product as well as the production rate. The nanoscale size also allows for reinforcement in the out of plane direction of a composite shell (Wuite 2005).

A variety in isomers can be obtained in the graphene sheet based on how it is rolled. The angle at which the graphene sheet is rolled is called the nanotube chirality, represented by the chiral-angle, θ , and the chiral-vector, C_h , as shown in Figure 2-2.

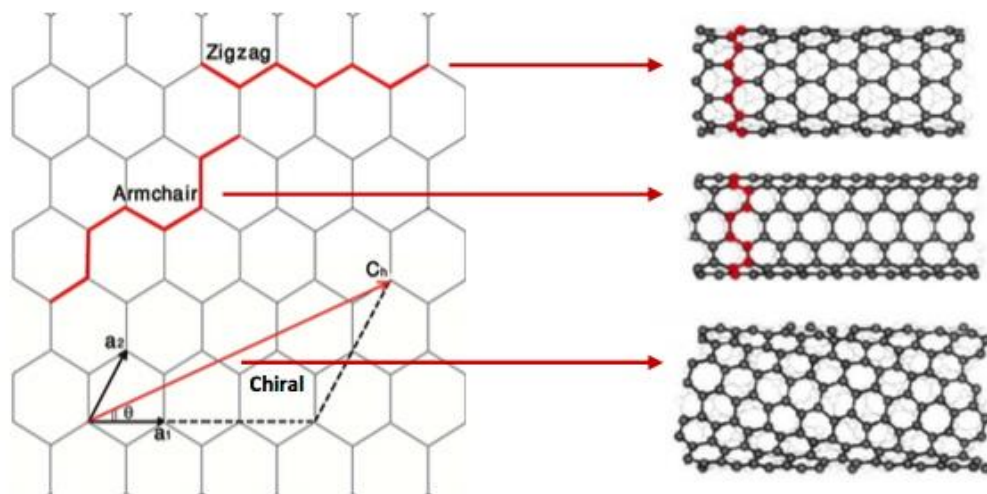


Figure 2-2: Carbon nanotube chiral vector (Amiot et al. 2008)

Additionally, carbon chains consist of covalently bonded molecules which results in a structure with both high electrical conductivity and specific thermal ratios. Manufacturing nanostructures into long fibres does however presents some difficulties and thus has limited these fibres to just being matrix modifiers. Due to their size, nanotubes inherently tend to group into bundles therefore resulting in a heterogenous material. Nanotubes provide a large surface area within a matrix as seen in Figure 2-3. This normally results in poor adhesion between the nanofibers and matrix, creating a nanocomposite which tends to be viscous and not easy to shape. On the other hand, the increased surface area of CNTs can also pose some beneficial characteristics that can be utilised. As an example, their high aspect ratios together with their increased surface area serves as a mechanical strengthening characteristic. CNTs can also be arranged in a 3D array; this results in improved material properties in all planes. There are concerns related to the matrix-nanotube bonding which have resulted in some challenges which will need to be addressed before making these nanocomposites readily available and cost effective (Wuite 2005).

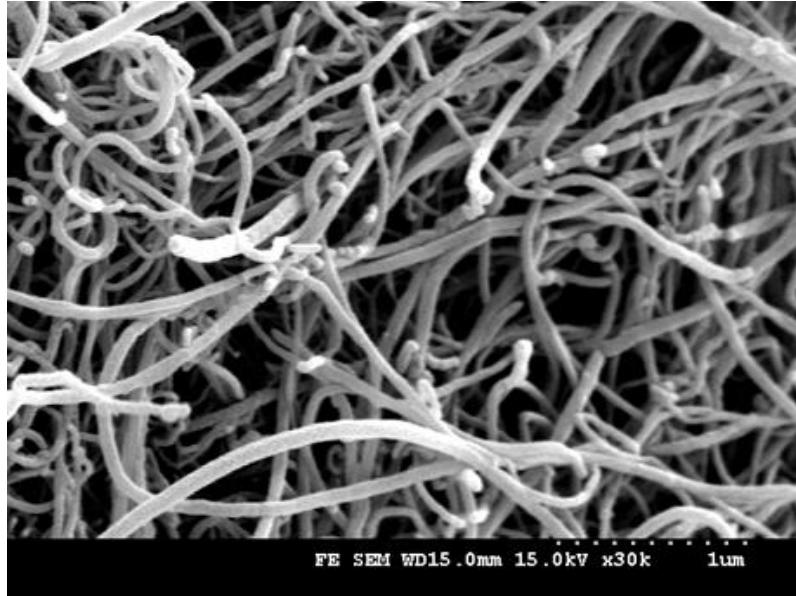


Figure 2-3: SEM of multiple walled carbon nanotubes (Carbonnano 2018)

2.2. Carbon nanotube classification

Classification of CNTs are typically based on the number of graphene layers present, being:

- Single-walled carbon nanotubes (SWCNTs), and
- Multiple-walled carbon nanotubes (MWCNTs)

SWCNTs consist of a single graphite layer, shaped into a cylinder. Usually SWCNT diameters are around 1 nm as seen in Figure 2-4, while the lengths are often in the order of 10 nm. The dimensions of the SWCNTs are usually dependant on the fabrication method used to produce the CNTs (Saito et al. 1998).

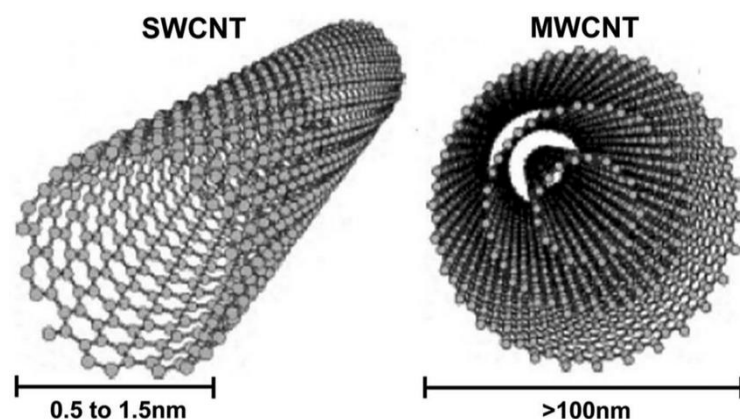


Figure 2-4: SWCNT and MWCNT typical dimensions (Roldo et al. 2013)

MWCNTs are composed of concentric SWCNTs coupled together through van der Waals forces resulting in a multi-layered structure (Figure 2-4). The interlayer spacing between the

individual shells is approximately 0.34 nm, which closely resembles the interlayer separation of graphite, 0.335 nm (Roldo et al. 2013). The diameter, usually in the range of 100 nm, as well as the number of shells is again dependant on the fabrication technique used to produce the nanotubes. As can be seen in Table 2-1, a change in the number of graphene layers results in unique and customisable material properties for both MWCNTs and SWCNTs.

Table 2-1: Differences between SWCNTs and MWCNTs (Loos 2014)

SWCNT	MWCNT
Single graphene layer	Multiple graphene layers
Catalyst required	No catalyst required
Bulk synthesis is difficult as it requires proper control over growth and atmospheric condition	Bulk synthesis is easy
Poor level of purity	High levels of purity can be achieved
Increased defect rate	Decreased defect rate, however once a defect is present it becomes increasingly difficult to improve
Less accumulation	More accumulation
Characterisation is simple	The complex structures make it difficult to evaluate
Easy to work and shape	Not easy to work and shape

Other ways of classifying CNTs are according to their orientation (randomly orientated or aligned) as well as the structure of the nanotube which will be discussed in the next segment.

2.3. Carbon nanotube's structure

The strength of the C-C bonds found within CNTs as well as the likelihood of a defect-free structure, has resulted in hypotheses that CNTs may reach the theoretical bounds for material properties, including tensile strength and axial stiffness. Improved toughness and strain rates as well as control over thermal and electrical properties are additional benefits associated with the use of CNTs as a reinforcement material. The sp^2 bonds present in CNTs, where each atom is connected to three neighbouring atoms, which is stronger than the sp^3 bonds found in diamonds, provides the CNT molecules with their unique strength. Under high pressures, CNTs have the ability to merge, exchanging sp^2 bonds for sp^3 bonds (Saito et al. 1998). This allows for the option of producing robust and long nanotubes through high pressure nanotube linking.

The outstanding properties that are predicted for CNTs are the result of their structure. As seen in Figure 2-5, the geometry of a CNT is best described by the unit cell of the CNT due to the variety of angles in which the hexagonal lattice can be manipulated. The atomic arrangement of the CNT is best described by the chiral vector as follows:

$$C_h = n\hat{a}_1 + m\hat{a}_2 \quad (2.1)$$

Where \hat{a}_1 and \hat{a}_2 are unit vectors on the hexagonal lattice and m and n are integers. We can then therefore determine both the diameter (d_{CNT}) and chiral angle (θ) of the CNT as:

$$\theta = \tan^{-1}\left(\frac{3n}{2m+n}\right) \quad (2.2)$$

and,

$$d_{CNT} = \frac{3}{\pi} a_{c-c} \sqrt{m^2 + mn + n^2} \quad (2.3)$$

Where the distance between neighbouring carbon atoms in a graphene sheet is represented by a_{c-c} , this is approximately 0.142 nm as studied by Harris (1999). As shown in Figure 2-6, different atomic configurations result in different nanotube chiral vectors (n,m), therefore the chiral angle can be used to define the three major categories of nanotubes:

- $\theta = 30$, "Arm Chair"
- $0 < \theta < 30$, "Chiral"
- $\theta = 0$, "Zigzag"

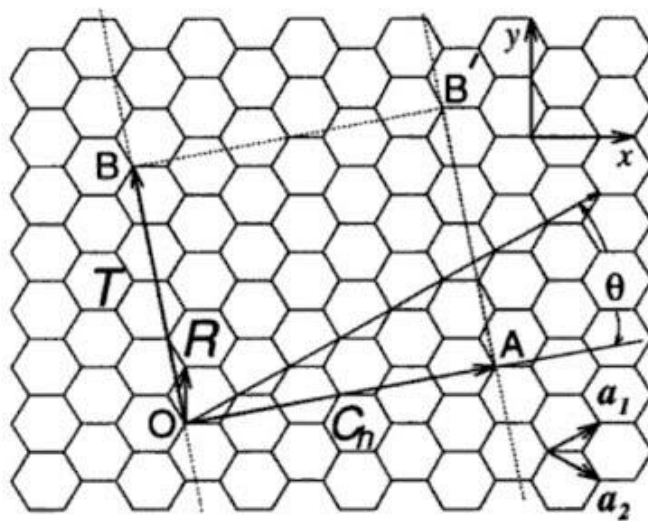


Figure 2-5: CNT unit cell and chiral vector (Quantopticon 2018)

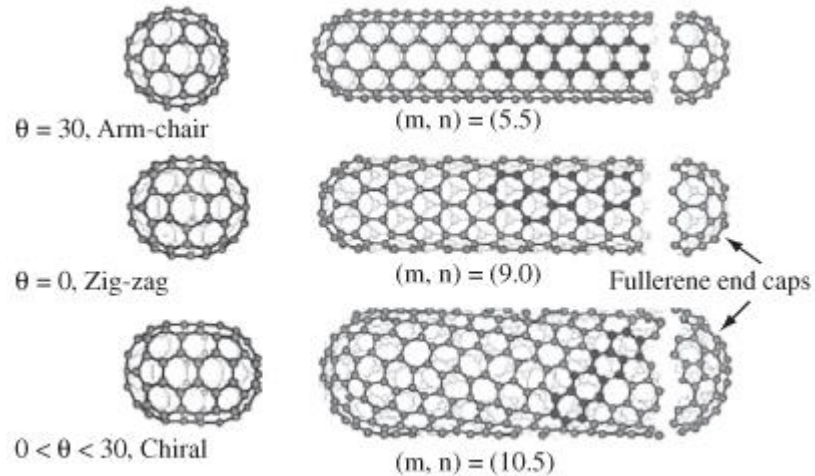


Figure 2-6: Nanotube chirality (Ávila 2008)

The CNT chirality has been found to strongly influence certain CNT properties, including fracture behaviour and electrical resistivity. For example, a metallic CNT chiral vector will satisfy the equation $n - m = 3q$, where q represents an integer and all remaining CNTs are semi-conductive (Harris 1999). Pan (2000) found that the CNT stiffness is relatively independent of the chirality.

A high-resolution transmission electron microscope (TEM) visualisation of a MWCNT is shown in Figure 2-7. The spacing between the individual shells is approximately 0.34 nm, similar to that of graphene sheets (Harris 1999). The diameter and number of shells of MWCNTs depends heavily on the production method used. Pan et al. (1999) have reported diameters on the order of 30 nm. A TEM image of a SWCNT array is shown in Figure 2-8, where the array comprise of about 20 SWCNTs with similar diameters, packed in a triangular lattice. The average spacing between tubes and average tube diameter in the bundle are found to be 1.7 nm and 1.4 nm respectively (Journet et al. 1997).

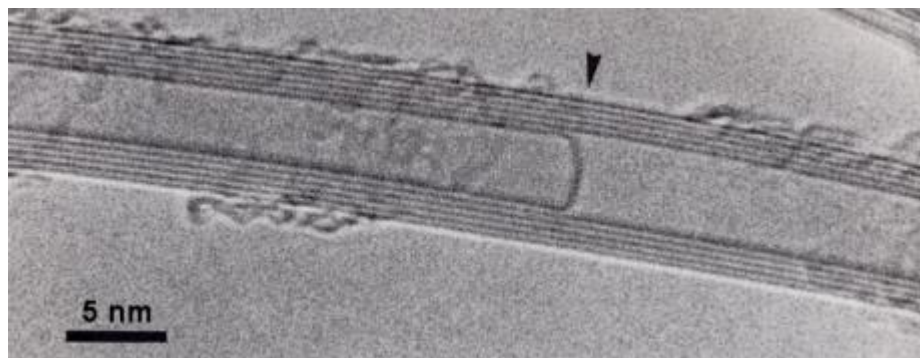


Figure 2-7: TEM of MWCNT with internal cap (Harris 1999)

While not taken into consideration in this dissertation, clear differences in the mechanical behaviour of various CNT forms will need to be investigated in future models. For the sake of structural reinforcement, ideal behaviour will depend on the load transferring capabilities between the CNTs and matrix. It should be noted that SWCNTs are vulnerable to buckling as a result of their very small cross-sections, in contrast Yu (2004) found that MWCNTs experience interlayer sliding due to the lack of inter-tube bonding and this might hinder the load transferring capabilities between the phases.

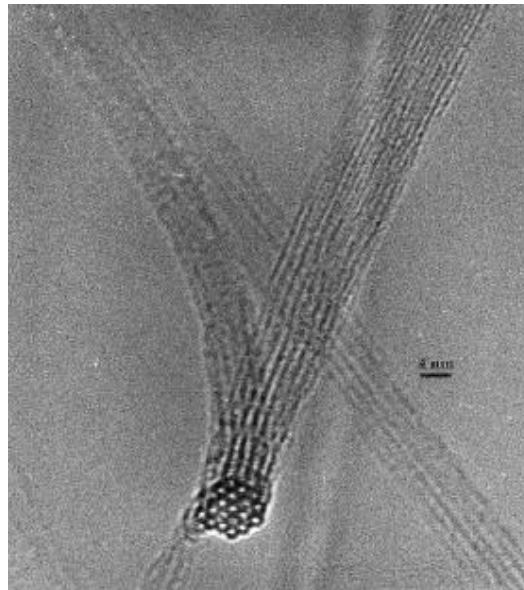


Figure 2-8: TEM of SWCNT bundle (Journet et al. 1997)

2.4. Synthesis of carbon nanotubes

In 1991, the arc-discharge method introduced MWCNTs to the field of nanotechnology. The nanotubes were extremely long, thin and consisting of pure SWCNTs tubes. Through the use of a metal catalyst, MWCNTs were first produced in 1996 (Roldo et al. 2013). Bundles of SWCNTs were initially produced through the use of Laser ablation. Soon after, chemical vapour disposition technique was utilised for the catalytic growth of MWCNTs. With recent increase in the popularity of carbon nanotube reinforcement, numerous approaches have since been established to synthesise nanotubes with more desirable properties. Since the purpose of the dissertation is to focus on carbon nanotube reinforcement, an overview of the manufacturing techniques available are provided to better understand the advantages and disadvantages associated with different CNT manufacturing processes. Understanding the way in which CNTs are produced is key as this will lay the foundation in creating composites with consistent material properties for both experimental and theoretical analyses.

An overview of both physical and chemical methods is considered below, these include chemical vapour deposition, arc discharge, and laser ablation methane decomposition and the self-assembly of single crystals of SWCNTs.

The advantages and shortcomings of each technique is looked at with focus being placed on the feasibility, possible implementation for mass production, control over fibre direction, fibre concentration, structural defects and the mechanical properties of the carbon nanotubes. Furthermore, CNT purification will be considered to purify the nanoparticles from any imperfections and/ or contaminants through post processing.

2.4.1. Arc discharge method

As seen in Figure 2-9, the Arc discharge method was commonly used to synthesise a variety of carbon-based materials in the past, such as carbon whiskers and soot. It has since been modified and developed to synthesise CNTs. The nanotube properties are determined by the pressure and type of gas surrounding the arc inside of the chamber (Dresselhaus et al. 2000).

The process involves generating an arc via DC current through the use of two carbon electrodes. The electrodes are immersed in an inert gas (e.g. Helium), inside of a vacuum chamber for the purpose of increasing the speed of carbon deposition. The process starts off by keeping the two electrodes apart while the chamber pressure stabilised after which the 20V power supply is turned on. The electrodes are gradually brought closer together until an arc is induced. Upon arcing the electrodes would form a plasma and once the arc stabilised (at approximately 1 mm part) the CNTs would deposit on the negatively charged electrode. The power would then be turned off, and the chamber left to cool once desired nanotube lengths are reached. The two most crucial parameters to control in this process are (Dresselhaus et al. 2000):

1. The current arcing, and
2. The inert gas pressures.

Good CNT yield is obtained for inert gas pressures of around 500 torr (Dresselhaus et al. 2000). Increasing or decreasing the pressure could change the yield and quality of CNTs and in some instances result in no formation of any CNTs. Generally, the yield would consist of MWCNTs riddled with impurities such as non-tubular fullerenes and amorphous carbon. Furthermore, a purification step is recommended to separate the nanotubes. Doping the electrodes with metallic elements results in the production of SWCNTs.

The advantages associated with this method is that both the microscopic and the macroscopic structures are well aligned with one another. This results in the synthesis of good quality SWCNTs with well controlled aspect ratios. Long MWCNTs of high quality with diameters between 2 and 100nm are possible. The MWCNTs synthesised through the use of this method are held together by van der Waals forces and are also highly crystalline. Whereas, SWCNTs with diameters of approximately 1 nm can be synthesised.

Bethune et al. (1993) used a carbon anode, containing cobalt catalyst, to synthesise SWCNTs in soot material. This method however, generates extremely high temperatures in the range of 3700°C. Factors such as current flow, gas pressure, electrode cooling and the distance between electrodes heavily influences the structure and shape of the deposit. Also, besides nanotubes, there is an abundance of carbonaceous sheets in the deposit. Bethune et al. (1993) conducted an experiment using carbon anodes alongside Fe, Co and Ni as catalysts to synthesise CNTs with currents ranging between 95A and 105A with helium pressures ranging between 100 and 500 Torr. TEM was used to analyse SWCNTs and diameters of $1.2 \pm 0.1\text{nm}$ were obtained with the use of cobalt catalysts (Bethune et al. 1993).

Carbon nanotubes from arc discharge method possess a set of challenges that need to be overcome before this method can be implemented as a practical solution for synthesising well-tailored CNTs. The limiting factor of this technique is the low production yields, making the technique unable to satisfy the high production rate needed for nanotube-reinforced composite applications. Recently studies involve CNTs that have been produced using arc-discharge method in open air to try and increase the yield of nanotubes.

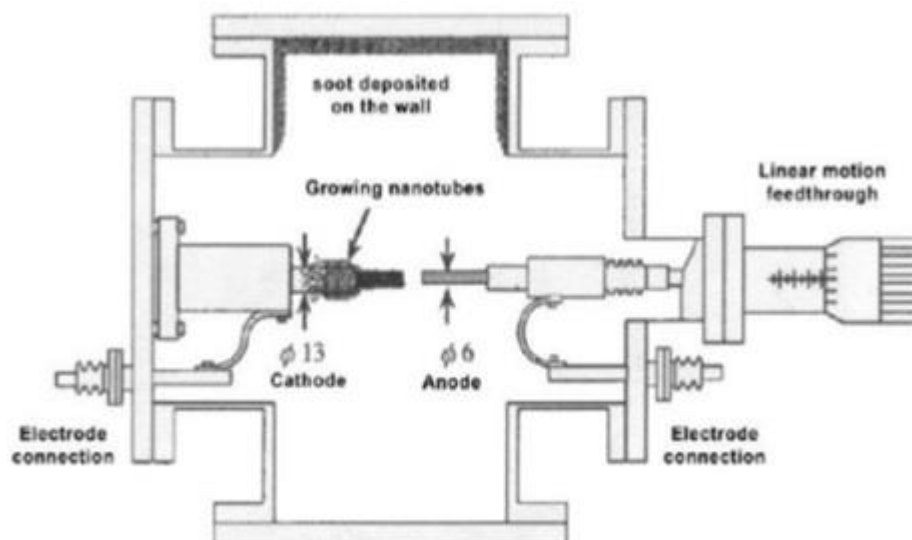


Figure 2-9: Carbon nanotube arc discharge physical synthesis method (Szabó et al. 2010)

2.4.2. Laser ablation method

Smalley and co-workers first discovered laser ablation who then derived the method from the arc discharge method (Purohit et al. 2014). This method utilises a catalyst under high temperature to ablate a carbon target with laser pulses. Furthermore, a surrounded inert gas such as Helium is utilised, acting as a carrier of the carbon deposit to the collector which highlights the main difference from the arc discharge method as seen in Figure 2-10. The temperatures needed in laser ablation are in the range of 1200°C, which is lower than that of the arc discharge method. A tangled mat of nanotubes is deposited on a water-cooled surface. The collected tubes consist of 5 to 20 nm in diameter CNT bundles which are tens to hundreds of microns in length (Purohit et al. 2014).

The graphite target is doped with a catalyst such as nickel or cobalt to increase the yield of SWCNTs. However, as with the arc discharge method impurities such as non-tubular fullerenes, unstructured carbon and catalyst particles are synthesised along with the carbon nanotubes thus additional purification is needed to rid the nanotubes of impurities. This method is also very costly, so it is therefore aimed at producing SWCNTs. Laser ablation yielded more SWCNTs with a narrower size distribution than that which was synthesised by the arc discharge method, although the overall production rates are still unsuitable for mass production (Purohit et al. 2014).

In summary the parameters that limit the yield of CNTs for laser ablation method are:

- The type and quantity of catalyst
- The laser wavelength and power
- The nature, pressure and temperature of inert gas
- The fluid dynamics in the chamber

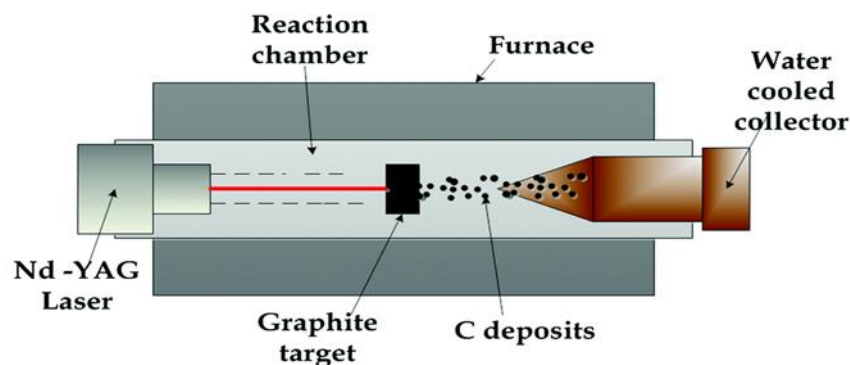


Figure 2-10: Laser ablation CNT synthesis method (Janas et al. 2016)

Terrones et al. (2000) found that by incorporating a cobalt coated silica plate, it aided in the alignment and growth of nanotubes, thus allowing for control of both nanotube length (approximately 50 μm) and diameter (approximately 30-50 nm).

In conclusion, laser ablation of CNTs involve solid carbon sources evaporating and yielding carbon atoms. The temperatures involved are close to the melting point of graphite as studied by Dresselhaus et al. (2000). Therefore, low production rates and high production costs have made mass production of CNTs difficult using laser ablation.

2.4.3. Chemical vapour deposition approach

Chemical vapour deposition (CVD) method is a technique commonly utilised in manufacturing of powders, fibres and coatings. CVD can be used to synthesise both non-metallic and metallic elements, in particular carbon. The nanotubes are produced by providing an energy source to the hydrocarbons, reactive radical species are generated from the imparted energy which breaks the molecule down. Temperatures ranging between 550°C and 750°C are experienced. A heated substrate, coated in a catalyst (typically Co, Ni or Fe), is then used to gather these reactive species, thus resulting in the formation of CNTs (Francisco 2010).

Ethylene, Methane and acetylene are commonly used as hydrocarbon sources. Resistive heating and electron beams are the commonly used energy sources. CNTs of up to 50 μm in length can be synthesised. Acetylene catalytic decomposition over iron particles at 700°C is used to produce the synthesised materials (Vajtai 2013).

Iron nanoparticles are utilised as a catalyst for high volume production of aligned nanotubes. The CVD method using microwave energy was developed for the production of MWCNTs using cobalt as the catalyst and acetylene as the hydrocarbon. MWCNTs produced using this combination had a diameter of approximately 25 nm which comprised of approximately 26 layers. Thermal CVD and radio frequency plasma enhanced CVD (RF PECVD) have since been studied further (Azam 2017), where an acetylene and hydrogen gas mixture are used to synthesise CNTs on a stainless-steel plate.

CVD technique, using a gas-phase catalyst (Figure 2-11) to control the orientation of CNTs made it possible to form them into either 1, 2, or 3D arrangements. This is especially useful in the manufacturing of electro-mechanical devices. The gas-phase CVD technique is typically performed in two steps.

Firstly, a catalyst is deposited on substrate after which the nucleation of the catalyst is performed via thermal annealing or chemical etching. An energy source is then used to break down a carbon source to an atomistic level. The carbon molecules gather on the metallic catalysts which aid in the synthesis of CNTs. Typical carbon source used are acetylene, methane or carbon monoxide.

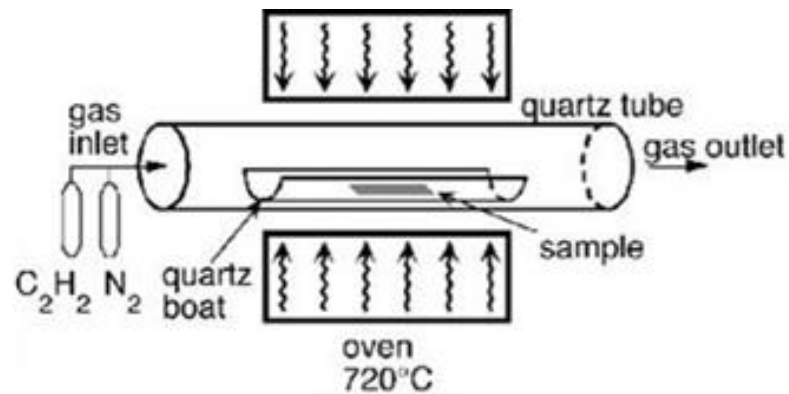


Figure 2-11: Chemical vapour deposition method

The parameters that affect the synthesis of nanotubes are:

- The temperature,
- type of hydrocarbons, and
- the catalysts used.

It was observed that MWCNTs and by altering the catalyst, SWCNTs of diameter 0.65 nm can be synthesised at a temperature of around 660°C. As the temperature increases then so does the density and growth rate of nanotubes. Alignment is also obtained through increasing the temperature (Saifuddin et al. 2012).

Although the CVD technique provides accuracy to the nanometre, a high defect rate is observed in the production of MWCNTs, this is due to the lack of thermal energy.

Comparing the three approaches, the laser-ablation and arc-discharge techniques produce increased volumes (>70%) and quality of nanotubes. However, the costs associated with the arc-discharge approach was considerably less expensive. The shortcomings associated with these approaches are (Saifuddin et al. 2012):

1. CNTs are tangled which makes the application and purification of them difficult.
2. Temperatures >3000°C are required in order to evaporate the carbon atoms.

The production of straight, aligned CNTs has been accomplished on multiple substrates through the use of plasma enhanced chemical vapour deposition (PECVD) (Saifuddin et al. 2012). A nickel coated catalyst and high-purity ammonia as the catalytic gas is used. A DC power supply generates the required plasma with acetylene being used as a carbon source. A carbonised tungsten filament is used to assist with the dissociation of the reactive gasses. The growth time and temperature are manipulated to control the nanotube length and graphitisation. The use of a direct current plasma showed controlled tube growth parallel to the plasma. Lastly, nanotube diameters are controlled through altering the catalyst layer thickness. The control over the alignment and diameter of nanotubes produced using PECVD represented in Figure 2-12 (Saifuddin et al. 2012).

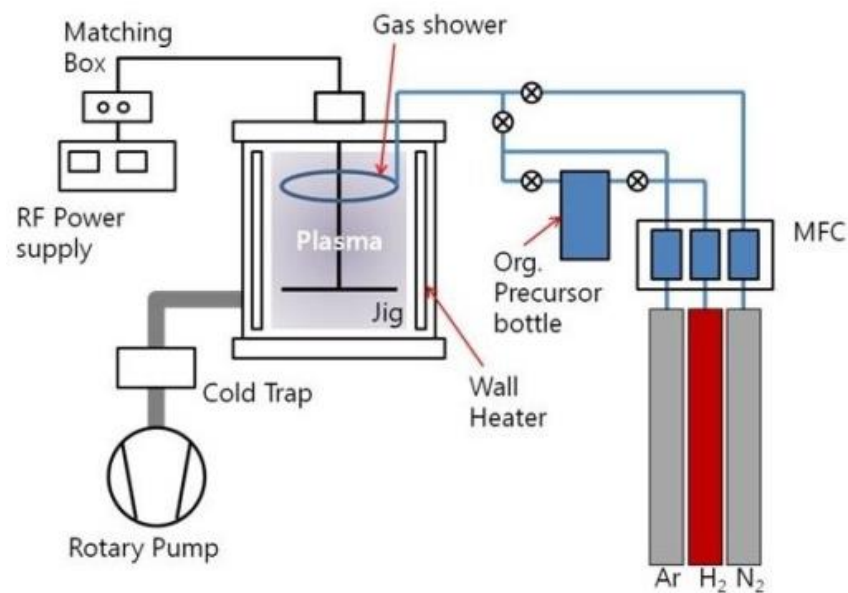


Figure 2-12: Plasma assisted chemical vapour deposition (Cho et al. 2012)

Microwave plasma enhanced chemical vapour deposition (MPECVD) is utilised to synthesise nanotubes perpendicular to the surface of the substrate (Saifuddin et al. 2012). The plasma is excited through the use of a varying micro-wave which imposes a self-bias thus resulting in nanotube growth normal to the surface of the substrate. Synthesising under plasma enhancement was shown to be forty times quicker than the growth rate under thermal CVD. Figure 2-13 depicts the structure and alignment of CNTs grown using MPECVD (Saifuddin et al. 2012).

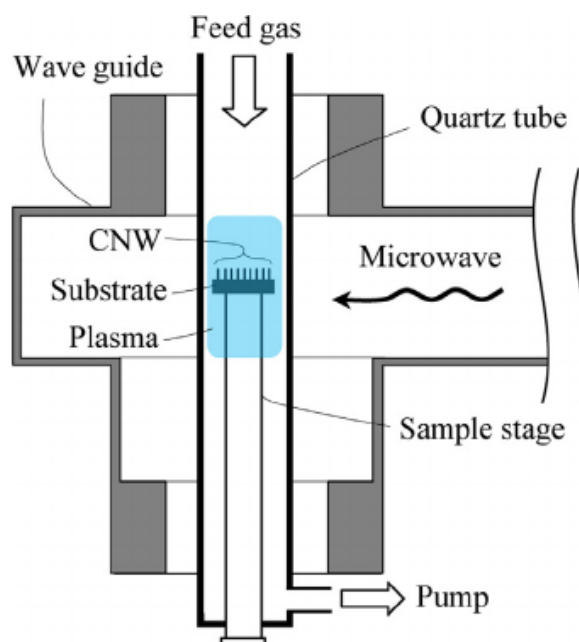


Figure 2-13: Microwave plasma enhanced chemical vapour deposition (Hassan et al. 2013)

2.4.4. Methane decomposition synthesis method

Research has shown that the most stable hydrocarbon at high temperatures to be natural gas containing up to 90% methane and therefore ideal for the purpose of self-decomposition in producing CNTs (Zeng et al. 2006). Hence, in order to synthesise CNTs, transition metal catalyst particles must be used to decompose methane. Therefore, the choice of hydrocarbon is a key element in the successful growth of good quality SWCNTs which contains no amorphous and soot contaminants (Yeoh et al. 2009). The process involves, methane reacting with transition metal nanoparticles which gives rise to CNTs as well as pure hydrogen (as a by-product).

A fixed bed reactor consisting of transition metal catalyst is used to decompose the methane at temperatures greater than 550°C (Yeoh et al. 2009). At the discharge stream, nearly pure hydrogen gas is produced as a by-product, whereas CNTs are left on the metallic catalyst. An inert gas is fed into the reactor for safety reasons.

Figure 2-14 shows the technique described above. Takenaka et al. (2003) found that methane decomposition synthesis method proves to be promising for increasing the production rate of defect free CNT based materials at a kilogram level. With catalysts of Nickel nanoparticles, well graphitised CNTs are synthesised without soot and amorphous impurities. The catalyst design is used as the controlling factor of the CNT diameters. Whereas, the yield of CNTs is determined by both the supportive material and type of transition metal used (Ermakova et al. 2001).

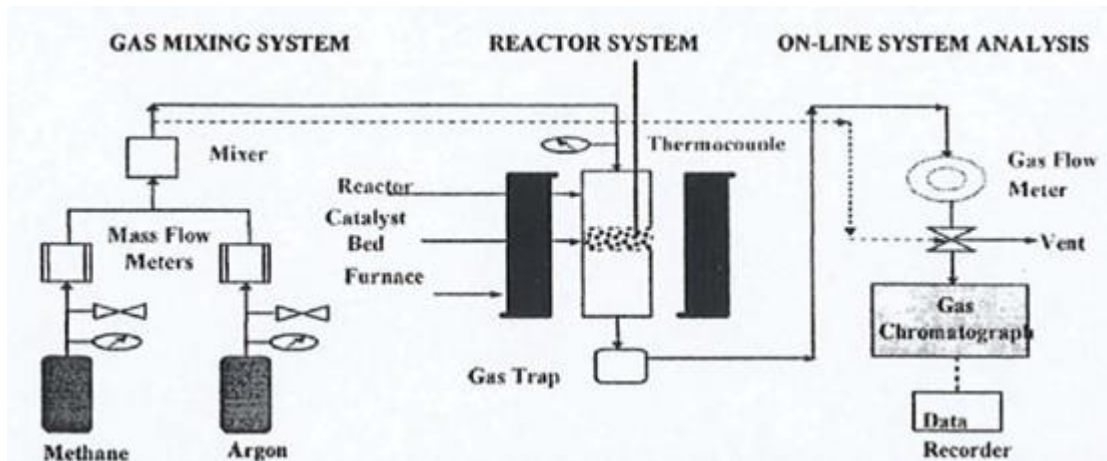


Figure 2-14: Methane decomposition fixed bed reactor system (Prasek et al. 2011)

2.4.5. Self-assembly of single crystals of SWCNTs

This approach was investigated by Schlittler et al. (2001) where the process enables the production of CNTs with control over the CNT diameter, straightness and chirality. The CNTs produced using this are very pure. A mixture of Ni and C is dissolved through a stencil of nanoscale proportions with holes having a diameter of 300nm, which is placed a few microns above a surface. Sub-nanometre precision can be achieved during the process.

The choice of substrate plays a vital role as the substrate material is responsible for constraining the Ni and C to the original 300nm diameter during the diffusion process at high temperatures. Schlittler et al. (2001) also found that using molybdenum as a substrate provides an exceptional result either in the form of a grid for TEM analyses or as a solid film 'splattered' onto a silicon wafer. Additionally, the CNT direction of growth is manipulated through the use of the magnetic field. Research involving self-assembly of single crystals of SWCNTs is currently under further investigation by researchers in the field.

2.4.6. Carbon nanotube purification

During the synthesis of CNTs, a great deal of imperfections such as metal particles, amorphous carbon and multi-shells are found present within the nanotubes. Purification of CNTs will result in improved material properties. The purification steps include;

1. Air oxidation: CNTs have a decreased purity of about 5 to 10%. Purification is therefore required before they can be used for applications such as drug delivery. Air oxidation is especially valuable in managing the volume of metal catalyst particles and carbon present, such as Y and Ni (Mehta 2014).

2. Acid refluxing: The volume of metal particles and amorphous carbon is controlled through the use of a strong acid. Commonly used acids are nitric acid (HNO₃) and sulphuric acid (H₂SO₄) but where the preferred refluxing acid was identified as hydrochloric acid (Ermakova et al. 2001).
3. Surfactant aided sonication, filtration and annealing: Although the above process resulted in purer CNTs, the nanotubes were usually still entangled which trapped majority of the impurities. Surfactant-aided sonication is performed using sulphonate (SDBS) aided sonication with either methanol or ethanol as a solvent. The solution is then filtered and annealed at 1273K in nitrogen for four hours. Annealing is then used to optimise nanotube structures. It is therefore demonstrated that the surfactant-aided sonication could effectively be used to untangle CNTs, and as a result reducing the particulate impurities trapped within the entanglements (Ermakova et al. 2001).

2.5. Carbon nanotubes mechanical properties

There are large volumes of literature populated with various theoretical and practical procedures used to control the mechanical properties of CNTs. Their light weight, surface area, ordered structure, high mechanical strength, increased aspect ratio, improved electrical conductivity and their metallic or semi-metallic behaviour make them the ideal candidate for a great deal of applications.

Typically, the mechanical properties of structural materials are heavily reliant on the elastic modulus. This is simply the relationship between the strain and stress subject to predetermined loading conditions. Composite materials possess a very discrete nature and their properties are therefore heavily dependent on the constituent's material properties. The effective moduli are then taken as an average, based on the fraction of each constituent material (Belytschko et al. 2002).

It is understood that the interface between the nanotubes and the matrix of two-phase atomic bond structures are irregular and interrupted, due to the distribution of electrons at the surface which then impacts interface bonding. This also disrupts the energy distribution within each phase thus, creating differences between the energy related to the surface atoms and that of the bulk of the material. Therefore, the elastic modulus of the bulk and surface region differ. The surface stress is responsible for elongating the substrate and therefore affecting the thus density of surface atoms while maintaining the same number of surface atoms (Hu et al. 2008).

Since motion of dislocations are thermally activated, it was discovered that temperature plays a key role in the strength of the CNTs. CNTs are brittle at low temperatures, irrespective of their helicity and diameter. At room temperature flexible CNTs are observed as a result of their high strength and distortion capability. At high temperatures, the CNTs displayed spontaneous formations of double pentagon-heptagon pairs (Hu et al. 2008). Defects in CNTs were also found to depend heavily on the chirality of the nanotubes. These defects are responsible for the possibility of plastic deformation to occur (Hu et al. 2008).

The electronic and electrical properties of CNTs are affected by distortions such as twisting and bending of the CNTs. The formation of pentagon-heptagon pairs can also be introduced in CNTs through bending. The result of these formations are semiconductor-metal and metal-metal nanoscale connections which can be altered for use as nano-switches (Hu et al. 2008). Bending angles greater than 45° results in kinks within the structure of the nanotubes, thus reducing the conductivity of CNTs. To account for the bending of nanotubes an increase in tube diameter can lead to a change in the bending resistivity (Belytschko et al. 2002). A model was created by Hu et al. (2008) to study the buckling characteristics of individual MWCNTs under radial pressure and it was found to be in good agreement with experimental results thus confirming the bending properties of nanotubes. Also, doping of nanotubes provides various opportunities for manipulating their physical properties which can be used in applications such as nano-electronics, chemical sensors, nonlinear optics and field emissions (Belytschko et al. 2002). The mechanical properties of nanocomposites will be investigated in depth in later chapters as this forms part of the dissertation.

2.5.1. Strength of carbon nanotubes

The strength of a material is associated with both the distribution and the number of defects present within a material. Therefore, it has been hypothesised that the strength of carbon nanotubes may be significantly higher when compared to competing materials due to their near-perfect microstructure. The strength of CNTs are thus heavily dependent on the synthesis method used as this determines the quality of the CNTs. Another factor that affects the strength of CNTs is its length as the longer a nanotube is, the more likely it is to have a concentration of defects somewhere along its span. Numerous theoretical simulations have been performed using molecular dynamics. These simulations emphasised the temperature, loading rate and defects present. Yakobson et al. (1996) performed such simulations under tensile loading and reported fracture strains of 30% and strengths of up to 150GPa. Belytschko et al. (2002) investigated the fracture behaviour of nanotubes using molecular dynamics, it

was demonstrated that there is a correlation between fracture strength and CNTs chirality, furthermore they reported fracture strains between 15.8% and 18.7% as well as fracture strengths ranging between 93.5GPa and 112GPa.

The impact of strain rate and temperature have also been investigated on nanotubes however these simulations are limited by the small-time scale offered by molecular dynamics methods. These effects are not dealt with in detail in this dissertation as they are not of importance for our investigation.

The extremely small dimensions of CNTs have made it difficult to experimentally determine the mechanical properties of said nanotubes. General observations using TEM were first used to provide insights into the stiffness and strength of nanotubes. TEM has also been used in a quantitative capacity and recently, the ability to measure the response of individual nanotubes to forces placed on them has been realised through scanning probe microscopy. Yu et al. (2004) studied bent and buckled nanotubes using TEM images of CNTs and compared them to those produced by atomistic simulations. A close resemblance of nanotube buckling was found in the studies, indicating the accuracy of the simulations.

Treacy et al. (1996) analysed the mechanical properties of CNTs by measuring the mechanical resonance of nanotubes in TEM images. The Young's moduli measured ranged between 410GPa and 4150GPa, with an average of 1800GPa. Krishnan et al. (1998) investigated the Young's moduli of SWCNTs and obtained a Longitudinal Young's modulus of 1.25TPa. Furthermore, Poncharal et al. (1999) extended the research to MWCNTs and found similar results to that yielded above.

Wong et al. (1997) tracked the bending behaviour of MWCNTs through the use of an atomic force microscope (AFM). A Young's modulus of 1.28TPa was reported using a beam mechanics model. Techniques were developed by Salvétat et al. (1999) to determine the characteristics of both MWCNT and SWCNT ropes. Stress versus strain curves were obtained, indicating Young's moduli values ranging from 270GPa to 950GPa for MWCNTs and from 320GPa to 1470GPa (mean of 1002GPa) for SWCNT ropes. Yu et al. (2000) furthered their research by measuring the shear strength between shells of MWCNTs. Very low values of shear strength were measured, averaging around 0.08MPa.

2.5.2. Carbon nanotube elastic properties

Since CNTs are made of cylindrical graphene sheets, it would be anticipated that the strength, stiffness and modulus of CNTs should be similar to the in-plane values of graphite which are

well understood. However, the elastic properties of the CNTs are heavily affected by nanotube curvature. Nanotubes of smaller diameters are affected more than nanotubes of larger diameters. Thostenson et al. (2001) theoretically predict the Young's moduli of carbon nanotubes using a combination of first principles and a Keating Hamiltonian approach. Treacy et al. (1996) determined the Young's modulus to range between 1500 and 5000GPa. Fan (1999), using continuum elastic theory, performed an energetics analysis and found that the strain energy was determined to be inversely proportional to the square of the CNT radius. Karthikeyan et al. (2009) later verified these results using both Tersoff and Tersoff-Brenner potentials.

Yakobson et al. (1996) performed computational studies and used a Tersoff-Brenner potential in a molecular dynamics simulation and compared the results found to the continuum shell model. A Young's modulus of 5.5TPa was found which is very high due to a small shell thickness which was set to 0.066nm. Lu (1997) used an empirical model in molecular dynamics evaluations to determine the mechanical properties of both SWCNTs and MWCNTs in a simulated tensile test. Young's moduli of roughly 1 TPa and shear moduli of 0.5 TPa were determined. The results found that aspects such as nanotube radius, chirality and number of walls had a slight impact on these values. Hernández et al. (1998) used an energy-per-surface rather than per-volume approach. The Young's modulus was determined to be 1.2TPa (slightly higher than graphite) when a thickness of 0.34nm is assumed. This value was found to be dependent on nanotube diameter. Sánchez-Portal et al. (1999) investigated the effects of SWCNTs and MWCNTs stiffness on the elastic properties. The stiffness of SWCNTs was found to be close to that of the in-plane stiffness of graphite. It was determined that curvature in thin SWCNTs played a minor role in the CNT Young's modulus.

Similar research was performed by Popov et al. (2000) who determined multiple elastic constants, showing that the Poisson's ratio, elastic and bulk moduli have a dependence on nanotube radius.

2.6. Computer simulation modelling techniques

The advancement of technology and science has stretched into the field of nanotechnology therefore the development of nanotube-based structures require a good understanding of nanotube properties. An important first step in analysing the development of structural composites would be to perform an accurate assessment of the mechanical properties of individual nanotubes.

The particularly small size of nanotubes, has resulted in the practical assessment of their elastic properties such as buckling resistance, tensile strength and elastic modulus to presents difficulties to researchers in the field. Problems associated with the experimental analysis include high costs, the size of the analysis and technological difficulties such as manipulating nanometre-sized objects. Researchers have since looked at employing computational methods for modelling the behaviour of nanostructures. It is however still a challenging process to develop efficient methods to analyse nanomaterials computationally. The three most successful methods used to analyse CNT computationally include atomistic modelling, continuum modelling and nano-scale continuum modelling.

Some examples of atomistic approaches include classical molecular dynamics (MD) (Lijima et al. 1993; Yakobson et al. 1996), density functional theory (DFT) (Sánchez-Portal et al. 1999) and tight binding molecular dynamics (TBMD) (Hernández et al. 1998). Although most molecular and atomic systems can be simulated by using these modelling techniques, atomistic modelling is limited due to the computational complexity due to the number of atoms involved in the analysis. Therefore, this only allows for studies to be analysed which last no longer than picoseconds or nanoseconds due to the computational cost of the analysis.

The second approach is the continuum mechanics modelling technique. Majority of computational assessments have resorted to classical continuum models for analysing CNTs. Researchers such as Tersoff (1992) and Yakobson et al. (1996), based on the bending and twisting of a graphite sheet, have performed simple analyses of the energies of fullerenes. It was found that the mechanical properties of the graphite sheet can be utilised in predicting the nanotube's elastic strain energies of fullerenes. Based on this, Yakobson et al. (1996) developed a continuum shell model which was then furthered by Ru (2000), placing focus on the buckling characteristics of CNTs when under axial compression. This continuum shell model can be utilised in analysing both the static and/ or dynamic elastic behaviour of CNTs. Though, these models do not take into account the forces imposed on the individual atoms as well as the detailed effects of nanotube chirality.

Therefore, there is a requirement for developing a modelling approach that analyses the elastic behaviour of CNTs at an atomistic level, but which is not restricted by time scales. Such a modelling technique would assistance research in designing nano-devices as well as performing multi-scale simulations of nano-systems. As a result, nano-scale continuum modelling was developed (Li et al. 2003).

2.6.1. Atomistic modelling

Atomistic modelling, based on the imposed boundary conditions and interactive forces, determines the locations of atoms (Shokrieh et al. 2010). In order to determine the material properties, this data is needed to solve Schrödinger wave. Atomistic modelling techniques consists of three main approaches, namely:

- Monte Carlo (MC),
- molecular dynamics (MD) and,
- *ab initio* approaches.

Additional atomistic modelling approaches such as TBMD, DFT, local density (LD), Morse potential function (MPF) approach and modified MPF techniques were also taken into consideration. Shokrieh et al. (2010) extensively reviewed the atomistic modelling techniques for determining the Young's moduli of CNTs. The primary approach used for simulating the behaviours of nanotubes was MD methods.

Once the force fields and total potential energy of a system was determined, then the mechanical properties of a system of molecules and atoms can be obtained. While both MC and MD techniques are based off of Newton's second law, MC approaches are stochastic based while MD approaches are deterministic approaches. Where, Schrödinger equation is the underlying principle of the *ab initio* techniques. Additionally, the *ab initio* methods are potential-free approaches where the electronic structure is used to determine the atomic forces. Furthermore, the MC and MD approaches attain the forces acting on atoms through differentiating interatomic potential functions (Shokrieh et al. 2010).

Zhang et al. (2008) investigated the dispersion characteristics of polymer based SWCNTs on their load transferring abilities, using MD techniques. Ganji et al. (2010) exploited the tight binding to investigate the impact of curvature on SWCNTs Young's modulus and atom's energy. Based on these results it was concluded that MD simulations result in accurate estimates of the CNT's elastic properties exposed to external forces. Although, MD methods takes long to compute, and computational costs are much higher especially when dealing with MWCNTs composed of many atoms.

2.6.2. Continuum modelling

Continuum models (CM) are generally utilised to investigate the elastic properties of nanotubes. The underlying assumption of continuum modelling is that CNTs can be modelled as a continuum structure with a constant distribution of stiffness and mass. Therefore, the

lattice structures of CNTs are simply ignored in continuum modelling and instead substituted with a continuum medium. This modelling approach can be either accomplished analytically or numerically via Finite Element Methods (FEM).

Hu et al. (2008) presented similar characteristics between MD simulation of nanotubes and that of macroscopic-shell modelling techniques. Yakobson's (1996) research also showed that the elastic properties of CNTs were strongly reliant on their atomic structure, chirality, curvature and helicity. However, these mechanical properties can't be obtained using the isotropic-shell model because of the disregarding of the CNT geometry. Chang (2010) studied the mechanical properties of SWCNTs through the use of an anisotropic shell model, unlike common shell models which are constructed using an isotropic continuum shell with constant elastic properties. This modelling technique enables the determination of the chirality induced effects on the elastic properties of nanotubes through combining continuum modelling and molecular approaches. Silvestre et al. (2011) investigated both the limitations and applicability of shell models and showed that Donnell theory (shallow shell theories) is not able to analyse CNTs accurately due to the CNT's non-shallow structure. However, it was found that Sanders theory (complex shell theories) can correctly match the results obtained from MD simulations. Values for CNT diameter and thickness aren't well defined in continuum models. As an example, while inter-planar spacing values of 0.34 nm between graphene sheets are commonly used for tube thickness, Wang et al. (2014) found that by comparing the continuum shell model results with those obtained from MD simulations that the effective CNT thickness was 0.066nm. Furthermore, Odegard et al. (2005) used a truss-based model and found the actual tube thickness to be 0.65nm. However, Vodenitcharova and Zhang (2006) calculated the actual wall thickness to be 0.0617nm based on a measure of CNT deformation. Wang and Zhang (2008) studied the effective wall thickness and mechanical properties of SWCNTs as well as their deformation relationships. Some fields such as the effective elastic modulus and effective bending stiffness were later introduced.

Continuum structures are also used to define the CNT material properties obtained from experimental results. Batra and Sears (2007) analysed nanotube defects of both SWCNTs and MWCNTs and suggested an equivalent continuum model for MWCNTs whose response to deformations was calculated using MD simulations as well as engineering theories. Zhao et al. (2013) conducted a theoretical analysis to determine the cohesive energy between CNTs and graphene through continuum modelling taking into consideration van der Waals forces. Batra and Sears (2007) utilised molecular simulations to acquire wall thickness, shear modulus and

Young's modulus of an equivalent continuum linear-elastic isotropic tube. The results obtained were then compared to those of continuum tube modelling for bending and buckling analyses. Based off these comparisons, it can be seen that the Euler-Bernoulli beam equations used to determine the bending deformation strain energy is in a good agreement with MD techniques.

2.6.3. Nano-scale continuum modelling

Nano-scale continuum modelling (NCM) of nanotubes provides an replaces the carbon-carbon bond with a continuum component as opposed to continuum modelling where the entire nanostructure is substituted for a continuum medium. In summary, NCM uses structural elements to replace the molecular connections amongst the carbon-carbon bonds. This allows for the mechanical properties to be obtained through atomistic modelling.

The equivalent-continuum as well as the quasi-continuum techniques are popular approaches that have been used in nanoscale modelling. Tadmor et al. (1996) introduced the quasi-continuum approach by incorporating classical Cauchy–Born theory which allowed for a link to be made between the crystal lattice and deformations of a continuum. Odegard et al. (2005) introduced the equivalent-continuum approach through combining continuum structural mechanics with computational chemistry, equating total molecular potential energies of a nanostructure with the strain energies of its equivalent continuum elements. The two models were further investigated by Zhao et al. (2013) by obtaining the elastic properties of graphene nanostructures and a significant difference in the elastic properties was observed. Additionally, Li et al. (2003) studied beam elements and developed a structural mechanics method by connecting the strain energy to the interatomic potential energy, thus creating a representation of each carbon-carbon bond. The relationship amongst structural and molecular spaces are described for each carbon-carbon bond through a factor which encompasses the entire nanostructure as investigated by Odegard et al. (2005).

Zhang et al. (2008) incorporated interatomic potentials to investigate the mechanical properties of SWCNTs through the use of nano-scale continuum theory. This theory was later furthered by Wu et al. (2008) where the bending and curvature effects were considered. Chang and Gao (2003) found that regardless of the load applied, the C-C link would always remain straight and therefore the spring components are ideal for modelling the C-C bonds.

Arroyo and Belytschko (2004), based on the exponential Cauchy–Born law, developed calculations to determine the properties of SWCNTs using finite deformation continuum theory. Furthermore, Liu and Chen (2003) further investigated the properties of CNTs through

the use of an atomic-scale FEA. Furthermore, Cheng et al. (2009) researched a new method entailing atomistic-continuum modelling techniques which incorporates equivalent-continuum and MD modelling methods.

An algorithm was then later advanced by Contreras et al. (2012) with the ability to model the CNT defects. The elastic behaviour of MWCNTs was analysed by Li et al. (2003) where MD is used and whereby every CNT wall is treated as a space frame. Here, nonlinear truss-rod elements are employed by incorporating Lennard-Jones potential to model the inter layer connections amongst tubes. Brcic et al. (2013) performed a similar analysis however the van der Waals interactions were not considered; a good agreement was observed between the two models. Wernik and Meguid (2010), using modified Morse Potential, found that under tensile and torsional loading the bending component has a noteworthy impact on the CNT structural stability. Additionally, the effects of torsional buckling and fracture progression have been investigated by Meo and Rossi (2006) who researched the CNT failures when subjected to uniaxial loading. The results demonstrate that nanotube chirality significantly affects the impact that defects have on the tensile characteristics of nanotubes. A remarkable reduction was observed in later studies.

3. Two-phase micromechanical analysis

Over the years several micromechanical techniques have been investigated and tested for a variety of composite materials. Information obtained from these analyses, such as those performed by Ghasemi et al. (2015), who used the results obtained to determine the thermo-mechanical characteristics of nanocomposites based on the constituent's properties, and later verified using practical testing.

To analyse the mechanical properties of nanocomposites effectively, micromechanical modelling techniques need to be employed. Apart from micromechanical modelling, other modelling methods such as molecular dynamics and Monte Carlo simulations can also be used for modelling multiscale composites to determine their properties. However, these methods require extensive computational resources and lengthy computer runs, making them impractical for multiscale composites. Analysing the composite material at a macroscopic level will also allow for a more thorough and accurate analysis while maintaining acceptable computational costs.

In this chapter micromechanical modelling techniques are used to analyse the flexural behaviour of two-phase nanocomposites which will lay the foundation for analysing three-phase nanocomposites in the next chapter. In the case of two-phase composites, constituents involve a matrix material (e.g. epoxy) and a nano-sized reinforcement (e.g. CNTs, nanoparticles, graphene platelets) will be analysed. To effectively analyse three-phase nanocomposites later-on, which in this case can be described as a fibre reinforced composite which has been modified with nano-sized materials, various modelling scenarios are firstly taken into consideration. These scenarios include aligned CNTs, randomly orientated CNTs and the impact of agglomerated nanotubes on the elastic properties of two-phase nanocomposites. A systematic modelling approach, as seen in Figure 3-1, is employed in order to use the results obtained in this section in the next, as performing a two-phase analysis is the first step in performing a multi-stage three-phase micromechanical analysis.

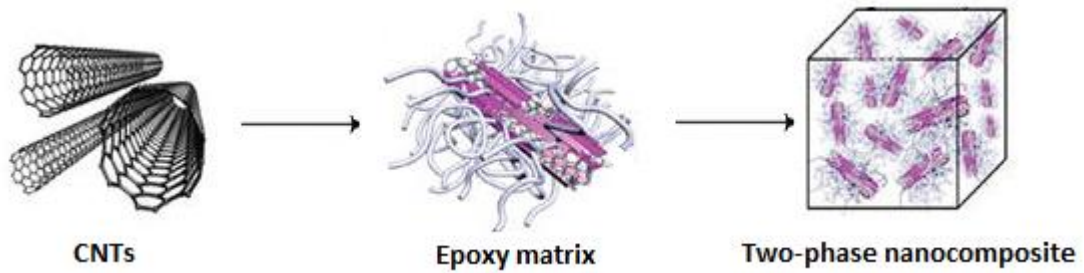


Figure 3-1: Two-phase micromechanical modelling approach

As seen in Figure 3-1 above, the nanocomposite comprises of an epoxy matrix with CNT reinforcement. The composite’s mechanical properties are analysed for increasing CNT volume fraction. The results obtained can then be used to determine the effectiveness of nanotube reinforcement, act as a foundation on which the three-phase analyses will be based and can also be used to benchmark against both two-phase and three-phase nanocomposites.

It should be noted here that data obtained on the mechanical characteristics of multiscale composites has proven to be useful in several fields including civil, automotive, aerospace, structural and mechanical engineering. Micromechanical approaches used to determine the properties of complex composites are opted for because of their ease of use, low cost and high accuracy.

3.1. Material properties and considerations

Phase one of the iterative processes involves analysing the two-phase nanocomposite as an epoxy-CNT composite after which the three-phase analysis will incorporate carbon and glass fibre reinforcement respectively. The composite constituents properties can be seen in Table 3-1 (Miyagawa et al. (2005), Shokrieh et al. (2010) and Arash et al. (2014)).

Table 3-1: Mechanical properties of composite constituents (Smith et al. 1974)

Material parameter	Carbon fibre	Glass fibre	Epoxy resin
Young’s modulus (GPa)	230	73.5	3.5
Transverse modulus (GPa)	8	72	N/A
Poisson’s ratio	0.3	0.22	0.4
Density (kg/m ³)	1680	2570	1200
Shear modulus (GPa)	27.3	33	1.25
Bulk modulus (GPa)	N/A	45	4.95

The CNT mechanical properties are depicted below in Table 3-2 (Popov et al. 2000).

Table 3-2: Mechanical properties of carbon nanotubes (Al-Saleh et al. 2011)

Young's modulus (GPa)	Poisson's ratio	Shear modulus (GPa)	Density (kg/m ³)	Length (μm)	Outer diameter (nm)	Thickness (nm)
1000	0.3	480	1680	8.5	8	0.8

In performing micromechanical analyses, numerous considerations that potentially influence the mechanical properties of nanocomposites have been identified, which impact parameters such as the strength and stiffness of the material. Some of these factors include (Fisher et al. 2003):

- Nanotube orientation
- Nanotube waviness
- Nanotube distribution
- Nanotube-matrix interface de-bonding

In this chapter we take into consideration some of these factors and their effect the flexural behaviour of two-phase nanocomposites, along with popular modelling techniques to establish the most suitable one for the application. Mori & Tanaka (1973) developed a micromechanical model capable of predicting the elastic moduli of straight, aligned CNTs. It was found that by controlling the nanotube direction, desired properties can be obtained. Furthermore, the Mori-Tanaka model implemented a parameter to account for the effect of nanotube-matrix de-bonding. Halpin et al. (1973) developed a similar model where nanotube orientation was taken into consideration and it was found to be accurate for composites with straight, randomly orientated CNTs. The nanotube distribution within the matrix is analysed using the inclusion model studied by Eshelby (Roatta et al. 1997).

Lastly, the effect of nanotube agglomeration is commonly evaluated using the Mori-Tanaka approach (Mori & Tanaka 1973). The results of this study may also be useful for analysing the flexural response of CNT based epoxy composites. This will in turn allow for tailored materials to be created for problem specific applications.

Nanotube waviness is not taken into consideration in this chapter as it makes for a very computationally expensive analysis. The focus of the dissertation is also more geared towards nanotube orientation and the effects of CNT agglomeration.

It should however be noted for future research that research performed by Sheng et al. (2004), Odegard et al. (2005) and Anumandla et al. (2006) investigated the impact of nanotube undulation on both the Young's moduli and Poisson's ratio of nanocomposites. Sheng et al. (2004) hypothesised that with increasing weight fraction so does the effect of curvature. However, Shi et al. (2004), Odegard et al. (2005) and Anumandla et al. (2006) agreed that nanotube waviness has little impact on the lateral modulus. Seidel et al. (2006) and Yu (2011) both studied the development of a micromechanical FEA for the approximation of the effective Young's moduli of nanocomposites. As a result of their findings, it was determined that as the amount of randomness increases, a decrease in the Young's modulus can be seen. Other studies performed by Fisher et al. (2002), Shao (2009) and Kundalwal et al. (2013) used a modified micromechanical approach to analyse the effects of nanotube waviness and orientation. They found the waviness of the nanotubes with both aligned and randomly oriented nanotubes to reduce the elastic modulus in the CNT direction as compared to straight CNTs.

3.2. Carbon nanotube critical length and aspect ratio

The critical length as well as the aspect ratio of the CNT reinforcement fibres have a significant impact when determining the strength and bending characteristics of the composite. For the nanotubes to have any effect on the elastic properties, the fibre length needs to exceed the critical length. The critical length of carbon nanotubes can be represented by:

$$l_c = \frac{\sigma_{CNT}d}{2\tau_{CNT}} \quad (3.1)$$

where, l_c depicts the CNT critical length, σ_{CNT} represents the CNT ultimate strength, d represents the CNT diameter (outer) and τ_{CNT} depicts the interfacial shear strength between the matrix and CNTs. Eq. (3.1) depicts the carbon nanotubes as being solid, however in reality they are hollow, therefore the Kelly-Tyson approximation is proposed where (Hassan et al. 2011):

$$l_c = \frac{\sigma_{CNT}d}{2\tau_{CNT}} \left(1 - \frac{d_i^2}{d^2}\right) \quad (3.2)$$

and d_i represents the internal diameter of the hollow carbon nanotubes. Figure 3-2 below compares Eq. (3.1) to Eq. (3.2) in order to determine the effectiveness of using the Kelly-Tyson approximation.

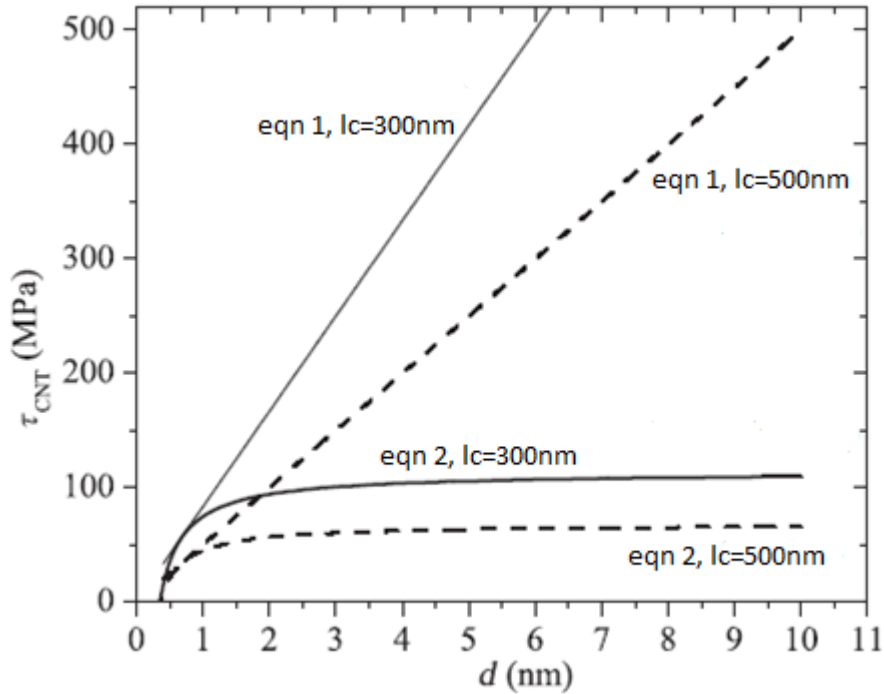


Figure 3-2: Graph of interfacial shear strength vs nanotube diameter (Hassan et al. 2011)

It can clearly be seen that the linearity of Eq. (3.1) will result in severe overestimation of the nanotube interfacial shear strength therefore, modelling based on the Kelly-Tyson approximation is opted for to obtain more accurate results. From Eq. (3.2) we can see that the CNTs will achieve their ultimate strength, under tension, when the aspect ratio equates to:

$$\alpha_c = \frac{l_c}{d} \quad (3.3)$$

where α_c represents the CNT critical aspect ratio. Shokrieh et al. (2017) showed that when l_c typically ranges between 50 and 500nm, the corresponding ultimate strength ranges between 20 and 150GPa. Assuming an ultimate strength of 50 GPa, the relation between the outer and inner diameter can be depicted by:

$$d = d_i + 0.68nm \quad (3.4)$$

This allows for the critical length and aspect ratio of the nanotubes to be further analysed. Using a critical length of 100nm and an ultimate strength of 150GPa, we can therefore determine the interfacial shear strength to be 980 MPa as per the above equations, which is

higher than the carbon fibre's interfacial shear strength. Based on the above equations as well as experimental data, a critical aspect ratio of 1/6 is opted for when modelling carbon nanotubes Shokrieh et al. (2017).

3.3. Reinforcement using straight, aligned carbon nanotubes

A Mori-Tanaka approach is used to analyse nanocomposites reinforced with straight, aligned carbon nanotubes. The Mori-Tanaka approach was chosen because of its simple yet accurate way of analysing nanocomposites using micromechanical modelling techniques.

The Mori-Tanka method assumes that each fibre is embedded within a perfect matrix and that no de-bonding occurs between the fibre-matrix interfaces. It is also assumed that the nanotubes are of infinite length. To further reduce the possible effects of the weak fibre-matrix interfaces, epoxy was selected to be used as a matrix as the fibre-matrix interface between epoxy and carbon nanotubes is excellent, resulting in a more accurate analysis and allowing for more focus to be placed on the effects of nanotube orientation (Wuite 2005).

When selecting a RVE, V , of the nanocomposite, then the RVE boundary ∂V is exposed to either an even overall stress, σ^0 , or to an even overall strain ϵ^0 . The Mori-Tanaka approach assumes that the inclusions are embedded in a perfect matrix which is then exposed to an effective strain, ϵ_M , or to an effective stress, σ_M . Here, ϵ_M represents average strain and σ_M represents average stress of the matrix. Thus, the effective elastic moduli, \mathbf{C} , is given as:

$$\mathbf{C} = (\mathbf{C}_M \mathbf{C}_M + V_{CNT} \mathbf{C}_{CNT} : \mathbf{A}) : (V_M \mathbf{I} + V_{CNT} \mathbf{A})^{-1} \quad (3.5)$$

where, a bold face letter denotes a 2nd or 4th order tensor, and a colon represents contraction. \mathbf{I} represents the 4th order identity tensor, M represents the matrix and CNT the carbon nanotubes. V_M and V_{CNT} denote the matrix and carbon nanotube volume fractions respectively, \mathbf{C}_M and \mathbf{C}_{CNT} denote the corresponding elastic moduli tensors and \mathbf{A} the 4th order tensor links the average strains, ϵ_M and ϵ_{CNT} through:

$$\epsilon_{CNT} = \mathbf{A} : \epsilon_M \quad (3.6)$$

and, where \mathbf{A} can then be depicted as:

$$\mathbf{A} = (\mathbf{I} + \mathbf{S} : (\mathbf{C}_M))^{-1} : (\mathbf{C}_{CNT} - \mathbf{C}_M)^{-1} \quad (3.7)$$

where, \mathbf{S} is the Eshelby tensor (Mura 1987). Let us take into consideration an elastic and isotropic epoxy matrix reinforced with aligned, straight CNTs, with Poisson's ratio, ν_M , and Young's modulus, E_M . Each nanotube is modelled as being infinitely long and demonstrates

transversely isotropic material properties, hence making the nanocomposite transversely isotropic with the stress-strain relations being expressed as:

$$\boldsymbol{\sigma} = \mathbf{C} : \boldsymbol{\varepsilon} \quad (3.8)$$

which can further be expanded to:

$$\begin{Bmatrix} \sigma_{11} \\ \sigma_{22} \\ \sigma_{33} \\ \sigma_{23} \\ \sigma_{13} \\ \sigma_{12} \end{Bmatrix} = \begin{bmatrix} k+m & l & k-m & 0 & 0 & 0 \\ l & n & l & 0 & 0 & 0 \\ k-m & l & k+m & 0 & 0 & 0 \\ 0 & 0 & 0 & p & 0 & 0 \\ 0 & 0 & 0 & 0 & m & 0 \\ 0 & 0 & 0 & 0 & 0 & p \end{bmatrix} \begin{Bmatrix} \varepsilon_{11} \\ \varepsilon_{22} \\ \varepsilon_{33} \\ 2\varepsilon_{23} \\ 2\varepsilon_{13} \\ 2\varepsilon_{12} \end{Bmatrix} \quad (3.9)$$

where, l , n , k , m and p are the cross modulus, uniaxial tension modulus in the fibre direction, plane-strain bulk modulus normal to the fibre direction, in plane shear modulus normal to the fibre direction and the in-plane shear modulus parallel to the fibre direction respectively (Hill 1965). As per Mura (1987) the components of the Eshelby tensor, \mathbf{S} , for a long, straight fibre in the nanotube direction can be determined. By substituting into Eq. (3.7) the components of \mathbf{A} can be obtained. Substituting the new-found results of \mathbf{A} , into Eq. (3.5) yields the effective elastic moduli tensor of the nanocomposite material with straight, aligned carbon nanotube reinforcement (Mura 1987). Therefore, the Hill's elastic modulus can be expressed as (Hill 1965):

$$k = \frac{E_M \{E_M V_M + 2k_r(1 + \nu_M)[1 + V_{CNT}(1 - 2\nu_M)]\}}{2(1 + \nu_M)[E_M(1 + V_{CNT} - 2\nu_M) + 2V_M k_r(1 - \nu_M - 2\nu_M^2)]} \quad (3.10)$$

$$l = \frac{E_M \{V_M \nu_M [E_M + 2k_r(1 + \nu_M)] + 2V_{CNT} l_r(1 - \nu_M^2)\}}{(1 + \nu_M)[2V_M k_r(1 - \nu_M - 2\nu_M^2) + E_M(1 + V_{CNT} - 2\nu_M)]} \quad (3.11)$$

$$n = \frac{E_M^2 V_M (1 + V_{CNT} - V_M \nu_M) + 2V_M V_{CNT} (k_r n_r - l_r^2) (1 + \nu_M)^2 (1 - 2\nu_M)}{(1 + \nu_M) \{2V_M k_r (1 - \nu_M - 2\nu_M^2) + E_M (1 + V_{CNT} - 2\nu_M)\}} + \quad (3.12)$$

$$\frac{E_M [2V_M^2 k_r (1 - \nu_M) + V_{CNT} n_r (1 - 2\nu_M + V_{CNT}) - 4V_M l_r \nu_M]}{2V_M k_r (1 - \nu_M - 2\nu_M^2) + E_M (1 + V_{CNT} - 2\nu_M)}$$

$$p = \frac{E_M [E_M V_M + 2(1 + V_{CNT}) p_r (1 + \nu_M)]}{2(1 + \nu_M) [E_M (1 + V_{CNT}) + 2V_M p_r (1 + \nu_M)]} \quad (3.13)$$

$$m = \frac{E_M[E_M V_m + 2m_r(1 + \nu_M)(3 + V_{CNT} - 4\nu_M)]}{2(1 + \nu_M)\{E_M[V_M + 4V_{CNT}(1 - \nu_M)] + 2V_M m_r(3 - \nu_M - 4\nu_M^2)\}} \quad (3.14)$$

Using Eq. (3.11) to (3.14), the elastic moduli of epoxy-based nanocomposites, with straight, aligned carbon nanotube reinforcement can be plotted. Both the transverse elastic modulus, E_{22} , as well as the longitudinal elastic modulus, E_{11} , can be related to elastic modulus as follows:

$$E_{11} = n - \frac{l^2}{k} \quad (3.15)$$

and,

$$E_{22} = \frac{4m(kn - l^2)}{kn - l^2 + mn} \quad (3.16)$$

respectively. Using the above equations, a micromechanical model was developed using computational software MATLAB R2014b. The composite's constituent elastic properties can be seen in Table 3-1 whereas the Hill's elastic moduli for carbon nanotubes of approximate diameter 8nm are as follows: $l_r = 10$ GPa, $k_r = 30$ GPa, $n_r = 450$ GPa and $m_r = p_r = 1$ GPa (Popov et al. 2000). Additionally, the shear modulus and Poison's ratio can be calculated using:

$$G_{12} = 2p \quad (3.17)$$

and,

$$\nu_{12} = \frac{l}{2k} \quad (3.18)$$

A MATLAB R2014b script file was generated to analyse the engineering constants of straight, aligned carbon nanotubes, for increasing nanotube volume fraction (Appendix A.1.1.). Figure 3-3 shows the association between the transverse and longitudinal Young's moduli for an increasing CNT volume fraction. As shown, the longitudinal Young's modulus increases more rapidly in comparison to the transverse Young's modulus with increasing CNT volume fraction. This is due to the transversely isotropic nature of the nanotubes. Figure 3-3 also shows a large surge in the Young's modulus at low CNT volume fractions. It can be seen here that with no reinforcement ($V_{CNT}=0$), the longitudinal and transverse Young's moduli are 0.3 GPa and 1.3 GPa respectively. Compared to $V_{CNT}=0.2$, a significant increase in both E_{11} and E_{22} can be

seen, as $E_{11}=88.55$ GPa and $E_{22}=4.11$ GPa at $V_{CNT}=0.2$. Lastly, it should also be noted that for $V_{CNT}=0.007$, $E_{11}=E_{22}$.

Figure 3-4 depicts the Poisson's ratio plotted against increasing nanotube volume fraction. Here, it's seen that an inversely linear relationship is held between the nanotube volume fraction and the Poisson's ratio. Figure 3-5 depicts an increasing trend for the shear modulus plotted against nanotube volume fraction.

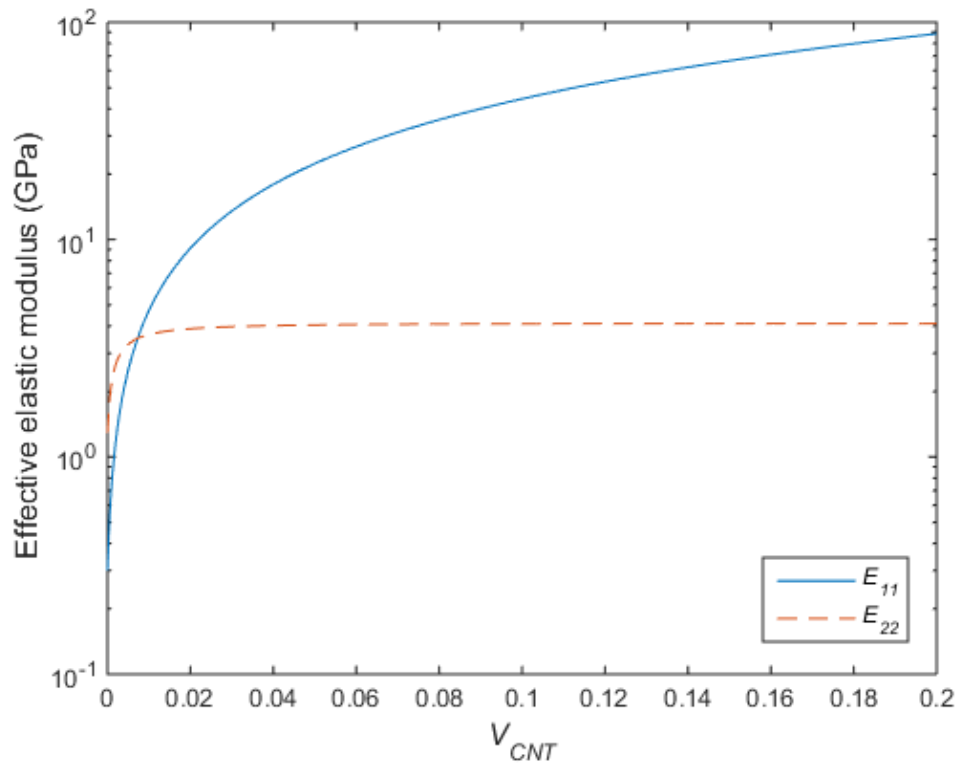


Figure 3-3: Effective elastic moduli for composite with straight, aligned nanotubes

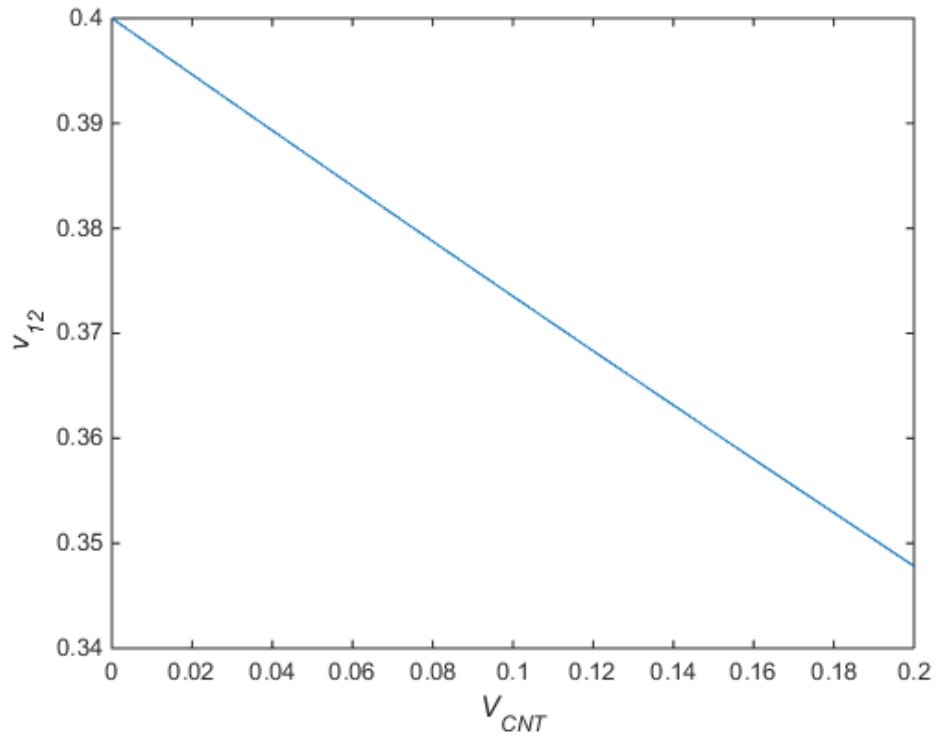


Figure 3-4: Effective Poisson's ratio for composite with straight, aligned nanotubes

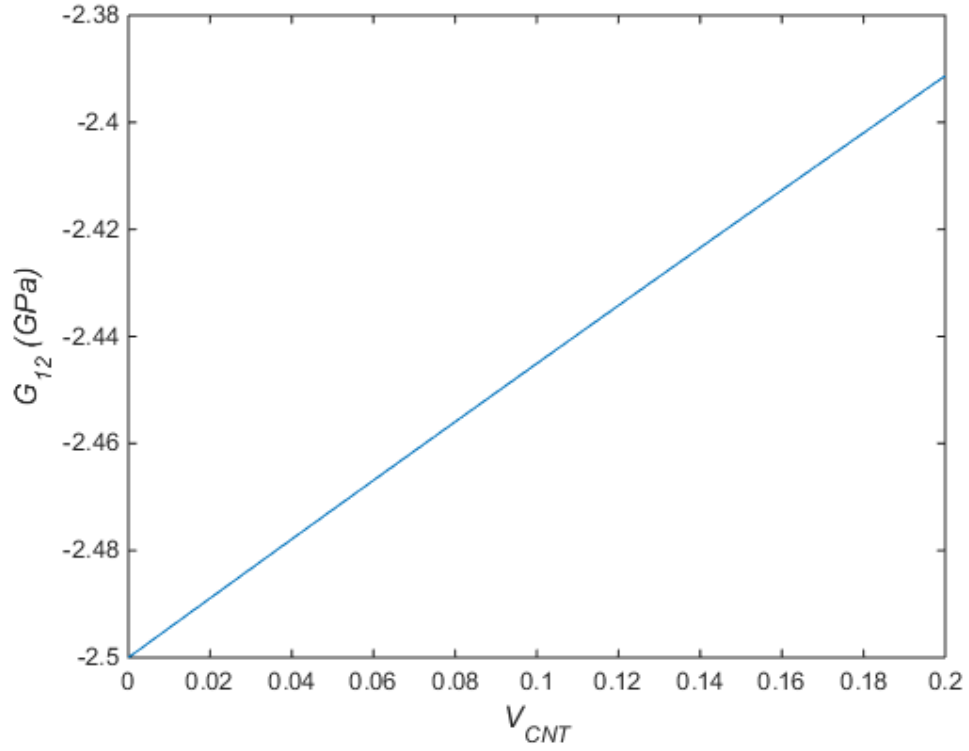


Figure 3-5: Effective shear modulus for composite with straight, aligned nanotubes

3.4. Reinforcement using straight, randomly orientated carbon nanotubes

In this analysis the effect of randomly orientated, straight carbon nanotubes on the mechanical properties of epoxy-based nanocomposites are analysed. The orientation of the straight carbon nanotubes can be determined using 2 Euler angles namely α and β as seen in Figure 3-6.

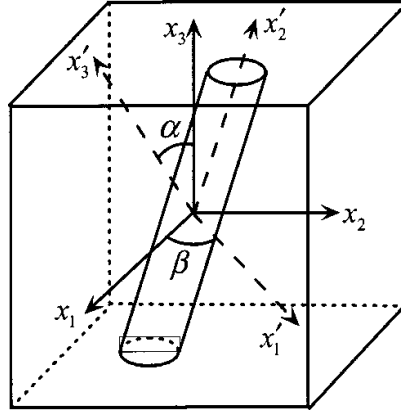


Figure 3-6: Euler angles of randomly orientated, straight carbon nanotubes (Foroughi 2013)

The base vectors, \mathbf{x}_1 and \mathbf{x}'_2 , of both the global and the local coordinate systems can be compared using matrix g (Shi et al. 2004), as depicted in Eq. (3.19) below:

$$g = \begin{bmatrix} \cos \beta & -\cos \alpha \sin \beta & \sin \alpha \sin \beta \\ \sin \beta & \cos \alpha \cos \beta & -\sin \alpha \cos \beta \\ 0 & \sin \alpha & \cos \alpha \end{bmatrix} \quad (3.19)$$

The distribution of the CNTs are determined by the probability density function $p(\alpha, \beta)$ which satisfies:

$$\int_0^{2\pi} \int_0^{2\pi} p(\alpha, \beta) \sin \alpha \, d\alpha d\beta = 1 \quad (3.20)$$

If the nanotubes are completely randomised, then the density function becomes:

$$p(\alpha, \beta) = \frac{1}{2} \pi \quad (3.21)$$

In this instance the Halpin-Tsai method is used to determine the elastic moduli. The Halpin-Tsai method assumes that the stress, $\sigma_{\text{CNT}}(\alpha, \beta)$ as well as the strain, $\epsilon_{\text{CNT}}(\alpha, \beta)$, of the CNTs can be associated to the stress of the matrix, σ_{M} .

Incorporating the strain concentration tensor, \mathbf{A} , as stated in Eq. (3.7), along with the theorems and relationships between stress and strain as stated by Eq. (3.8), the effective modulus of the composite can be determined. Note, completely randomised nanotube orientation within the matrix will result in an isotropic composite material, where the shear modulus, G , and the bulk modulus, K , is given by:

$$K = K_M + \frac{V_{CNT}(\delta_r - 3K_M\alpha_r)}{3(V_M + V_{CNT}\alpha_r)} \quad (3.22)$$

and,

$$G = G_M + \frac{V_{CNT}(\eta_r - 2G_M\beta_r)}{2(V_M + V_{CNT}\beta_r)} \quad (3.23)$$

where V_{CNT} , K_M , V_M and G_M and denote the nanotube volume fraction, matrix bulk modulus, matrix volume fraction and the matrix shear modulus respectively, whereas δ_r , α_r , η_r and β_r are described by Shi et al. (2004). The interface between the nanotubes and matrix for this model is considered to be perfect. The CNTs demonstrate transversely isotropic material properties. The model focuses predominantly on composites with aligned short nanotube fibres. The modulus of elasticity, as stated by Halpin et al. (1976) can be described by:

$$E_{11} = E_M \left(\frac{1 + c\eta V_{CNT}}{1 - \eta V_{CNT}} \right) \quad (3.24)$$

where,

$$\eta = \frac{E_{CNT}/E_M - 1}{E_{CNT}/E_M + \zeta} \quad (3.25)$$

and ζ represents a parameter that relies on the geometry of the matrix. To calculate the longitudinal modulus (E_{11}), ζ is set to equal $2l/d$ and in order to determine the transversal modulus (E_{22}), ζ is set to equal 2. To effectively analyse composites containing reinforcement with straight, randomly orientated CNTs of any length within an epoxy matrix, the Halpin-Tsai equations have been modified (Halpin et al. 1976). The modulus of elasticity for composites of this nature can be analysed using the following set of equations:

$$E_1 = \frac{1 + c\eta V_{CNT}}{1 - \eta V_{CNT}} E_M \quad (3.26)$$

where,

$$\eta = \frac{\alpha(E_{CNT}/E_M) - 1}{\alpha(E_{CNT}/E_M) + c} \quad (3.27)$$

In this set of equations α , the orientation factor, was introduced to account for the randomness of the distributed reinforcement (Gao 2005). Gao (2005) determined that if the reinforcement length is much less than the thickness, and if the carbon nanotubes are considered randomly orientated in three dimensions then an orientation factor of $\alpha = 1/6$ can be used.

Montazeri et al. (2011) further determined that for a decreased weight percentage of CNTs, not more than 2%, the above-mentioned set of equations approximates the Poisson's ratio and Young's moduli of the nanotube reinforced epoxy matrix with high accuracy. The transverse modulus can further be calculated as:

$$E_2 = \frac{1 + 2\eta V_{CNT}}{1 - \eta V_{CNT}} E_M \quad (3.28)$$

Furthermore, the volume fraction of nanotubes in the matrix is a function of the weight fraction of the CNTs and the densities of the matrix and CNTs as stated in Eq. (29):

$$V_{CNT} = \frac{W_{CNT}}{W_{CNT} + \rho_{CNT}/\rho_M - (\rho_{CNT}/\rho_M)W_{CNT}} \quad (3.29)$$

where W_{CNT} represents the weight fraction of the carbon nanotubes, ρ_m and ρ_{CNT} represents the density of the matrix and nanotubes respectively (Al-Saleh et al. 2011). A MATLAB script file was compiled calculating the effective Young's moduli, shear modulus and effective Poisson's ratio of randomly orientated, straight carbon nanotube reinforced epoxy-based composites. Figure 3-7 shows the effective longitudinal and transverse moduli for increasing nanotube volume fraction of straight, randomly oriented CNTs. A substantial increase in the longitudinal Young's modulus E_{11} , roughly 10 times more than pure epoxy, can be seen with the addition of nanotubes, however an insignificant increase in the transverse modulus, E_{22} , is also observed. Figure 3-8 depicts the Poisson's ratio for increasing nanotube volume fraction of straight, randomly oriented nanotubes in an epoxy matrix. The Poisson's ratio decreases with increasing nanotube volume fraction. The shear modulus versus carbon nanotube volume fraction can be analysed in Figure 3-9. Both the Poisson's ratio and shear moduli are observed to increase linearly.

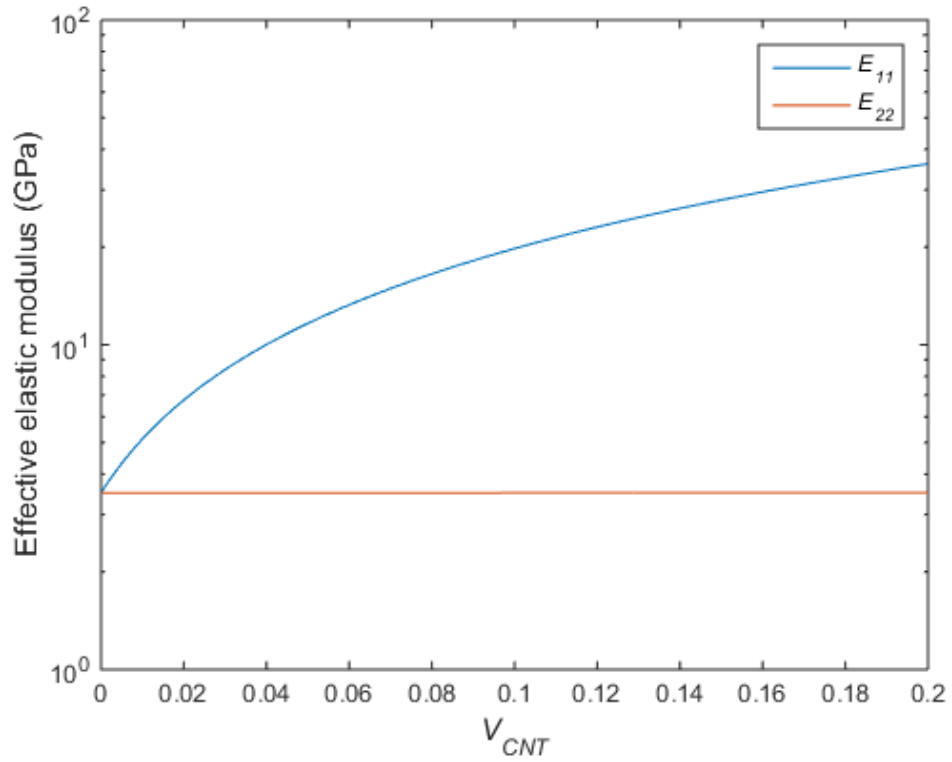


Figure 3-7: Randomly orientated carbon nanotube effective elastic moduli

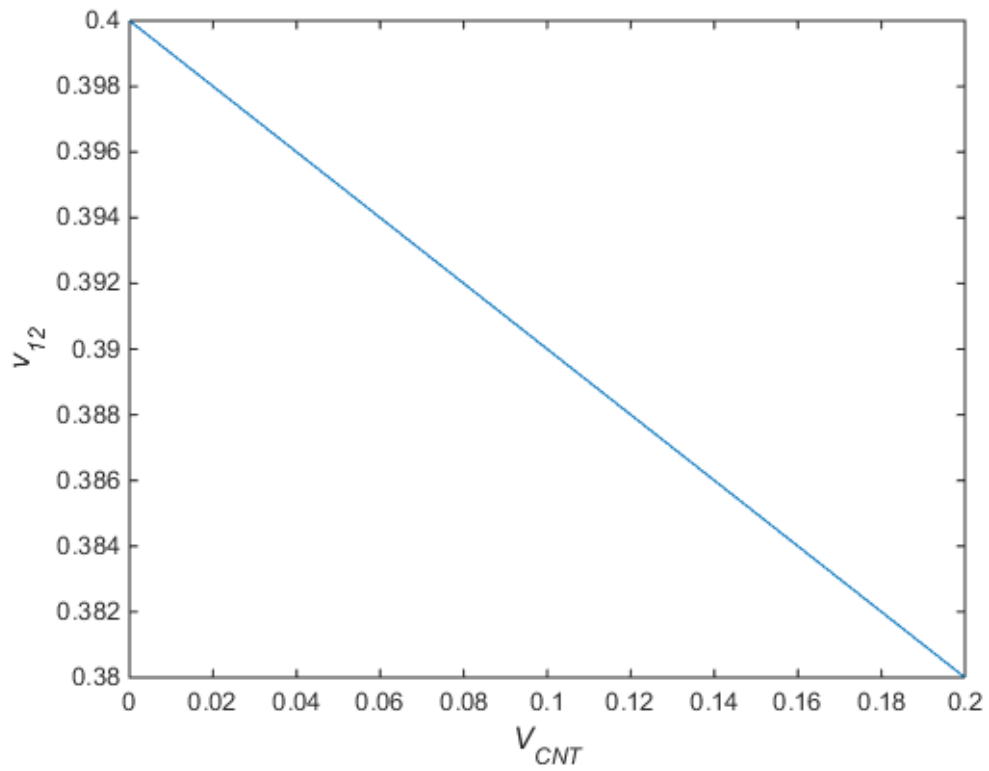


Figure 3-8: Randomly orientated carbon nanotube effective Poisson's ratio

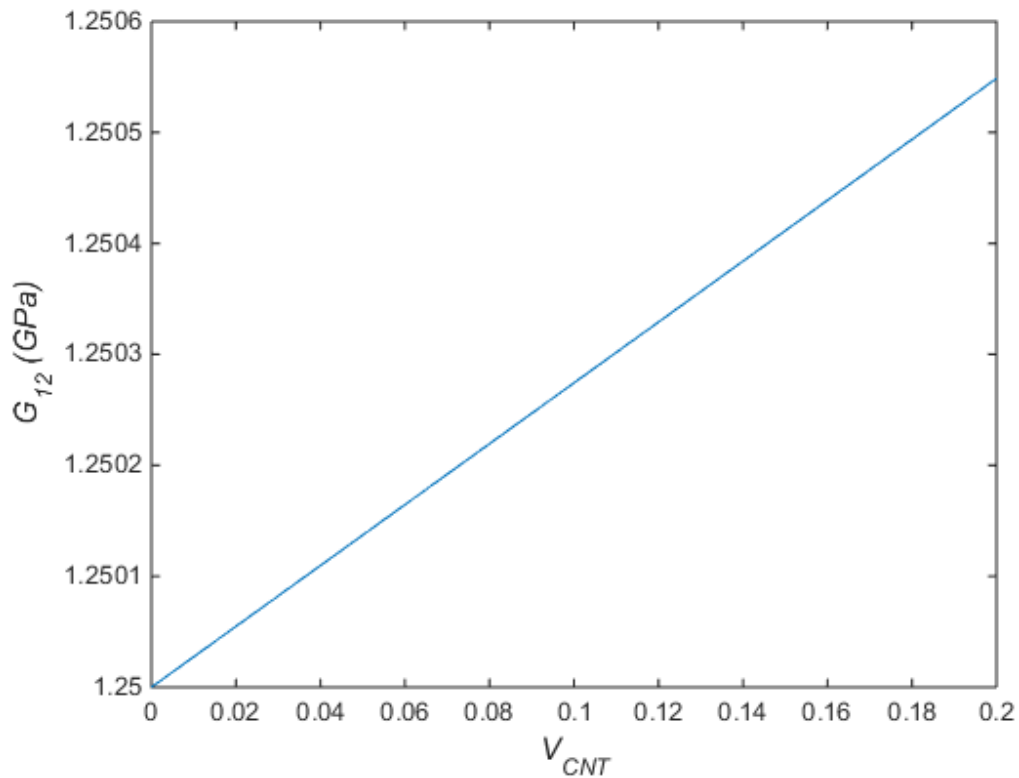


Figure 3-9: Randomly orientated carbon nanotube effective Shear modulus

3.5. Effect of agglomerated carbon nanotubes

Due to carbon nanotubes' small diameter and therefore high aspect ratio, they become very prone to agglomerate within an epoxy resin matrix. Ideally, in order to achieve uniform properties throughout a composite material, the reinforcement needs to be evenly dispersed, but this is not always possible. Micromechanical modelling techniques can be used to analyse the elastic moduli of nanocomposites where uneven dispersion is present. Previous studies such as those performed by Kamarian (2016), have found that an uneven dispersion of carbon nanotubes within a matrix tend to stick together and form spherical shapes, referred to as inclusions as seen in Figure 3-10.

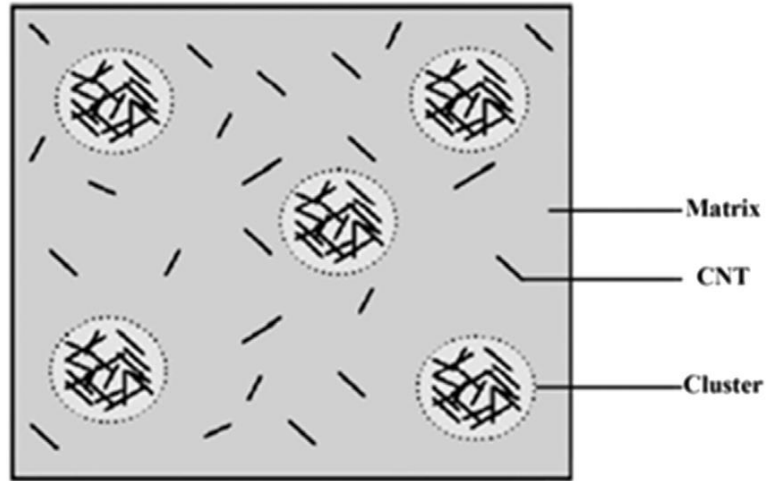


Figure 3-10: Eshelby's cluster model of CNTs (Kamarian 2016)

These zones of agglomerated carbon nanotubes result in areas with dissimilar material properties compared to the rest of the material. Therefore, it can be denoted that the total volume, V_{CNT}^{RVE} , of CNTs within the RVE can be broken into two parts, namely:

$$V_{CNT}^{RVE} = V_{CNT}^{inclusion} + V_{CNT}^M \quad (3.30)$$

Where $V_{CNT}^{inclusion}$ represents the volume of CNTs within the inclusion and V_{CNT}^M represents the volume of CNTs within the rest of the matrix. We can now denote two ratios (ξ and ζ) to describe the dispersion of nanotubes within a composite where agglomeration is present;

$$\xi = \frac{V_{inclusion}}{V} \quad (3.31)$$

and,

$$\zeta = \frac{V_{CNT}^{inclusion}}{V_{CNT}^{RVE}} \quad (3.32)$$

In the above set of equations $V_{inclusion}$ represents the volume of the inclusions within the RVE. When $\xi=1$, then the nanotubes within the matrix are evenly dispersed and as ξ decreases, more agglomeration is present. When $\zeta=1$, then all nanotubes within the matrix are located inside of the inclusions and if $\xi=\zeta$ then all nanotubes are dispersed uniformly. The average volume fraction (V_{CNT}) can be denoted as:

$$V_{CNT} = \frac{V_{CNT}^{RVE}}{V} \quad (3.33)$$

where V represents the total volume. The above equations can therefore be equated to:

$$\frac{V_{CNT}^{inclusion}}{V_{CNT}^{RVE}} = \frac{V_{CNT}\zeta}{\xi} \quad (3.34)$$

and,

$$\frac{V_{CNT}^m}{V - V_{inclusion}} = \frac{V_{CNT}(1 - \zeta)}{1 - \xi} \quad (3.35)$$

The micromechanical model is therefore based on the assumption that agglomeration occurs as spherical shaped inclusions within a matrix. To solve the system of equations, the inclusions and the matrix are solved individually and then the overall properties of the nanocomposite can be determined by combining the results thereafter. The effective elastic moduli of both the matrix and the inclusions are calculated using separate micromechanical equations. Assuming the nanotube orientation is completely random, the effective moduli of the inclusions, E_{in} , and their surrounds, E_{out} can be calculated as follows:

$$E_{out} = \frac{3}{8} \left\{ \frac{V_{CNT}(1 - \zeta)}{1 - \xi} E_{CNT} + \left[1 - \frac{V_{CNT}(1 - \zeta)}{1 - \xi} \right] E_M \right\} + \frac{5}{8} \left\{ \frac{(1 - \xi)E_{CNT}E_M}{[(1 - \xi) - V_{CNT}(1 - \zeta)]E_{CNT} + V_{CNT}(1 - \zeta)E_M} \right\} \quad (3.36)$$

and,

$$E_{in} = \frac{3}{8\xi} [V_{CNT}\zeta E_{CNT} + (\xi - V_{CNT}\zeta)E_M] + \frac{5}{8} \frac{\xi E_M E_{CNT}}{(\xi - V_{CNT}\zeta)E_{CNT} + V_{CNT}\zeta E_M} \quad (3.37)$$

Where both the reinforcement and the matrix are both isotropic, and E_{CNT} and E_M represent the Young's modulus of the CNTs and matrix respectively.

To analyse the matrix, a similar approach used to analyse straight, randomly orientated carbon nanotube composites will be employed. Thus, Mori-Tanaka techniques are once again implemented. It should be noted that the nanotubes are transversely isotropic. Due to the random nanotube orientation within the inclusions, it is assumed that the inclusions are also therefore isotropic. The effective shear moduli (G_{in} and G_{out}) and the effective bulk moduli (K_{in} and K_{out}) for both the matrix and inclusions can be determined using (Shi et al. 2004):

$$K_{in} = K_M + \frac{(\delta_r - 3K_M\alpha_r)V_{CNT}\zeta}{3(\xi - V_{CNT}\zeta + V_{CNT}\zeta\alpha_r)} \quad (3.38)$$

$$K_{out} = K_M + \frac{V_{CNT}(\delta_r - 3K_M\alpha_r)(1 - \zeta)}{3[1 - \xi - V_{CNT}(1 - \zeta) + V_{CNT}(1 - \zeta)\alpha_r]} \quad (3.39)$$

$$G_{in} = G_M + \frac{V_{CNT}\zeta(\eta_r - 2G_M\beta_r)}{2(\xi - V_{CNT}\zeta + V_{CNT}\zeta\beta_r)} \quad (3.40)$$

$$G_{out} = G_M + \frac{V_{CNT}(1 - \zeta)(\eta_r - 2G_M\beta_r)}{2[1 - \xi - V_{CNT}(1 - \zeta) + V_{CNT}(1 - \zeta)\beta_r]} \quad (3.41)$$

The Eshelby's tensors can then be determined for the spherically shaped inclusions in an isotropic matrix (Shi et al. 2004). Using the Eshelby's tensors K and G can be derived using the Mori-Tanaka approach as:

$$K = K_{out} \left[1 + \frac{\xi \left(\frac{K_{in}}{K_{out}} - 1 \right)}{1 + \alpha(1 - \xi) \left(\frac{K_{in}}{K_{out}} - 1 \right)} \right] \quad (3.42)$$

and,

$$G = G_{out} \left[1 + \frac{\xi \left(\frac{G_{in}}{G_{out}} - 1 \right)}{1 + \beta(1 - \xi) \left(\frac{G_{in}}{G_{out}} - 1 \right)} \right] \quad (3.43)$$

with,

$$\alpha = \frac{(1 + \nu_{out})}{3(1 - \nu_{out})} \quad (3.44)$$

and,

$$\beta = \frac{2(4 - 5\nu_{out})}{15(1 - \nu_{out})} \quad (3.45)$$

where ν_{out} is the hybrid matrix Poisson's ratio, denoted as:

$$\nu_{out} = \frac{3K_{out} - 2G_{out}}{2(3K_{out} + G_{out})} \quad (3.46)$$

Furthermore, the effective Young's modulus and Poisson's ratio can be determined using (Wuite 2005):

$$E = \frac{9KG}{3K + G} \quad (3.47)$$

and,

$$\nu = \frac{3K - 2G}{6K + 2G} \quad (3.48)$$

Using the above information, a computational model was developed using MATLAB R2014b depicting the influence of nanotube agglomeration on the material properties (Appendix A.1.2.). The CNT properties along with the composite constituent's properties can be seen in Table 3-2 and Table 3-1 respectively. The nanotubes were considered transversely isotropic. The representative values for the Hill's elastic moduli of the transversely isotropic nanotubes were taken as follows: $l_r=10$ GPa, $k_r=30$ GPa, $n_r=450$ GPa and $m_r=p_r=l$ GPa. Figure 3-11 shows the contour plots of the impact of nanotube agglomeration on the composite Young's moduli with respect to a uniformly distributed composite ($E_{agglomerated}/E_{distributed}$). Here the agglomerated composites are shown as a fraction of evenly distributed composites, where the nanotube volume fraction is 0.1 ($\zeta > \xi, \xi > c_r \zeta$) and the nanotubes are considered to be isotropic.

Figure 3-12, Figure 3-13 and Figure 3-14 analyse the impact of nanotube agglomeration on the Poisson's ration, Shear modulus and Elastic modulus respectively for increasing CNT volume fraction. Here it's seen that as the nanotube volume fraction increases so does the elastic and shear moduli. For the effective Poisson's ratio, at low nanotube volume fraction (up to 10%), a significant decrease can be observed. It should also be noted here that 40% nanotube agglomeration is used. Figure 3-15 depicts the effect of nanotube agglomeration (ranging from 0 to 100%) on the elastic modulus of the two-phase nanocomposite thus suggesting that as the agglomeration parameter increases so does the elastic modulus. This analysis was performed for 10% nanotube volume fraction.

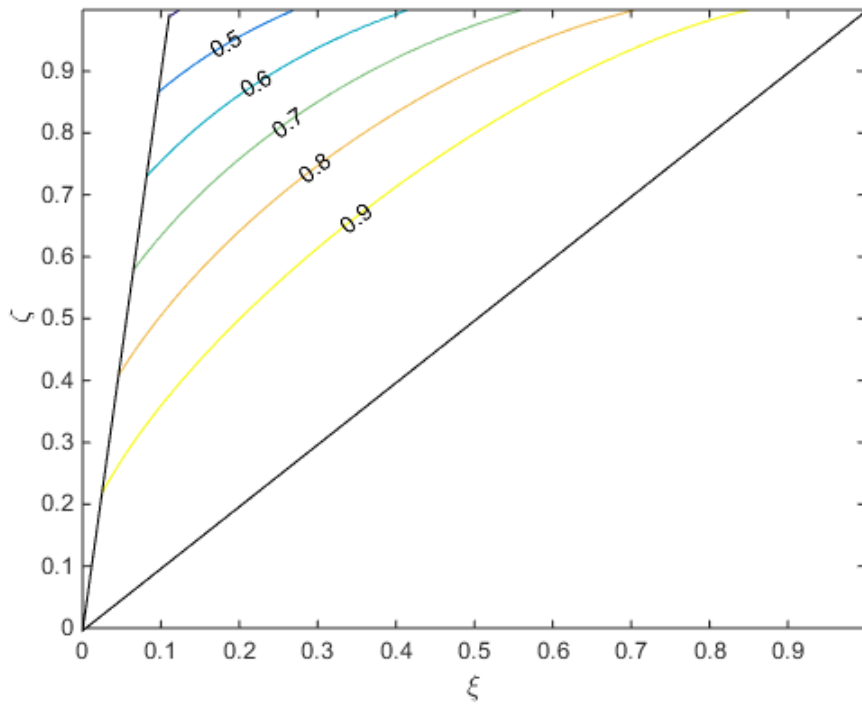


Figure 3-11: Contour plot depicting the effect of nanotube agglomeration on the Young's modulus with respect to a uniformly distributed composite ($E_{\text{agglomerated}}/E_{\text{distributed}}$)

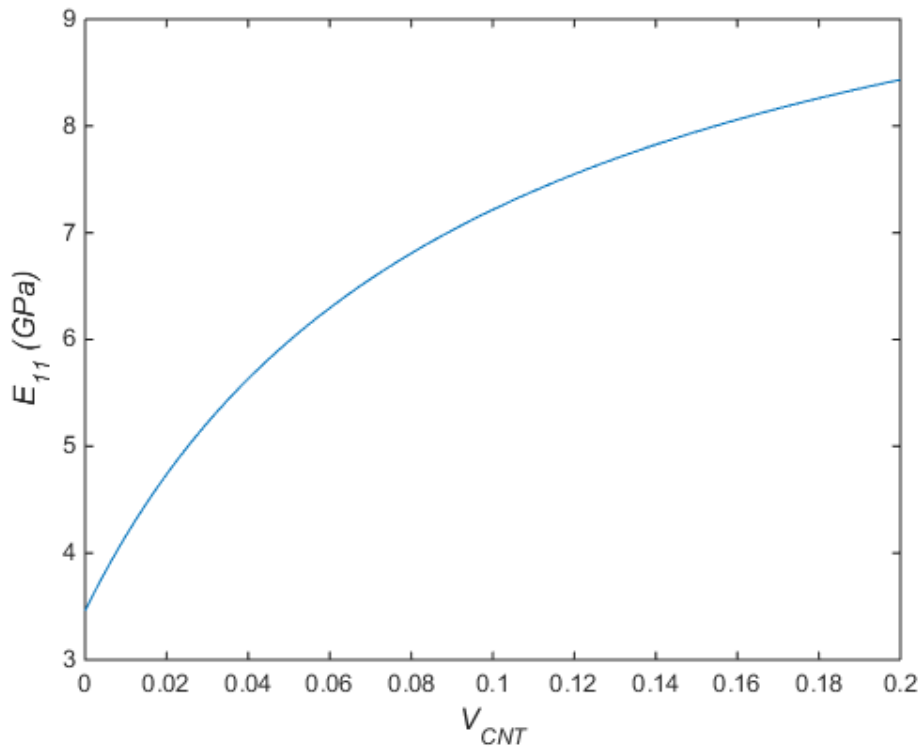


Figure 3-12: CNT agglomeration effect on the composite longitudinal modulus

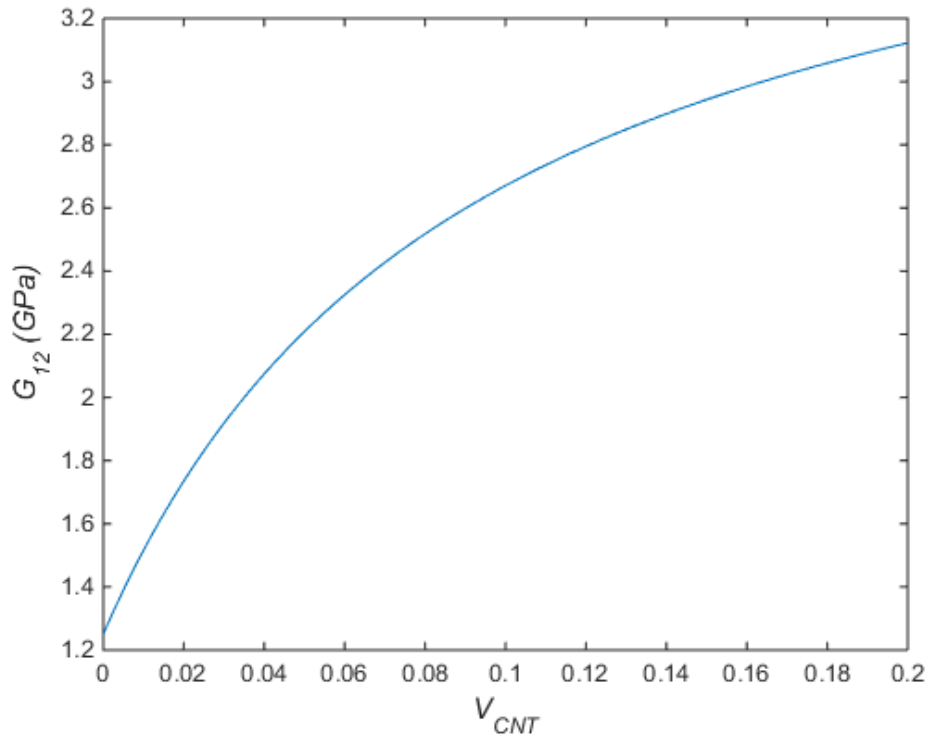


Figure 3-13: CNT agglomeration effect on the composite shear modulus

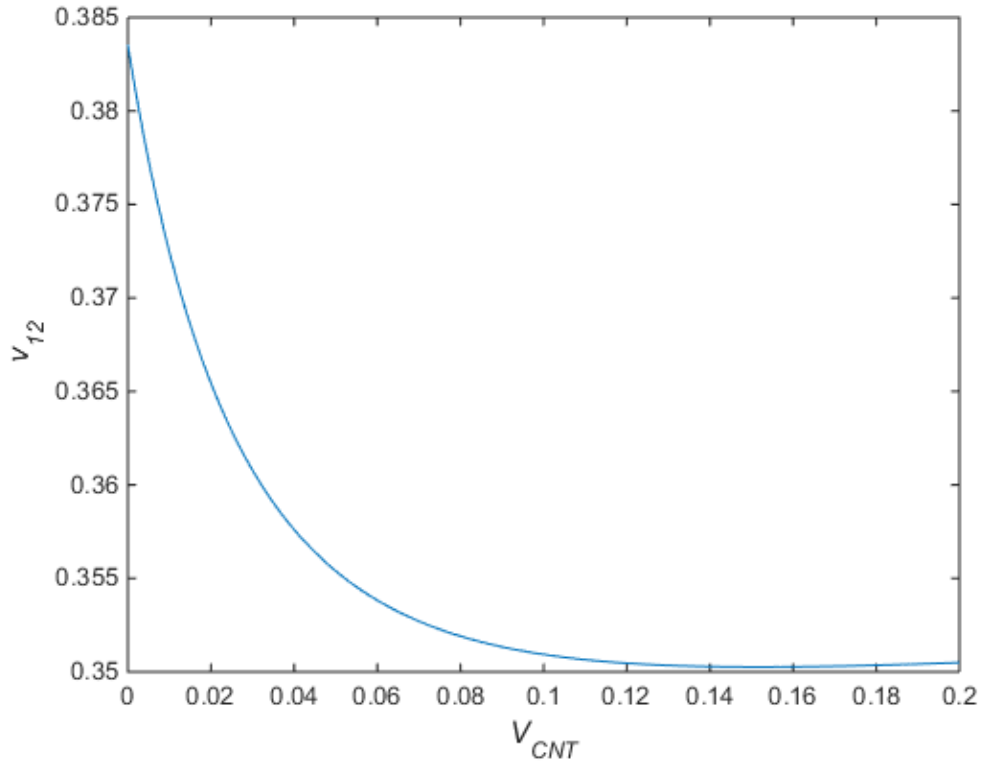


Figure 3-14: CNT agglomeration effect on the composite Poisson's ratio

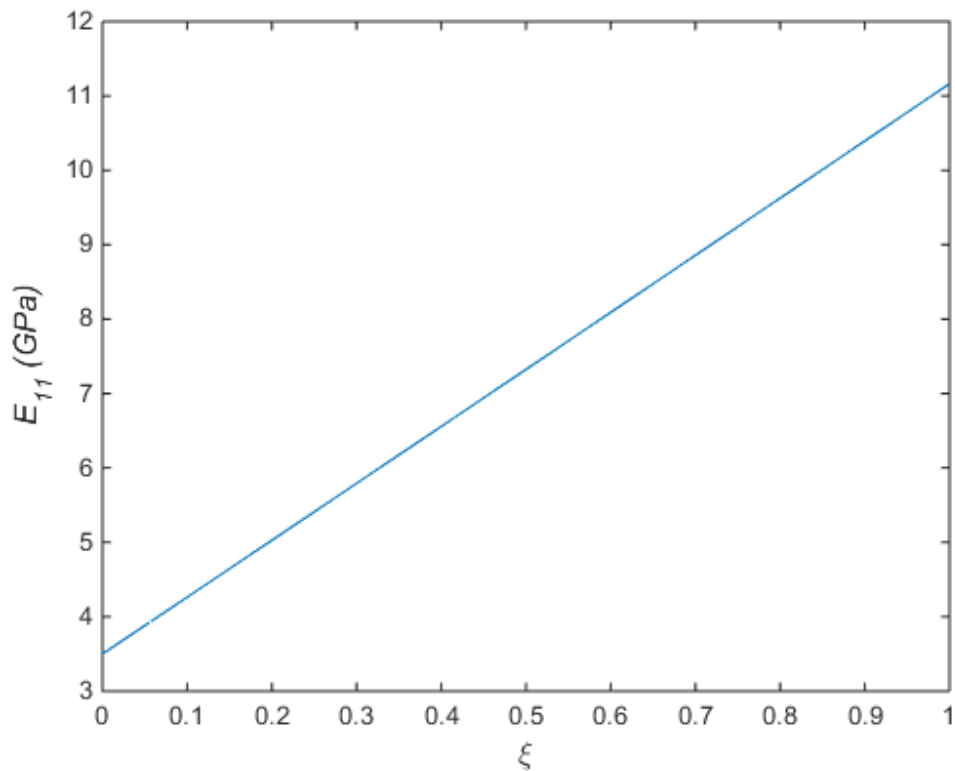


Figure 3-15: Nanotube agglomeration versus elastic modulus

Analysing Figure 3-11 reveals that the elastic modulus for the agglomerated carbon nanotube composite has a maximum value when the nanotubes are completely and evenly distributed within the matrix. As the level of agglomeration increases the elastic modulus decreases. It can also be noted from the data that a reduction in the stiffening effect of the nanotubes can be observed with an increasing nanotube volume fraction situated within the inclusions.

3.6. Chapter summary

The effects of CNT orientation and agglomeration on the flexural properties of CNT reinforced epoxy nanocomposites were examined using micromechanical methods. Epoxy matrix reinforced with evenly distributed, aligned CNTs, randomly orientated CNTs and agglomerated CNTs were analysed respectively. The straight, aligned CNT model showed a rapid increase in Young's longitudinal modulus for increasing nanotube volume fraction. Though, the transverse modulus normal to the fibre direction only increased initially with increasing nanotube volume fraction as a result of the transversely isotropic properties of nanotubes but tapered off significantly at roughly $V_{CNT}=0.007$.

Significant improvements in the elastic properties of epoxy were demonstrated for the addition of straight, randomly oriented CNTs. These results suggest the possibility of tailoring

the properties of CNT based composites by controlling the orientation of the nanotubes. However, assumptions such as the distribution, length and waviness need to be taken into account for a more detailed analysis. Experimental studies on nanotube-reinforced epoxy-based composites have shown limited ability to control the dispersion of CNTs within the matrix. The influence of distribution of the nanotubes within the matrix was analysed using Eshelby's inclusion model. Here, where the nanocomposite is assumed to contain spherical inclusions with concentrated nanotube clusters. Results showed a significant impact on the elastic properties when CNTs are concentrated in agglomerations.

The effective elastic modulus vs carbon nanotube weight fraction can be seen in Figure 3-16. Here, the effective elastic modulus determined using the model, is compared to practical results obtained by Shokrieh et al. (2017).

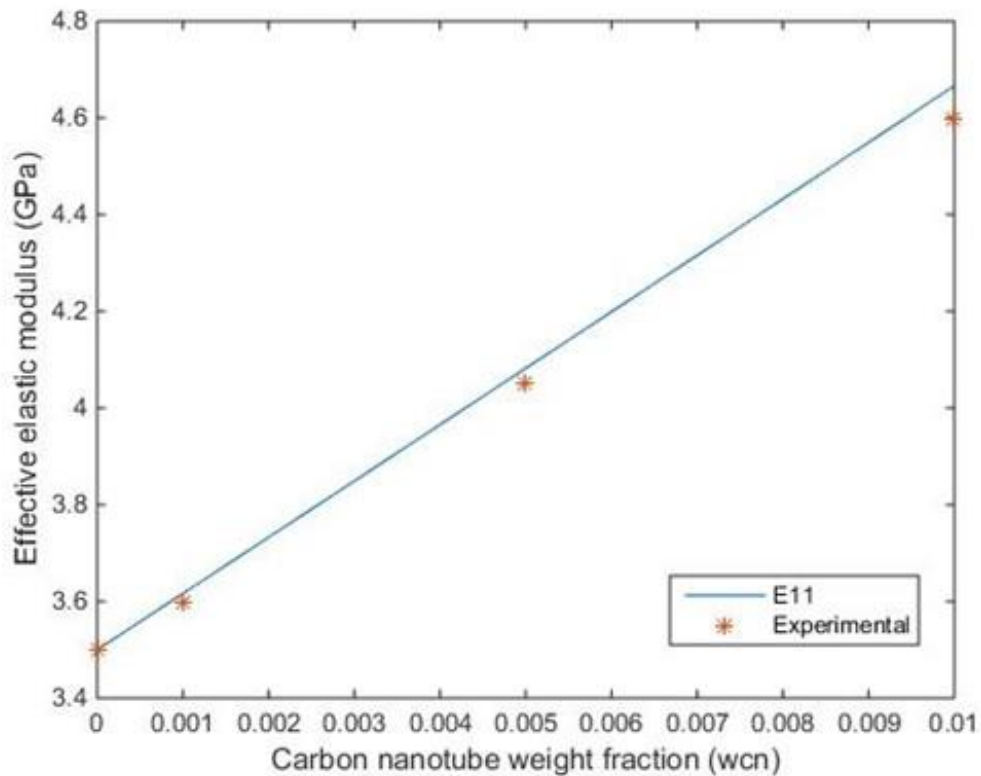


Figure 3-16: Randomly orientated CNT Young's modulus vs experimental data (Shokrieh et al. 2017)

Table 3-3 summarises the difference between the computationally obtained modelling data and experimental results. A good correspondence can be observed for the straight, randomly orientated nanotubes. It's seen here that as the nanotube volume fraction increases so does the effects of nanotube waviness.

Table 3-3: Randomly orientated CNT Young's modulus vs experimental data (Shokrieh et al. 2017)

	0 wt%	0.1 wt%	0.5 wt%	1 wt%
Experimental results (GPa)	3.5	3.6	4.05	4.6
Theoretical results (GPa)	3.5	3.614	4.079	4.666
% Difference	0	0.39	0.72	1.43

4. Three-phase micromechanical analysis

Experimental analyses are typically used to determine the impact of factors such as constituent material properties, volume fractions types and orientation of fibres on hybrid composites. However, these experiments require various composites of specific material properties to be fabricated which can be time consuming and costly. Developing computational micromechanical modelling techniques to allow for hybrid composites to be analysed using finite element simulations will therefore be beneficial. Micromechanical approaches to study the properties of nanocomposites have several advantages such as ease of use, low cost, and high accuracy making them ideal for analysing multiscale nanocomposites and laminates reinforced by CNTs and fibres.

Conventional composite analyses are typically single-stages analyses used to determine the material properties of two-phase composites, however with the addition of a third phase, conventional approaches need to be modified to account for the increased complexity of the composite. To accurately analyse hybrid composites, a multi-stage analyses is proposed. Hence, methods such as Rule of Hybrid Mixtures (RoHM) studied by Banerjee et al. (2014) were developed but found to be inadequate due to the linearity of their outputs, unable to take into account factors such as nanotube orientation and agglomeration. Since then other methods have been developed by extending on traditional two-phase techniques. Methods developed by Mori and Tanaka (1973) as well as Halpin and Kardos (1976) have been modified to account for the additional fibre constituent.

The stiffness of a fibre-matrix volume fraction is not impacted much by the change in fibre location but more so by its direction since the elastic constants of a nanocomposite are volume averaged over the constituent micro-phases. Thus, in this chapter the effects of fibre orientation and agglomeration on the flexural behaviour of three-phase hybrid nanocomposites will be investigated. The results obtained here will be used to determine the effectiveness of three-phase nanocomposites by comparing it to traditional materials and composites by applying the results obtained in this chapter to structural applications.

4.1. Three-phase, aligned CNT micromechanical analysis

For this approach a hexagonal fibre stacking sequence is assumed. This results in the mechanical properties to be similar in any direction normal to the fibre therefore resulting in transverse isotropy material properties (Shi et al. 2004). It is assumed that the matrix fills up all the voids and cavities within the RVE. For the sake of this analysis the hexagonal pattern was

opted for because of its ability to accurately represent the transverse isotropy of the nanotubes as opposed to a square stacking sequence (Elbadry et al. 2018). The hybrid composite can be altered by varying the volume fraction of both the CNTs and fibre reinforcement within the epoxy matrix to achieve desired material properties. Here, both carbon and glass fibres are modelled.

Figure 4-1 depicts the micromechanical technique used in analysing the aligned CNT, three-phase nanocomposite. Here, a single-stage modelling approach is opted for because of the nature of the fibre and nanotube orientation.

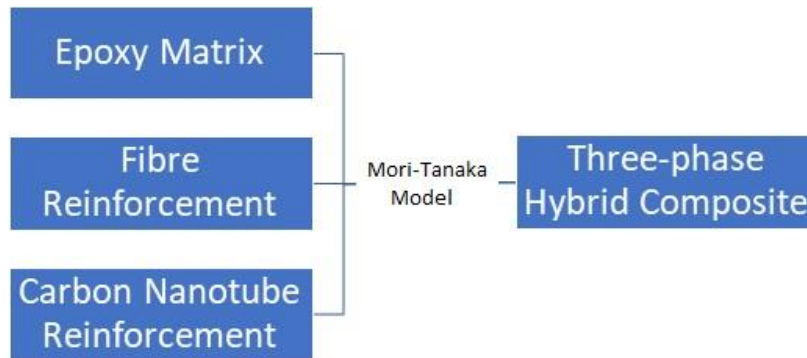


Figure 4-1: Three-phase, aligned CNT modelling approach

Assumptions like same size and even distribution of the fibres as well as absence of voids are made to reduce the computational cost of the analysis, however these assumptions should still allow for reasonably accurate results. These assumptions also allow for a 2D analysis to be performed. Furthermore, fibre undulation and waviness are not taken into consideration. The elastic modulus of the nanocomposite is analysed through varying the CNT and fibre reinforcement respectively.

4.1.1. Evaluating the engineering constants

The nanocomposite is subjected to a uniform strain at the macroscopic level known as macro-strains (ε^M), with equivalent stresses called macro-stresses (σ^M). The macro-stresses are the average stresses needed to produce a state of macro-deformations (Banerjee et al. 2014). The macro-strains and macro-stresses follow the relation:

$$\{\sigma^M\} = [C]\{\varepsilon^M\} \quad (4.1)$$

where [C] represents the stiffness matrix of the homogenised nanocomposite. The compliance matrix, [S], can be obtained by inverting the stiffness matrix. Furthermore, the elastic constants can therefore be calculated using the relation:

$$[C]^{-1} = \begin{bmatrix} \frac{1}{E_{11}} & -\nu_{12} & -\nu_{13} & 0 & 0 & 0 \\ \frac{E_{11}}{-\nu_{21}} & \frac{1}{E_{11}} & \frac{-\nu_{23}}{E_{11}} & 0 & 0 & 0 \\ \frac{E_{22}}{-\nu_{31}} & \frac{E_{22}}{-\nu_{32}} & \frac{1}{E_{22}} & \frac{1}{G_{23}} & 0 & 0 \\ \frac{E_{33}}{0} & \frac{E_{33}}{0} & \frac{E_{33}}{0} & 0 & \frac{1}{G_{13}} & \frac{1}{G_{12}} \\ 0 & 0 & 0 & 0 & 0 & 0 \\ 0 & 0 & 0 & 0 & 0 & 0 \\ 0 & 0 & 0 & 0 & 0 & 0 \end{bmatrix} \quad (4.2)$$

where E_{11} , ν_{12} , E_{22} , E_{33} and G_{12} represent the longitudinal modulus, Poisson's ratio, transverse moduli (in both directions) and the shear modulus of the hybrid composite respectively. For a nanocomposite to demonstrate transversely isotropic behaviour in the 2–3 plane, it needs to adhere to the following relation:

$$G_{23} = \frac{E_{22}}{2(1 + \nu_{23})} \quad (4.3)$$

This is due to the hexagonal packing of the fibre as this arrangement better represents isotropy in the 2–3 plane. RoHM is utilised to determine the longitudinal Poisson's ratios (ν_{12}) as well as the longitudinal modulus (E_{11}). The Halpin-Tsai approach is then used to calculate the transverse modulus E_{22} , and shear moduli G_{12} , G_{13} and G_{23} . The Halpin-Tsai equation were altered to better calculate the results obtained from the FEA after analysing experimental results. The RoHM can be stated as:

$$E_{11} = E_{11F}V_F + E_{11CNT}V_{CNT} + E_MV_M \quad (4.4)$$

where E_{11F} , E_{11CNT} and E_M represents the longitudinal moduli for fibre, CNTs and matrix respectively, and V_F , V_{CNT} and V_M represents the fibre volume fraction, CNT volume fraction and matrix volume fraction respectively. Originally the Halpin-Tsai semi-empirical equations were used to determine the transverse modulus (E_{22}) as:

$$\frac{E_{22}}{E_M} = \frac{1 + \zeta\eta V_F}{1 - \eta V_F} \quad (4.5)$$

where,

$$\eta = ((E_F/E_M) + 1)/((E_F/E_M) + \zeta) \quad (4.6)$$

ζ represents a curvature fitting parameter which depends on the fibre packing arrangement. As mentioned above, to more accurately represent the transverse modulus, Eq. (4.5) was modified accordingly

$$\frac{E_{22}}{E_M} = \frac{1 + \zeta(\eta_F V_F + \eta_{CNT} V_{CNT})}{1 - (\eta_F V_F + \eta_{CNT} V_{CNT})} \quad (4.7)$$

where,

$$\eta_F = ((E_{11F}/E_M) - 1)/((E_{11F}/E_M) + \zeta) \quad (4.8)$$

and,

$$\eta_{CNT} = ((E_{11CNT}/E_M) - 1)/((E_{11CNT}/E_M) + \zeta) \quad (4.9)$$

Subscripts 'F', 'CNT' and 'M' refers to the fibre, carbon nanotubes and matrix respectively. Additionally, the optimal value of ζ was calculated utilising a least square error approach and it was calculated that $\zeta = 1.165$ produced good results for E_{22} (Banerjee et al. 2014). The Poisson's ratios ν_{12} and ν_{13} can be calculated using the RoHM as follows:

$$\nu_{12} = \nu_{12F} V_F + \nu_{12CNT} V_{CNT} + \nu_M V_M \quad (4.10)$$

where ν_{12F} , ν_{12CNT} and ν_M depicts the Poisson's ratio of the fibre, CNTs and matrix respectively. Furthermore, the shear modulus (G_{12}) can be calculated as shown by Eq. (4.11).

$$\frac{G_{12}}{G_M} = \frac{1 + \zeta(\eta_F V_F + \eta_{CNT} V_{CNT})}{1 - (\eta_F V_F + \eta_{CNT} V_{CNT})} \quad (4.11)$$

where,

$$\eta_F = ((G_{12F}/G_M) - 1)/((G_{12F}/G_M) + \zeta) \quad (4.12)$$

and,

$$\eta_{CNT} = ((G_{12CNT}/G_M) - 1)/((G_{12CNT}/G_M) + \zeta) \quad (4.13)$$

The corresponding fibre shear moduli as stated in Table 3-1 is used in determining the parameter η . The optimum value of ζ was calculated as 1.01 for G_{12} and G_{13} , and 0.9 for G_{23} (Banerjee et al. 2014). Note that the Poisson's ratio ν_{23} can also be calculated using G_{23} and E_{22} if required.

4.1.2. Results

Computational software, MATLAB R2014b was used to develop a script file to analyse the impact of straight, aligned CNTs on the mechanical properties of three-phase nanocomposites reinforced with either glass or carbon fibres in an epoxy matrix. Figure 4-2 depicts the effective longitudinal modulus for increasing nanotube volume fraction of three-phase nanocomposites.

It should be noted that for the analysis performed a curvature fitting parameter of 1.165 was used. Figure 4-2 shows a linear increase of the longitudinal moduli for increasing nanotube volume fraction from 0 to 20%. Here, 30% glass fibre reinforced composite is the weakest whereas the composite containing 60% carbon fibre reinforcement is considered the strongest. This is due to the excellent mechanical properties of carbon fibre reinforcement as compared to that of glass fibre. Figure 4-3 depicts the composite's transverse modulus for increasing CNT volume fraction. It can clearly be seen here that as nanotube volume fraction increase so does the transverse modulus exponentially. A significant increase in the transverse modulus can be observed for both 60% carbon and glass fibre reinforced composites respectively. A significant difference between the longitudinal and transverse moduli can be observed as this is due to the CNT material properties.

Figure 4-4 shows the shear modulus for increasing CNT volume fraction. Similar to the transverse modulus, the shear modulus increases exponentially for increasing CNT volume fraction. It's seen here that the type of fibre reinforcement has little impact on the shear moduli of the hybrid composite. This is due to the shear moduli of both carbon and glass fibre being similar. More so the fibre volume fraction has a more significant impact on the shear moduli. For low volume fractions of fibre reinforcement (30%) the shear modulus is nearly the same for both glass and carbon reinforced nanocomposites.

Lastly, Figure 4-5 depicts the Poisson's ratio of the three-phase composite for increasing nanotube volume fraction. Variations in type and volume fraction of fibre reinforcement were also analysed. Here the Poisson's ratio demonstrates a decreasing linear trend as the nanotube volume fraction increases (0 to 20%). It can be remarked that for both increasing fibre and nanotube volume fraction the Poisson's ratio decreases.

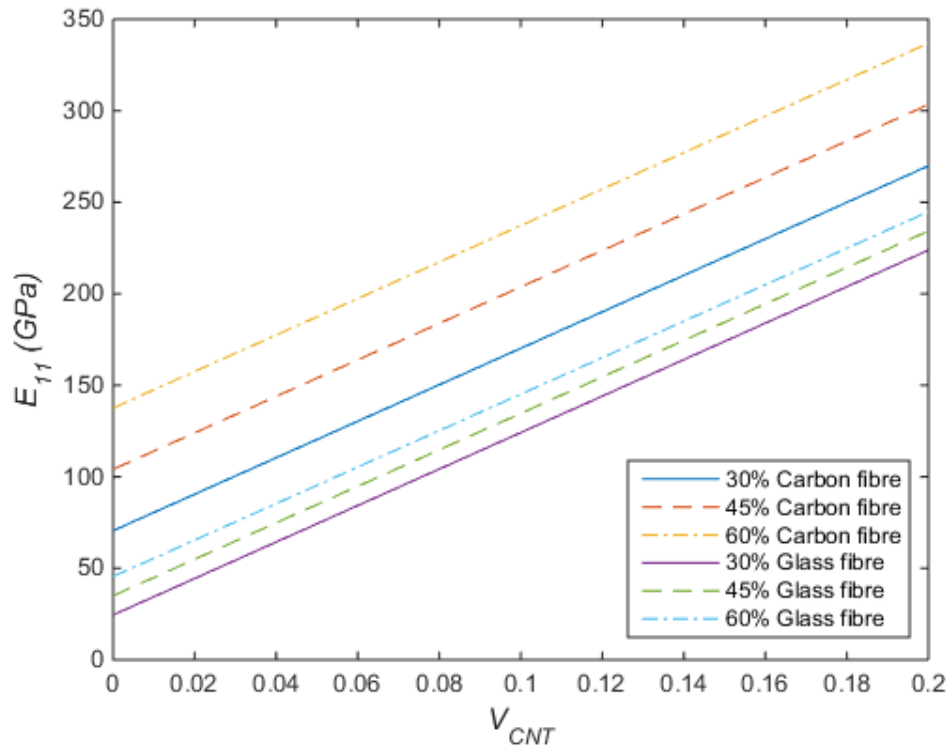


Figure 4-2: Three-phase aligned nanocomposite effective longitudinal modulus

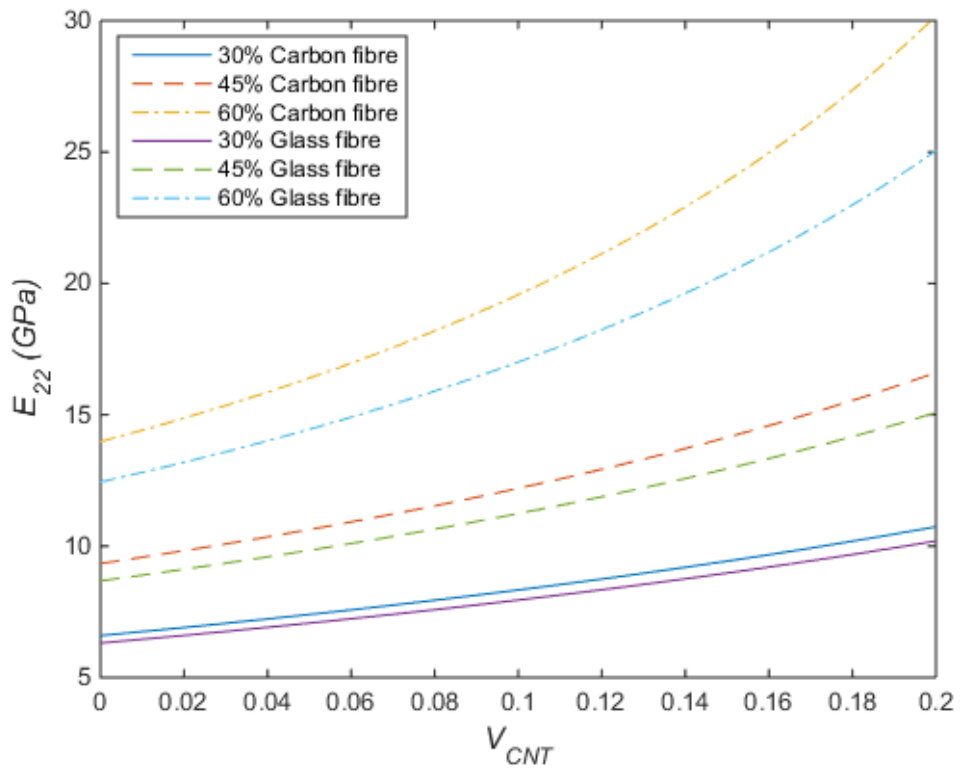


Figure 4-3: Three-phase aligned nanocomposite effective transverse modulus

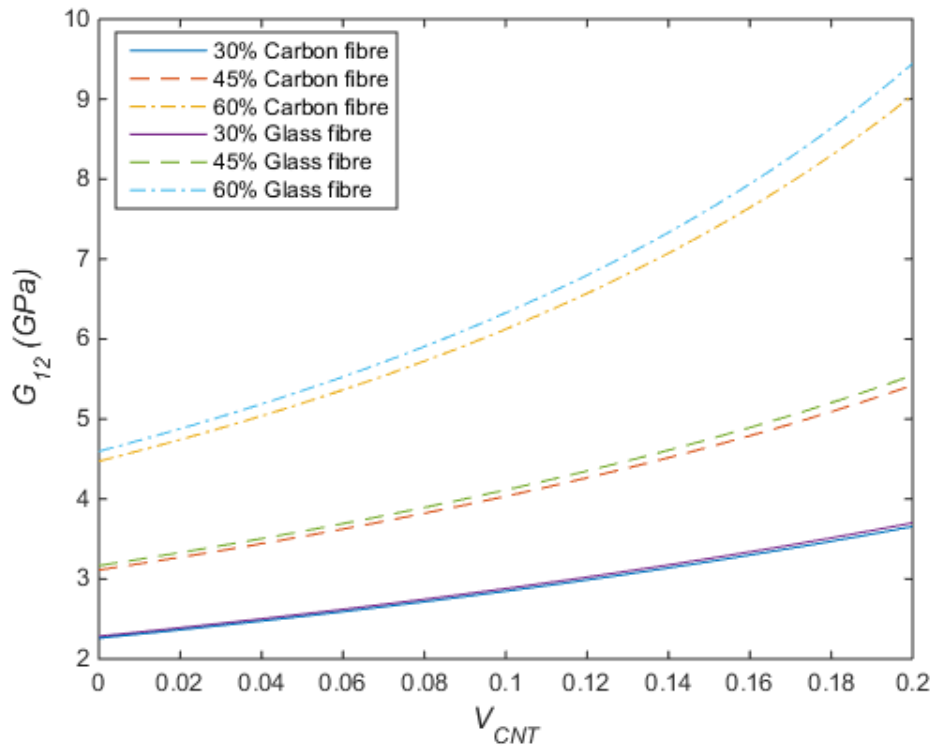


Figure 4-4: Three-phase aligned nanocomposite effective shear modulus

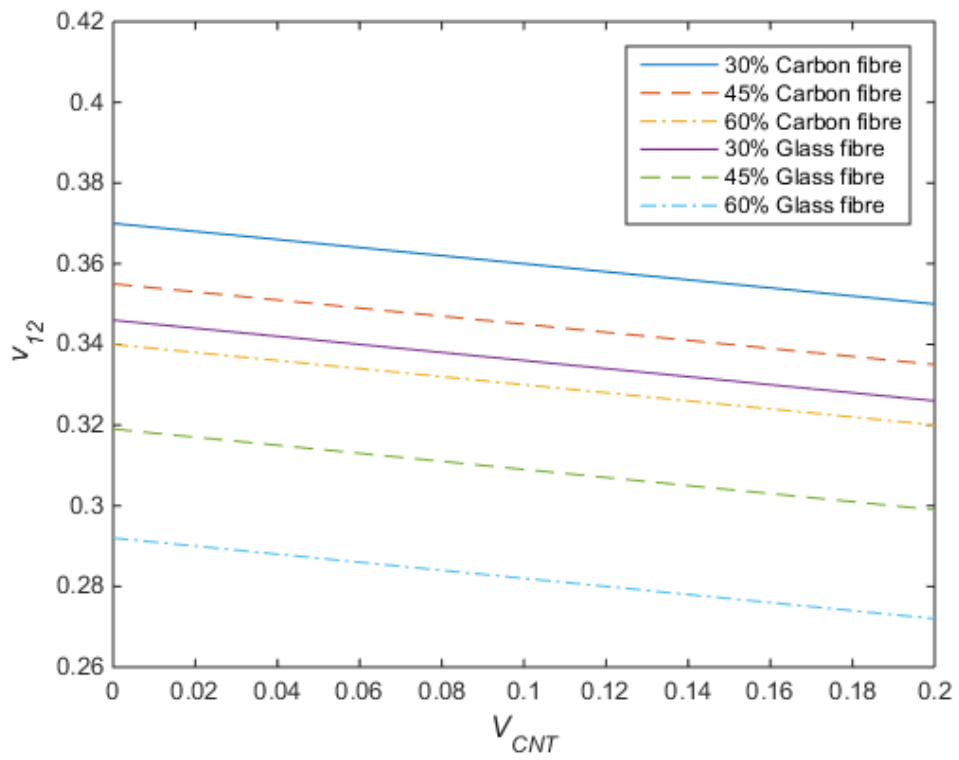


Figure 4-5: Three-phase aligned nanocomposite effective Poisson's ratio

4.2. Three-phase, randomly orientated CNT micromechanical analysis

The analysis performed in this section takes into consideration the effects of randomly orientated CNTs within a hybrid composite material. A modified Halpin-Tsai micromechanical analysis is employed to analyse the effects of varying types and quantities of reinforcement. The hybrid composite analysed below comprises of a CNT/ fibre/ epoxy three-phase composite where both glass and carbon fibre reinforcement will be analysed. Properties such as the Shear modulus, Poisson's ratio and Young's moduli of the three-phase composite will be studied. Figure 4-6 visually depicts the modelling approach utilised in order to perform the multi-stage analysis effectively. Firstly, a two-phase analysis, as performed in chapter 3.4, will be used, after which a micromechanical modelling approach will be implemented to further the analysis to a multi-stage, hybrid composite analysis.

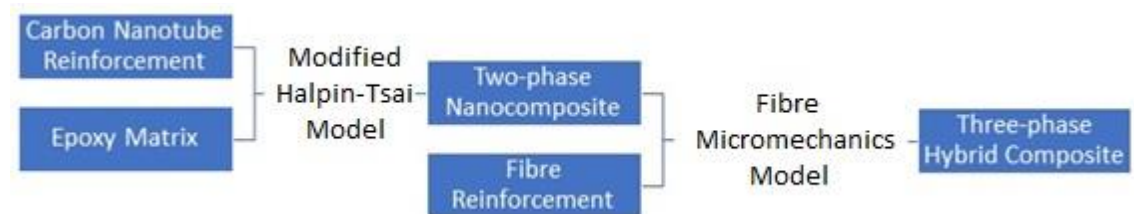


Figure 4-6: Micromechanical modelling of three-phase composite reinforced by randomly orientated CNTs and fibres

4.2.1. Evaluating the engineering constants

A CNT/ fibre reinforced epoxy composite (CNTFEC), composes of an isotropic matrix (epoxy), CNTs and fibres either of carbon or glass nature. Furthermore, the CNTFEC bonding and reinforcement dispersion within the matrix are assumed to be perfect. Additionally, it is also assumed that no voids are present, and all fibres are straight rods with the same respective elastic properties throughout and length-to-radius ratio, therefore no waviness is taken into account. It is assumed that the constituent materials adhere to the linear elastic behaviour throughout the deformation. To determine the CNTFEC elastic properties, the mechanical properties are considered to be orthotropic and as such the modified Halpin-Tsai technique in combination with the micromechanics modelling method is employed to derive the following set of equations (Gholami et al. 2018):

$$E_{11} = V_F E_{11F} + V_{MCNT} E_{MCNT} \quad (4.14)$$

$$\frac{1}{E_{22}} = \frac{V_F}{E_{22F}} + \frac{V_{MCNT}}{E_{MCNT}} - V_F V_{MCNT} \quad (4.15)$$

$$* \frac{v_F^2 E_{MCNT}/E_{22F} + v_{MCNT}^2 E_{22F}/E_{MCNT} - 2v_F v_{MCNT}}{V_F E_{22F} + V_{MCNT} E_{MCNT}}$$

$$\frac{1}{G_{12}} = \frac{V_F}{G_{12F}} + \frac{V_{MCNT}}{G_{MCNT}} \quad (4.16)$$

$$v_{12} = V_F v_F + V_{MCNT} v_{MCNT} \quad (4.17)$$

$$\rho = V_F \rho_F + V_{MCNT} \rho_{MCNT} \quad (4.18)$$

where, the associated volume fraction and material properties are denoted by F (fibre), CNT (carbon nanotube) and MCNT (matrix-carbon nanotube) respectively. The Young's moduli of the MCNT nanocomposite can be determined using the modified Halpin–Tsai equation (Gholami et al. 2018):

$$E_{MCNT} = \frac{E_M}{8} \left[5 \left(\frac{1 + 2\beta_{ad} V_{CNT}}{1 - \beta_{ad} V_{CNT}} \right) + 3 \left(\frac{1 + 2(l_{CNT}/d_{CNT})\beta_{dl} V_{CNT}}{1 - \beta_{dl} V_{CNT}} \right) \right] \quad (4.19)$$

where,

$$\beta_{dl} = \frac{(E_{11CNT}/E_M) - (d_{CNT}/4t_{CNT})}{(E_{11CNT}/E_M) + (l_{CNT}/2t_{CNT})} \quad (4.20)$$

and,

$$\beta_{ad} = \frac{(E_{11CNT}/E_M) - (d_{CNT}/4t_{CNT})}{(E_{11CNT}/E_M) + (d_{CNT}/2t_{CNT})} \quad (4.21)$$

in which t_{CNT} , d_{CNT} and l_{CNT} represents the nanotube thickness, outer diameter and length. The volume fraction and longitudinal modulus of the nanotubes are denoted by V_{CNT} and E_{11CNT} respectively. The volume fraction and Young's modulus of the isotropic epoxy matrix are denoted by V_M and E_M respectively. The CNT volume fraction can be determined using:

$$V_{CNT} = \frac{w_{CNT}}{w_{CNT} + (\rho_{CNT}/\rho_M) - (\rho_{CNT}/\rho_M)w_{CNT}} \quad (4.22)$$

where w_{CNT} , ρ_{CNT} and ρ_M represent the CNT mass fraction, mass density and matrix mass density respectively. The mass density and Poisson's ratio of the MCNT composite can be determined as follows:

$$\rho_{MCNT} = V_{CNT}\rho_{CNT} + V_M\rho_M \quad (4.23)$$

and,

$$\nu_{MCNT} = \nu_M \quad (4.24)$$

Since the volume fraction of nanotubes are minimal (usually less than 20%), the Poisson's ratio of the MCNT composite is assumed to be equal to that of the matrix (Gholami et al. 2018).

4.2.2. Results

A MATLAB R2014b script file (Appendix A.1.3.) was developed to analyse the effect of straight, randomly orientated nanotubes on the flexural behaviour of three-phase nanocomposites reinforced with either carbon or glass fibres in an epoxy matrix. Note that uniformly distributed reinforcement with no debonding is observed. The effective longitudinal modulus for increasing nanotube volume fraction, and for 30%, 45% and 60% fibre reinforcement is studied in Figure 4-7. Here it can be observed that for the 60% carbon fibre reinforced composite, only a 3.5% increase in the longitudinal modulus is found for an increase in CNT volume fraction (0 to 0.2). however, for a 30% glass fibre reinforced composite, a 36.5% increase in longitudinal modulus is observed for increasing CNT volume fraction from 0 to 0.2. thus, the nanotube reinforcement has a more significant impact on the glass fibre reinforced composites.

Figure 4-8 shows the transverse modulus for increasing CNT volume fraction. Here, increase in nanotube volume fraction follows a similar trend for glass fibre reinforced composites. However, for carbon fibre reinforced composite, the increase in nanotube volume fraction has less of an impact and thus the increase in transverse modulus is less. It should be noted that for nanotube volume fraction equal to 0.06, the carbon fibre reinforced composites for 30%, 45% and 60% all carry the same transverse modulus of 8.05 GPa.

The shear modulus for increasing nanotube volume fraction can be observed in Figure 4-9. Here, once again the shear modulus is observed to increase for increasing nanotube volume fraction. However, the type of fibre (glass or carbon) has little impact on the shear modulus compared to the impact of increasing fibre volume fraction. This is due to the similar shear mechanical properties of both carbon and glass fibres.

Lastly, the Poisson's ratio is observed for increasing nanotube volume fraction (Figure 4-10). Here a slight, nearly insignificant decrease in the Poisson's ratio is observed. Both the type and volume fraction of fibre plays a more influential role compared to the nanotube volume fraction.

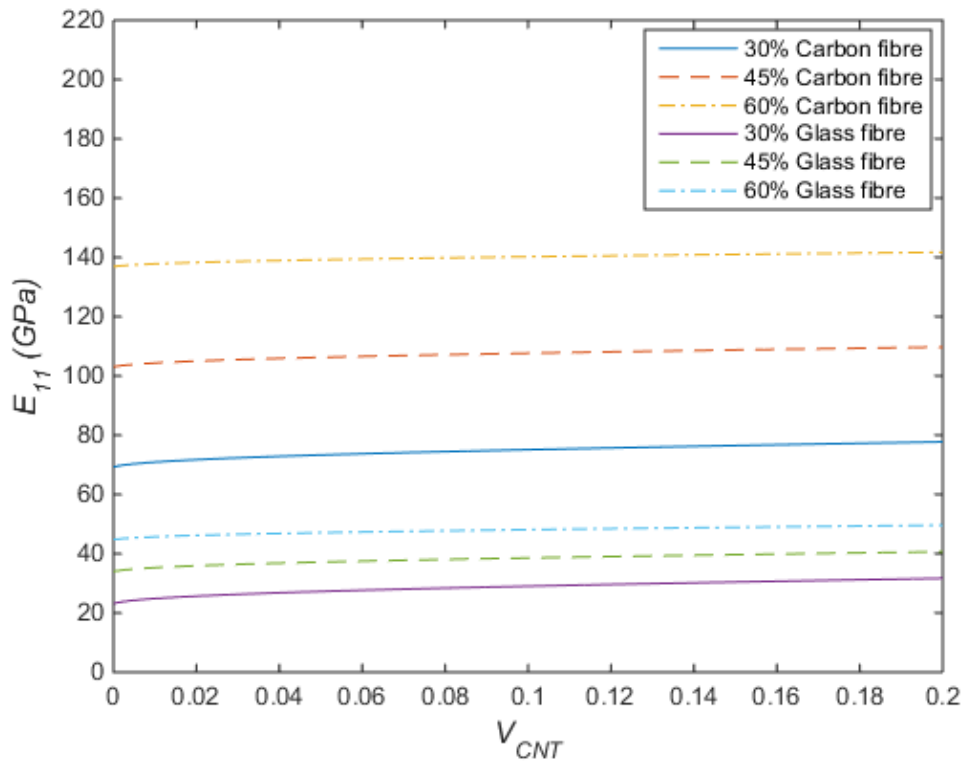


Figure 4-7: Three-phase randomly orientated nanocomposite effective longitudinal modulus

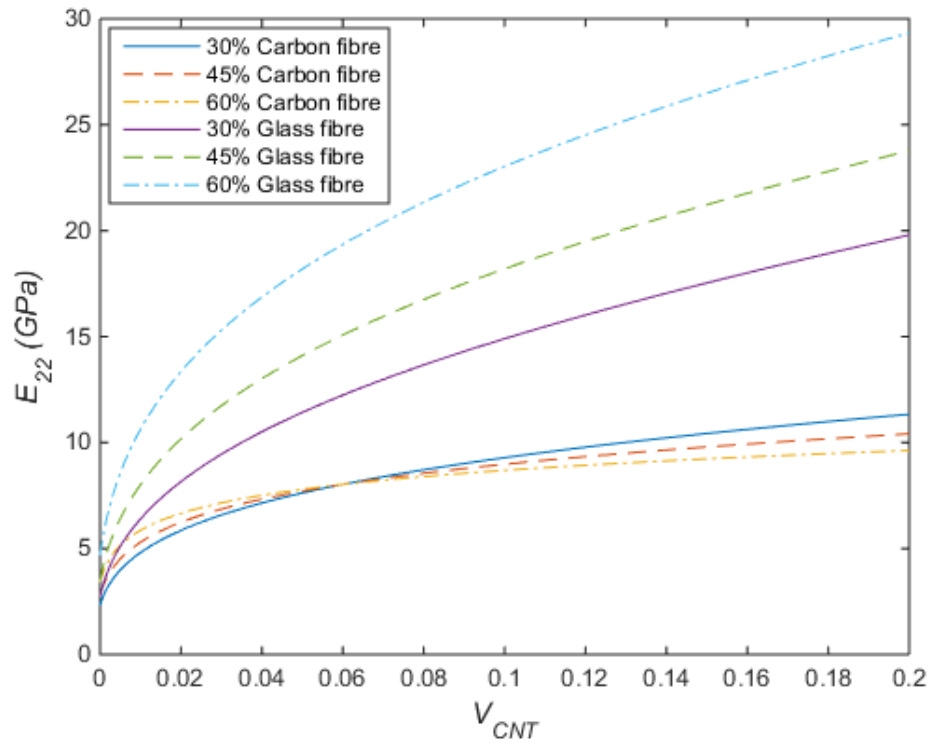


Figure 4-8: Three-phase randomly orientated nanocomposite effective transverse modulus

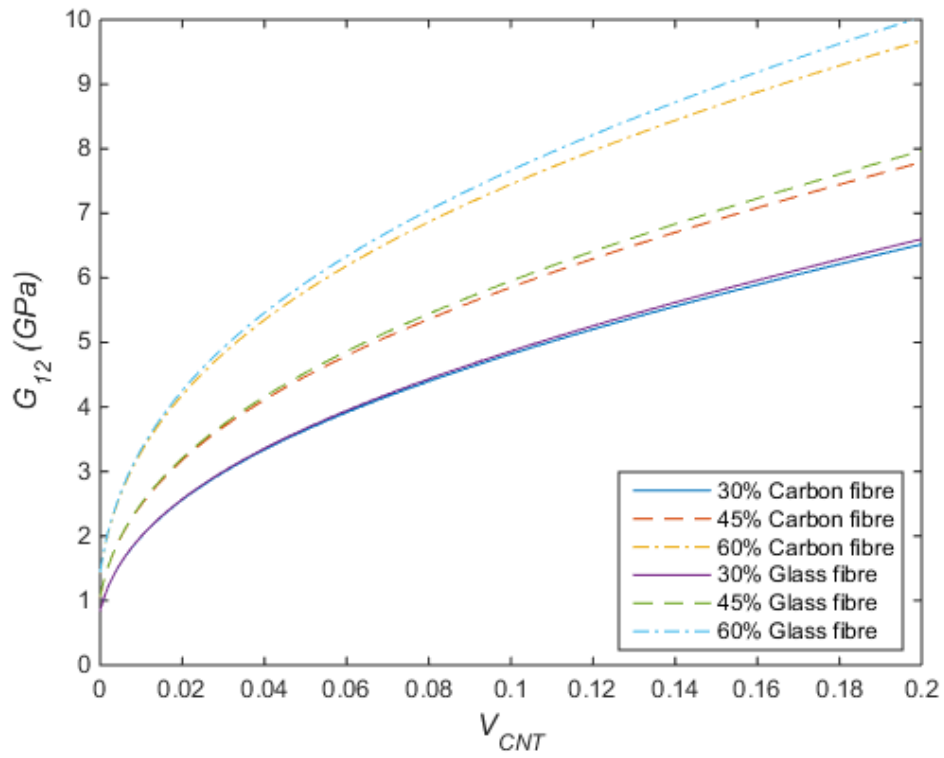


Figure 4-9: Three-phase randomly orientated nanocomposite effective shear modulus

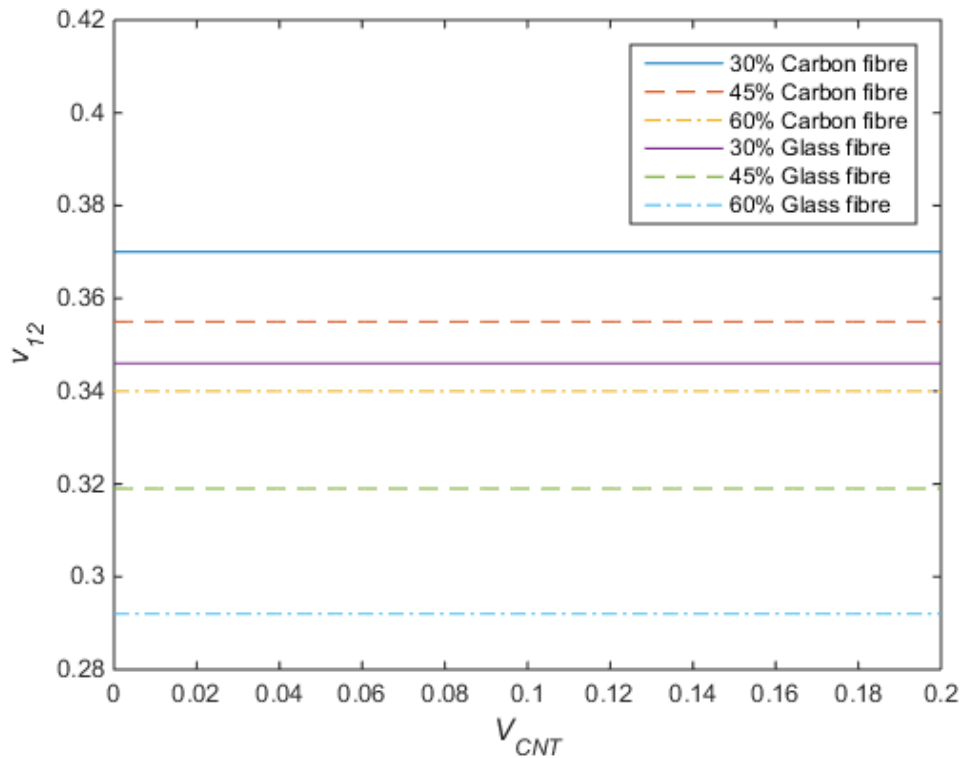


Figure 4-10: Three-phase randomly orientated nanocomposite effective Poisson's ratio

4.3. Effect of CNT agglomeration on the mechanical properties of hybrid nanocomposites

In this analysis, the effect of nanotube agglomeration on multi-scale nanocomposites reinforced by CNTs is studied. A two-stage analysis (Figure 4-11) is performed where the Mori-Tanaka technique is used to predict the elastic properties of three-phase CNTFEC. The efficiency and accuracy of the applied approach is studied and compared to experimental data and two-phase results reported previously. The influences of volume fraction, nanotube agglomeration and fibre type (carbon and glass) are examined.

It is assumed that the nanotubes are transversely isotropic. It is also assumed that the matrix fills all voids. A similar modelling technique, to the modified Halpin-Tsai analysis, is implemented where the volume fraction of both the nanotubes and fibre reinforcement within the epoxy matrix can be altered to achieve desirable material properties.

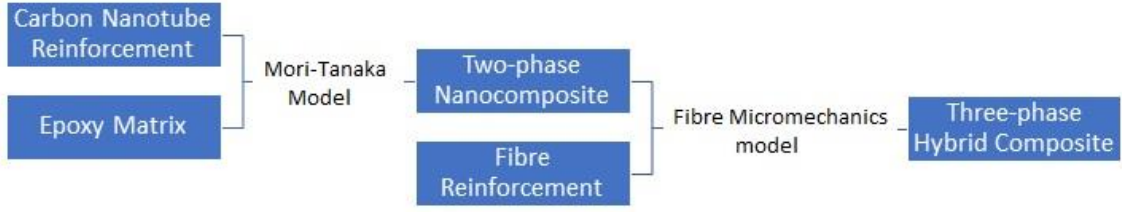


Figure 4-11: Micromechanical modelling approach of three-phase composites reinforced by agglomerated CNTs and fibres

Additional assumptions include same size and location of the fibres to decrease the cost of the 2D analysis. Fibre undulation and waviness is not taken into consideration, to place emphasis on the agglomeration effect of CNTs. The elastic moduli, shear modulus and Poisson's ratio are analysed to determine the bending characteristics of the hybrid composite.

4.3.1. Evaluating the engineering constants

As depicted by Figure 4-11, the second iteration of the three-phase analysis uses a micromechanics approach which yields the following set of equations (Seidi et al. 2017):

$$E_{11} = E_F V_F + E_{MCNT} V_{MCNT} \quad (4.25)$$

$$\frac{1}{E_{22}} = \frac{V_F}{E_{22F}} + \frac{V_{MCNT}}{E_{MCNT}} - V_{MCNT} V_F \quad (4.26)$$

$$* \frac{(v)^2 E_{MCNT}/E_{22F} + (v_{MCNT})^2 E_{22F}/E_{MCNT} - 2v_F v_{MCNT}}{E_{22F} V_F + E_{MCNT} V_{MCNT}}$$

$$\frac{1}{G_{12}} = \frac{V_F}{G_{12F}} + \frac{V_{MCNT}}{G_{12MCNT}} \quad (4.27)$$

$$v_{12} = V_F v_F + V_{MCNT} v_{MCNT} \quad (4.28)$$

$$\rho = V_F \rho_F + V_{MCNT} \rho_{MCNT} \quad (4.29)$$

where, F and MCNT stand for fibre and matrix-CNT nanocomposite respectively. ρ represents the mass density. This analysis takes into account the agglomeration of the CNTs thus introducing the following parameters:

$$\mu = \frac{V_{cluster}}{V} \quad (4.30)$$

and,

$$\eta = \frac{V_{CNT\ cluster}}{V_{CNT}} \quad (4.31)$$

where, V denotes the volume of the RVE, V_{CNT} the total CNT volume, $V_{cluster}$ the volume of all clusters and $V_{CNT\ cluster}$ the total CNT volume within clusters. In the case where $\mu = \eta = 1$, the CNTs are evenly distributed throughout the material. The bulk and shear moduli inside the clusters (K_{in} and G_{in}) as well as the bulk and shear moduli outside the clusters (K_{out} and G_{out}) can be obtained from the equations below:

$$K_{in} = K_M + \frac{V_{CNT}\eta(\delta_r - 3K_M\alpha_r)}{3(\mu - V_{CNT}\eta + V_{CNT}\eta\alpha_r)} \quad (4.32)$$

$$K_{out} = K_M + \frac{V_{CNT}(1 - \eta)(\delta_r - 3K_M\alpha_r)}{3[1 - \mu - V_{CNT}(1 - \eta) + V_{CNT}(1 - \eta)\alpha_r]} \quad (4.33)$$

$$G_{in} = G_M + \frac{V_{CNT}\eta(\eta_r - 2G_M\beta_r)}{2(\mu - V_{CNT}\eta + V_{CNT}\eta\beta_r)} \quad (4.34)$$

$$G_{out} = G_M + \frac{V_{CNT}(1 - \eta)(\eta_r - 2G_M\beta_r)}{2[1 - \mu - V_{CNT}(1 - \eta) + V_{CNT}(1 - \eta)\beta_r]} \quad (4.35)$$

where M and CNT stand for of matrix and CNTs respectively. Using the above set of equations, the MCNT bulk and shear moduli can be found to be:

$$K_{MCNT} = K_{out} \left[1 + \frac{\mu \left(\frac{K_{in}}{K_{out}} - 1 \right)}{1 + \alpha(1 - \mu) \left(\frac{K_{in}}{K_{out}} - 1 \right)} \right] \quad (4.36)$$

$$G_{MCNT} = G_{out} \left[1 + \frac{\mu \left(\frac{G_{in}}{G_{out}} - 1 \right)}{1 + \beta(1 - \mu) \left(\frac{G_{in}}{G_{out}} - 1 \right)} \right] \quad (4.37)$$

Where α and β , are defined by Shi et al. (2004) as:

$$\alpha = \frac{1 + \nu_{out}}{3(1 - \nu_{out})} \quad (4.38)$$

and,

$$\beta = \frac{2(4 - 5\nu_{out})}{15(1 - \nu_{out})} \quad (4.39)$$

where,

$$\nu_{out} = \frac{3K_{out} - 2G_{out}}{2(3K_{out} + G_{out})} \quad (4.40)$$

Once the K_{MCNT} and G_{MCNT} have been calculated the Poisson's ratio as well as the Young's modulus of the hybrid matrix can be obtained using:

$$\nu_{MCNT} = \frac{3K_{MCNT} - 2G_{MCNT}}{6K_{MCNT} + 2G_{MCNT}} \quad (4.41)$$

and,

$$E_{MCNT} = \frac{9K_{MCNT}G_{MCNT}}{3K_{MCNT} + G_{MCNT}} \quad (4.42)$$

4.3.2. Results

A MATLAB R2014b script file (Appendix A.1.4.) was developed to analyse the impact of nanotube agglomeration on the flexural behaviour of three-phase nanocomposites reinforced with either carbon or glass fibres in an epoxy matrix. Figure 4-12 depicts the longitudinal Young's modulus for increasing nanotube volume fraction and for varying fibre volume fraction. Also, nanotube reinforcement up to $V_{CNT} = 0.2$ has little effect on the longitudinal modulus. Whereas both the type and amount of fibre reinforcement had a more considerable impact. It should also be noted that the nanotube reinforcement, although slight, had a greater impact on the glass fibre reinforced composites as opposed to the carbon fibre reinforced composites. Figure 4-13 depicts the transverse modulus for increasing nanotube volume fraction. Here the nanotube reinforcement has a more considerable impact on the modulus especially on the glass fibre reinforced composite. The increase in both the nanotube volume fraction and fibre volume fraction had little to no impact on the carbon fibre reinforced composites.

Figure 4-14 shows the shear modulus for increasing CNT volume fraction. Here, the fibre type does not play a significant role but more so the nanotube volume fraction. Figure 4-15 depicts the Poisson's ratio for increasing nanotube volume fraction. Here the Poisson's ratio is seen to

decrease significantly until $V_{CNT} = 0.04$ after which the increase in nanotube volume fraction has little to no effect.

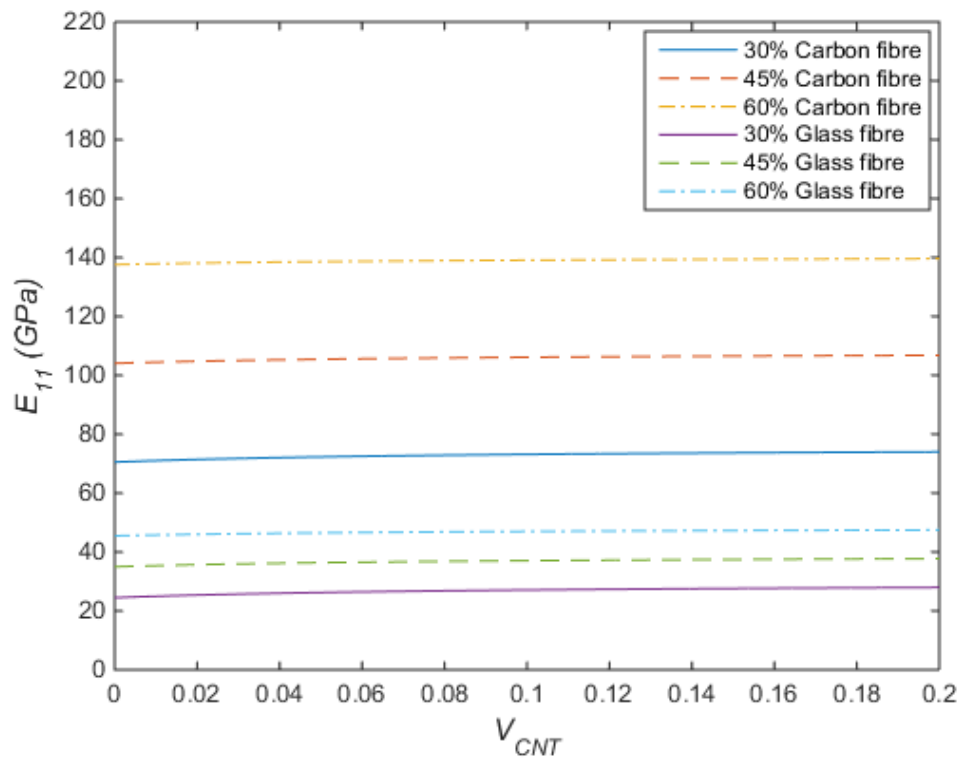


Figure 4-12: Effect of nanotube agglomeration on three-phase longitudinal modulus

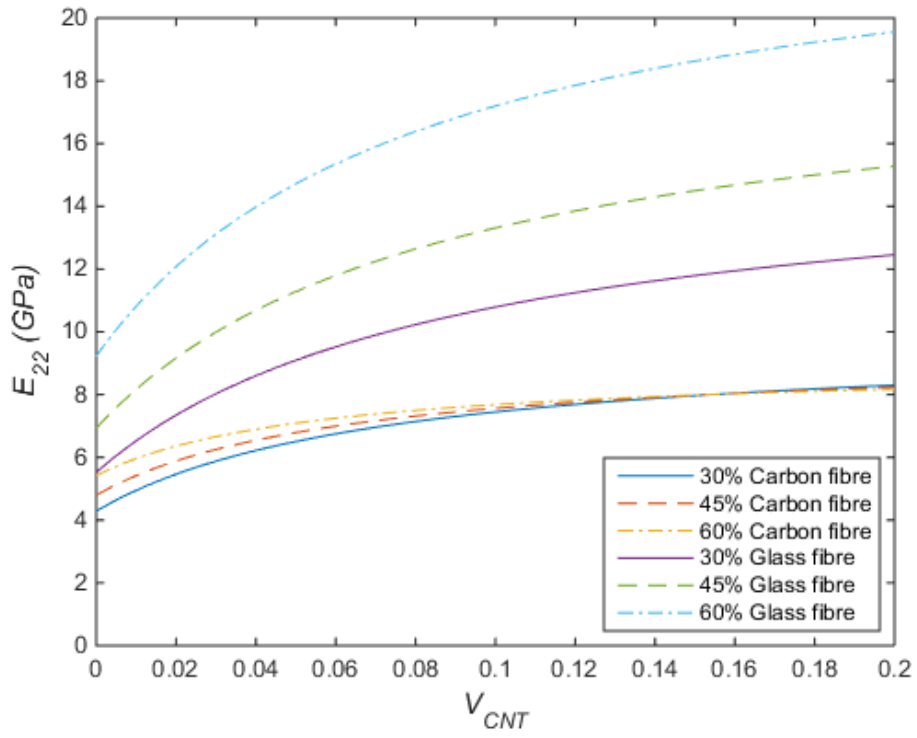


Figure 4-13: Effect of nanotube agglomeration on three-phase transverse modulus

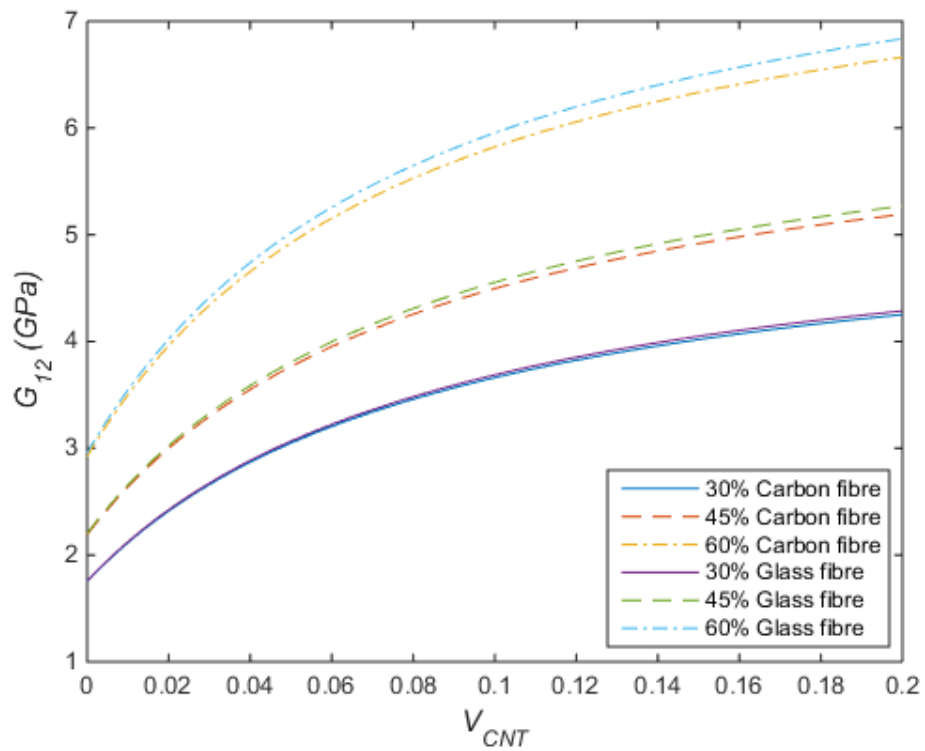


Figure 4-14: Effect of nanotube agglomeration on three-phase shear modulus

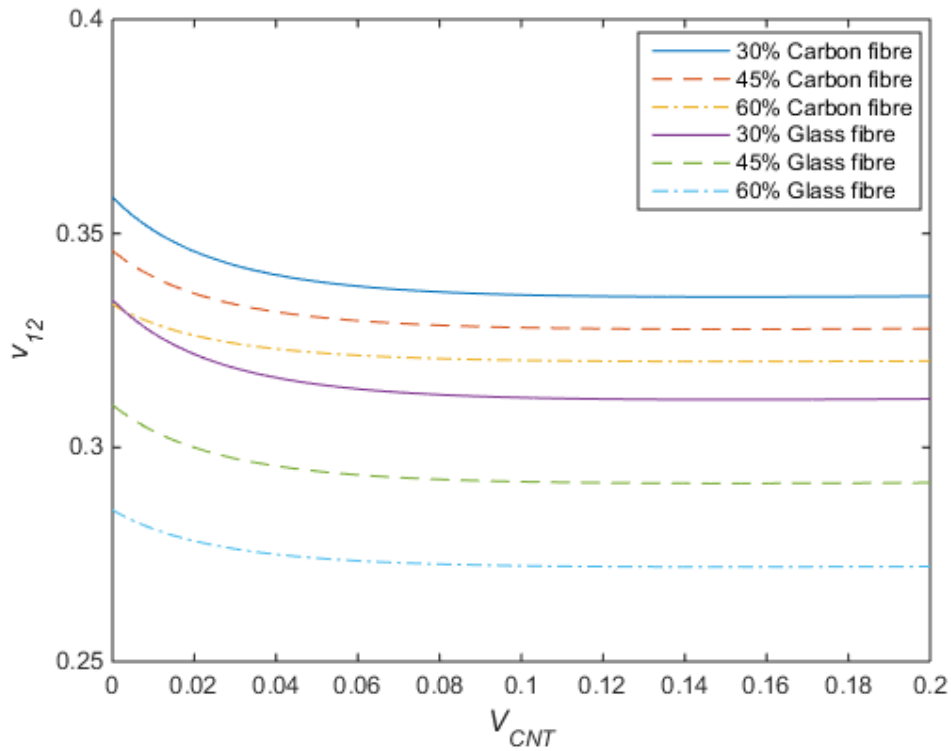


Figure 4-15: Effect of nanotube agglomeration on three-phase Poisson's ratio

4.4. Chapter summary

The objective of the chapter was to create computational models to analyse the effects of CNT orientation and agglomeration on the flexural properties of CNT-reinforced epoxy nanocomposites. Three scenarios were analysed. Firstly, the engineering constants for three-phase nanocomposites with straight, aligned nanotubes were analysed for glass and carbon fibre reinforced composites. Secondly, the same scenario was extended to straight, randomly orientated CNTs, and lastly the effects of nanotube agglomeration on three-phase composites were analysed.

An excellent agreement can be found between the present results and those provided in literature as seen in Figure 4-16, Figure 4-17 and Figure 4-18 for 45% reinforced carbon fibre nanocomposites. Experimental data for hybrid composites has been studied extensively by academics such as Gholami et al. (2018). Banerjee et al. (2014) found that the RoHM can be used to predict the longitudinal and transverse moduli of hybrid composites. This is consistent with the results presented in this dissertation. However, the RoHM can only predict the longitudinal Young's modulus with reasonable accuracy for low mass fraction of CNTs as seen in Figure 4-16. Taking into account the effect of nanotube agglomeration (Figure 4-18), a

stronger resemblance between the experimental data from literature and the results obtained in this dissertation can be observed.

Also, for increasing nanotube volume fraction, a more pronounced impact on the flexural response of glass fibre reinforced composites as opposed to the carbon fibre reinforced composites can be observed. This is due to the outstanding material properties of carbon fibre thus resulting in the nanotubes having less of an influence. Furthermore, the results obtained from the three-phase micromechanical analysis can be utilised to model nano-structures, which will be undertaken in the next chapter.

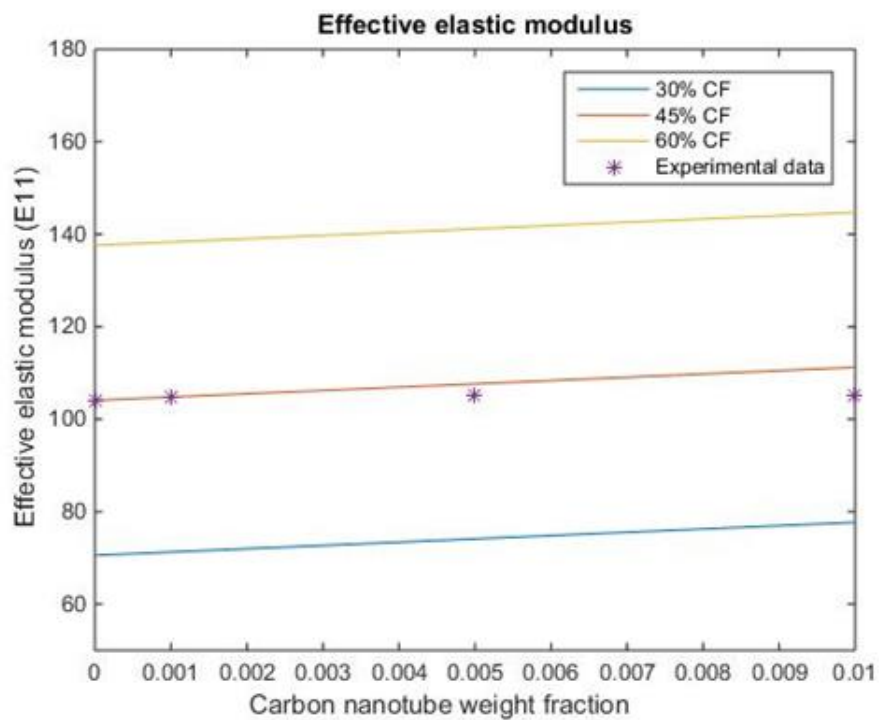


Figure 4-16: Conventional micromechanical approach vs experimental data

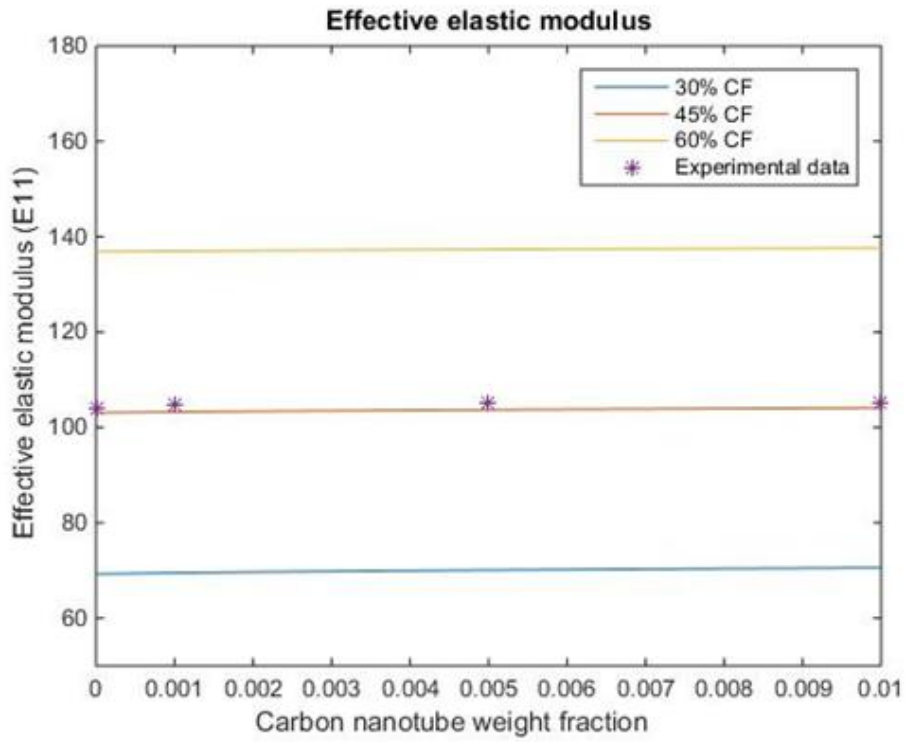


Figure 4-17: Modified micromechanical approach vs experimental data

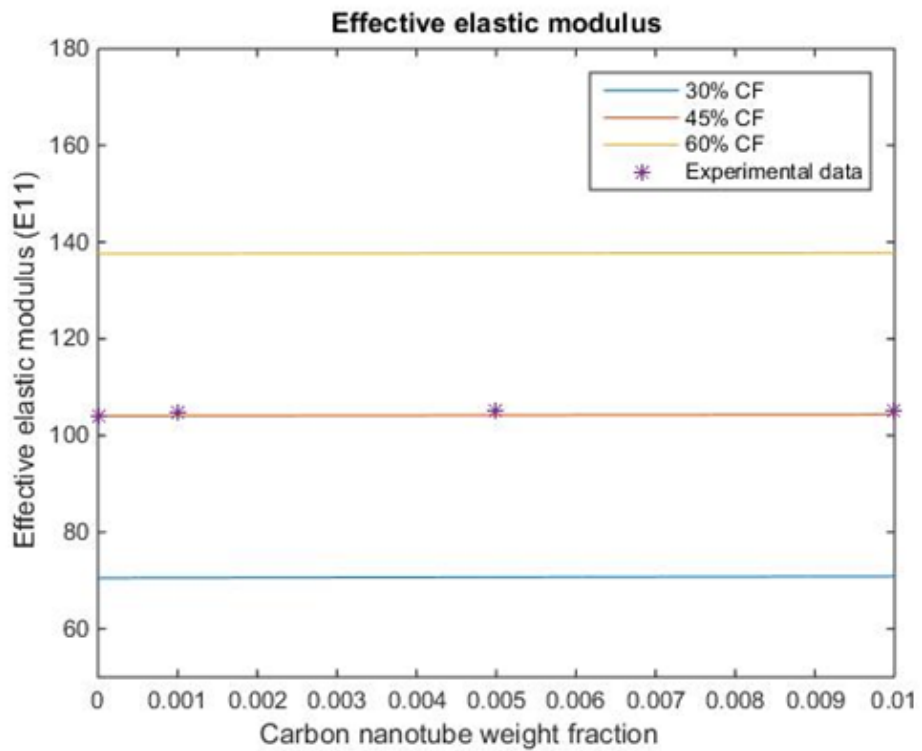


Figure 4-18: Effect of nanotube agglomeration vs experimental data

5. Three-phase composite structural application

Recently there has been extensive research performed on the bending, buckling and vibration of structural components made of CNT or graphene nanoplatelet reinforced nanocomposites. Studies of these materials are important for the design and manufacture of a large number of devices and systems used in engineering. Examples of such studies for both two-phase and three-phase nanocomposites include investigations by Masoud et al. (2018), Ahmadi et al. (2017) and He et al. (2015) who performed free and forced vibration analyses on multiscale composite plates and beams. Thostenson et al. (2002), Bekyarova et al. (2007) as well as Green et al. (2009) focused on the bending and buckling characteristics of carbon nanotube-based nanocomposites. Emphasis was also placed on the mechanical and thermomechanical properties of the composite. Other studies performed by Gholami et al. (2017) and Gholami et al. (2018) investigated the vibration and deflection properties of functionally-graded graphene nanoplatelet reinforced composite plates where promising results were attained.

Rafiee et al. (2014) and Kamarian et al. (2018) found that nanotube agglomeration affected the mechanical properties of nanocomposites by reducing the elastic moduli. This is due to several factors such as large aspect ratios, low bending rigidity and the debonding effect.

The much sought-after strength-to-weight ratio of hybrid composites make them very suitable for structural applications. In addition, they exhibit other superior properties such as low heat conductivity, increased corrosion resistance and low thermal expansion as well as increased fatigue life (Collins et al. 2000). The most commonly utilised composites are those with continuous fibres as well as those with short fibres embedded in a matrix material. Reducing structural weight, whilst maintaining critical material properties such as strength and stiffness, is one of the key design criteria for many such studies.

The purpose of the chapter is to analyse hybrid composite structures, and more specifically three-phase composite plates, to determine their effectiveness and performance in composite applications thus allowing for a comparison with traditional materials and composites.

Using the micromechanical results obtained in chapters 3 and 4, the performance of composite plates reinforced with both CNTs and fibre in an epoxy matrix can be analysed. Both glass and carbon fibres will be considered. The scenario chosen under which to analyse the performance of the hybrid composite is a symmetrical plate element in bending. Analysis of plate elements is pertinent for the mechanical characterisation by flexural response and because plates are considered fundamental structural elements. The plate is simply supported with an evenly

distributed load across the surface of the plate in the transverse direction. The measure of structural performance is being taken as the deflection of the plate at its centre. The results are then evaluated for a variety of different possibilities; including variation in reinforcement volume fraction, types of reinforcement used and nanotube agglomeration effects just to name a few. The study undergone in this chapter will allow for further analyses to be extended to elements such as graphene platelets in future work.

5.1. Notation and sign convention

Let us consider a plate placed in the X-Y plane. Plate surface slopes, W_x and W_y , gives arrows that point in the positive X and negative Y directions according to right hand rule. In order to analyse the plate elements, both rotations and surface slopes are required. Sign convention and subscripts are replaced as follows; θ_y with $-\psi_x$ and θ_x with ψ_y as seen in Figure 5-1.

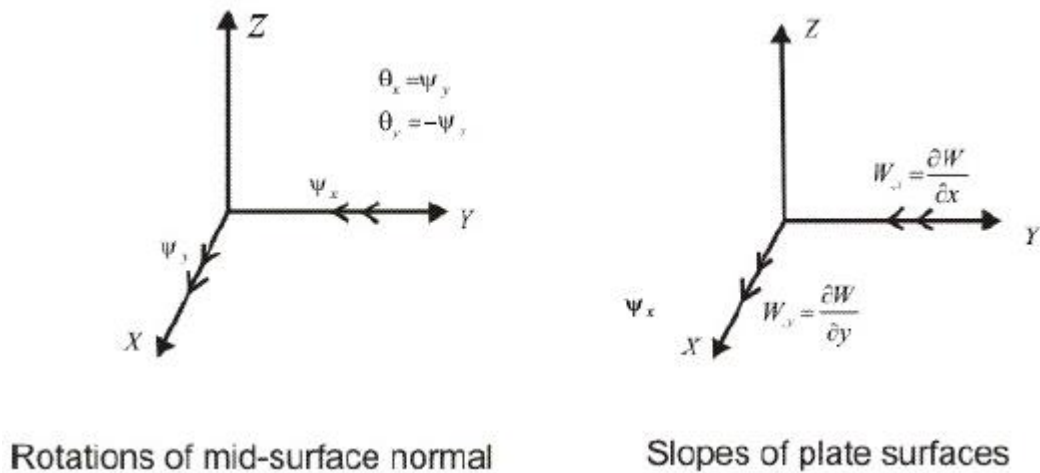


Figure 5-1: Plate sign convention (Birman 2011)

5.2. Plate theory

Plates are planar structures with a small thickness when compared to its planar dimensions. Since the applied forces on the plate is normal to the plane of the plate, the plate twists and bends in two directions in order to account for the load applied. To reduce the computational cost of the analysis, the variance in length scale is used to simplify the full 3D system to a 2D one, thus allowing for a more simplified micromechanical technique to be implemented. The aim is to determine the deformation experienced by the plate subjected to a uniform loading condition. The results obtained will allow for an improved understanding of both two-phase and three-phase composite mechanics by applying it to a structural element such as a plate.

Plate analyses are typically categorised into 2 types, dependant on the breadth to thickness ratio of the plate, and can be categorised into either thick or thin plates. If the max deflection is smaller than 1/10 of the thickness and the breadth to thickness ratio of the plate is smaller than 1/10, then the plate is considered a thin plate (Katili 1993). Kirchhoff's plate theory is used to investigate such thin plates. Conversely, Mindlin plate theory is utilised to investigate thick plates where the impact of shear deformation is taken into consideration (Ahmadi et al. 2018).

For this analysis the plate is assumed to be thin and therefore Kirchhoff plate theory is made use of to analyse the plate. The underlying assumption for typical Kirchhoff plate theory is that a straight line perpendicular to the mid-plane of the plate before bending, remains perpendicular even after bending occurs (Ghavanloo et al. 2019). Transverse shear deformation is not taken into consideration in this model. In essence, three principals are made use of to reduce the 3D set of elasticity equations to 2D ones as seen in Figure 5-2 and listed below.

1. The line perpendicular to the neutral axis before deformation occurs remains straight after the deformation has occurred.
2. The normal stress in thickness direction is neglected. i.e., $\sigma_z = 0$. This assumption reduces the 3D set of elasticity equations to 2D ones.
3. The transverse shear strains are set to equal zero. Therefore, shear strains γ_{xz} and γ_{yz} also equal zero. Hence, when bending, the plate thickness doesn't vary (Ghavanloo et al. 2019).

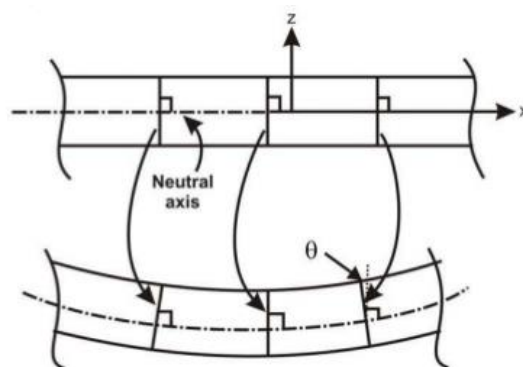


Figure 5-2: Kirchhoff plate bending (Saetta 1990)

Consider a plate with thickness t and with the plate mid-surface, $t/2$ from each surface. As such the X-Y plane is located in the plate's mid-surface (Figure 5-3), hence $z = 0$ represents the plate's mid-surface. Furthermore, let u , v and w be the displacements at any point in the x , y and z directions respectively.

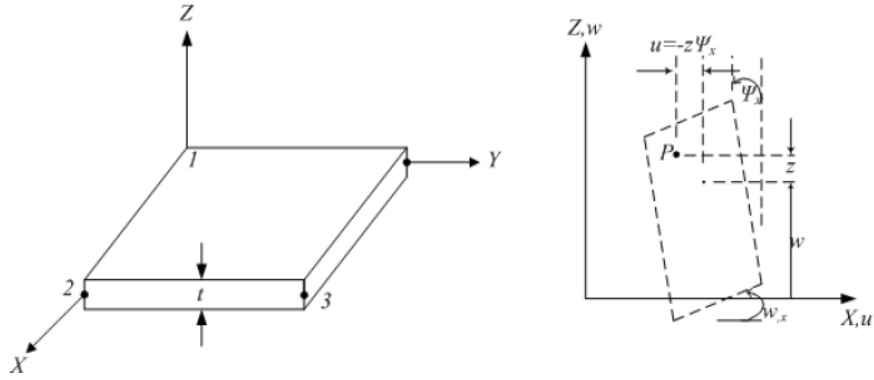


Figure 5-3: Plate notation (Saetta 1990)

Then the variance of u and v across the thickness of the plate can be visualised in terms of w through the following equations:

$$u = -z \frac{\partial w}{\partial x} \quad (5.1)$$

and,

$$v = -z \frac{\partial w}{\partial y} \quad (5.2)$$

where w is the plate's mid-plane deflection in the z -direction. Furthermore, the relationship between the deflection and strain can be expressed as:

$$\varepsilon_x = \frac{\partial u}{\partial x} = -z \frac{\partial^2 w}{\partial x^2} = z \chi_x \quad (5.3)$$

$$\varepsilon_y = \frac{\partial v}{\partial y} = -z \frac{\partial^2 w}{\partial y^2} = z \chi_y \quad (5.4)$$

$$\gamma_{xy} = \frac{\partial u}{\partial y} + \frac{\partial v}{\partial x} = -2z \frac{\partial^2 w}{\partial x \partial y} = z \chi_{xy} \quad (5.5)$$

where ε represents direct strain, γ refers to the shear strain and χ refers to the curvature along the respective directions. The above equations can be written in matrix form:

$$\begin{Bmatrix} \varepsilon_x \\ \varepsilon_y \\ \gamma_{xy} \end{Bmatrix} = -z \frac{\partial^2}{\begin{bmatrix} \partial x^2 \\ \partial y^2 \\ \partial x \partial y \end{bmatrix}} w \quad (5.6)$$

or simply as:

$$\varepsilon = -z\Delta w \quad (5.7)$$

where, ε is the in-plane strain vector, and Δ represents the differential operator matrix. Furthermore, the following equations can be determined from Hooke's law as follows:

$$\sigma = [D]\varepsilon \quad (5.8)$$

where:

$$[D] = \frac{E}{(1-\nu^2)} \begin{bmatrix} 1 & \nu & 0 \\ \nu & 1 & 0 \\ 0 & 0 & \frac{1-\nu}{2} \end{bmatrix} \quad (5.9)$$

In this equation, $[D]$ is equated to the value depicted for two-dimensional elements (i.e. $\sigma_z = 0$).

5.3. Calculation of shear forces and moments

Let's take a plate of thickness t and with dimensions dx by dy which is exposed to a load distributed evenly over the surface of the plate. For thin plates, the force of the plate can be equated to a load and as a result the analysis of separate body forces is not required (Ghavanloo et al. 2019). By combining Eq. (5.7) with Eq. (5.8) the following relationship can be derived:

$$\sigma = -z[D]\Delta w \quad (5.10)$$

From this equation we see that the transverse stress is varied linearly along the plate thickness as seen in Figure 5-4 and Figure 5-5; therefore the moments on the cross section can be calculated by means of integration as:

$$M = \begin{Bmatrix} M_x \\ M_y \\ M_{xy} \end{Bmatrix} = \int_{-t/2}^{t/2} \sigma z dt = - \left(\int_{-t/2}^{t/2} z^2 dt \right) [D]\Delta w = -\frac{t^3}{12} [D]\Delta w \quad (5.11)$$

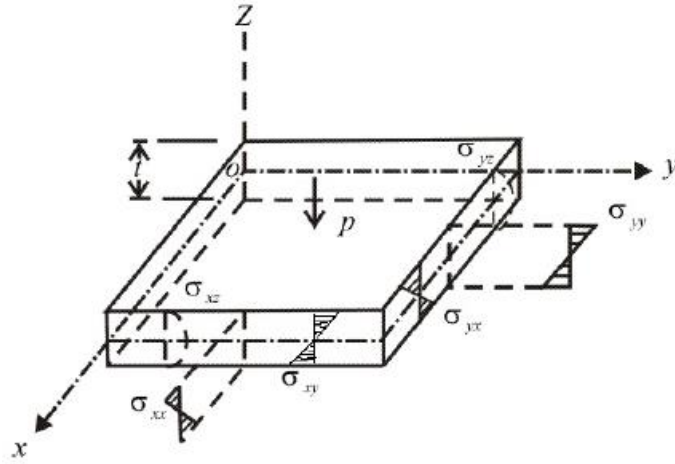


Figure 5-4: Stresses within a plate (Vidya-mitra 2018)

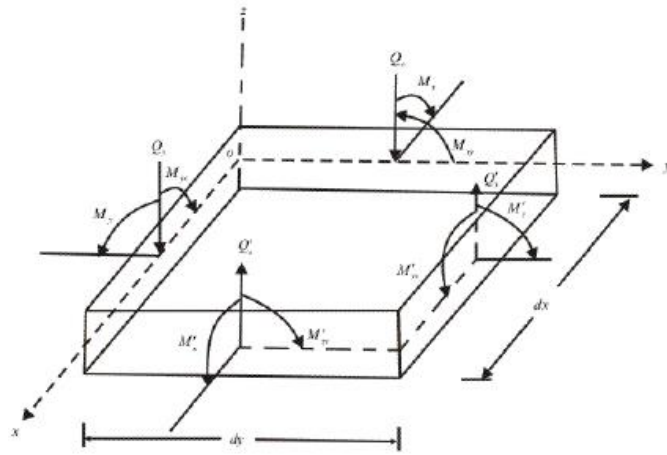


Figure 5-5: Forces and moments within a plate (Vidya-mitra 2018)

By expanding Eq. (5.11) the following three expressions can be obtained:

$$M_x = -\frac{Et^3}{12(1-\nu^2)} \left(\frac{\partial^2 w}{\partial x^2} + \nu \frac{\partial^2 w}{\partial y^2} \right) = D_p (\chi_x + \nu \chi_y) \quad (5.12)$$

$$M_y = -\frac{Et^3}{12(1-\nu^2)} \left(\frac{\partial^2 w}{\partial y^2} + \nu \frac{\partial^2 w}{\partial x^2} \right) = D_p (\chi_y + \nu \chi_x) \quad (5.13)$$

$$M_{xy} = M_{yx} = \frac{Et^3}{12(1-\nu^2)} \left(\frac{\partial^2 w}{\partial x \partial y} \right) = -\frac{D_p(1-\nu)}{2} \chi_{xy} \quad (5.14)$$

Where, D_p represents the flexural rigidity of the plate and can be shown as:

$$D_p = \frac{Et^3}{12(1 - \nu^2)} \quad (5.15)$$

Now taking into consideration the moments, varying along the plate's breadth and length, and representing it as a function of both x and y respectively. Then, if M_x acts on one side then, $M_x = M_x + \partial M_x / \partial x dx$ acts on the opposing side of the plate. If the plate is in a state of equilibrium, then the equations of forces can be expressed as:

$$\frac{\partial Q_x}{\partial x} + \frac{\partial Q_y}{\partial y} + P = 0 \quad (5.16)$$

$$\frac{\partial M_x}{\partial x} + \frac{\partial M_{xy}}{\partial y} = Q_x \quad (5.17)$$

$$\frac{\partial M_{xy}}{\partial x} + \frac{\partial M_y}{\partial y} = Q_y \quad (5.18)$$

Furthermore, the following relations can be derived from the above equations as:

$$Q_x = -D_p \frac{\partial}{\partial x} \left(\frac{\partial^2 w}{\partial x^2} + \frac{\partial^2 w}{\partial y^2} \right) \quad (5.19)$$

$$Q_y = -D_p \frac{\partial}{\partial y} \left(\frac{\partial^2 w}{\partial x^2} + \frac{\partial^2 w}{\partial y^2} \right) \quad (5.20)$$

And finally, the equilibrium equation for small displacement flat plates can be equated:

$$\frac{\partial^4 w}{\partial x^4} + 2 \frac{\partial^4 w}{\partial x^2 \partial y^2} + \frac{\partial^4 w}{\partial y^4} = -\frac{P}{D_p} \quad (5.21)$$

5.4. Boundary conditions

Different boundary conditions imposed on the plate, such as the manner in which the plate is supported result in a change of the governing differential equations. For this analysis a simply supported square plate is analysed as seen in Figure 5-6. The plate is symmetrical in both the x and y directions.

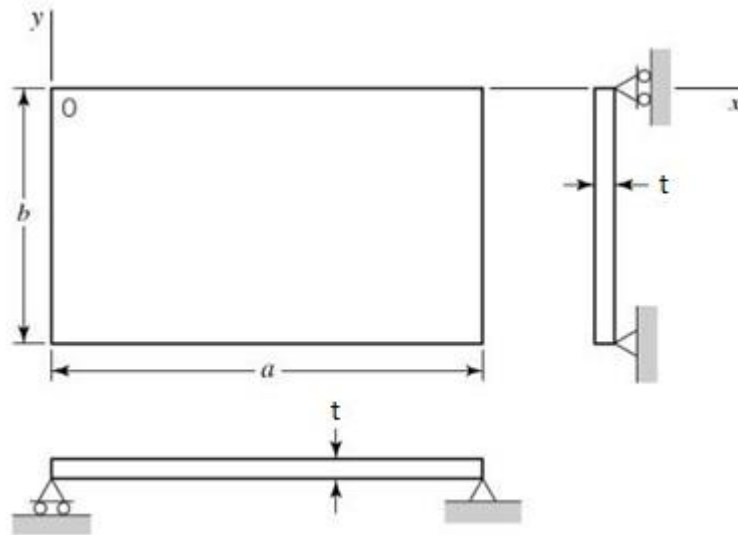


Figure 5-6: Plate dimensions and notation

Therefore, for a simply support edge (along both the x and y direction) the respective boundary conditions are depicted as:

- $w(x, y) = 0$;
- $M_x = 0$ for $[x = const \ \& \ 0 \leq y \leq b]$;
- $M_y = 0$ for $[y = const \ \& \ 0 \leq x \leq a]$;

Once the displacement of the plate at various points has been calculated, the moments, stresses as well as the strains in the plate can be calculated and therefore the flexural response can be analysed.

5.5. Plate analysis

Using MATLAB R2014b, a script was developed to analyse the plate element in bending. Considering a plate which is simply supported, with dimensions a and b in the x and y directions respectively (Saetta 1990). The differential equation governing the deflection of the symmetrically laminated cross-ply plate (Figure 5-6) under a distributed load $P(x,y)$, as determined by Eq. (5.21) can be given as:

$$D_{11}w_{xxxx} + 2(D_{12} + 2D_{66})w_{xxyy} + D_{22}w_{yyyy} = P(x, y) \quad (5.22)$$

where D_{ij} are the bending stiffnesses, $w(x, y)$ is the transverse deflection and the derivatives with respect to x and y are indicated by the respective subscripts. The boundary conditions, as stated prior, for a simply supported plate can be rewritten in script notation as:

$$-D_{11}w_{xx} - D_{12}w_{yy} = 0 \quad \text{at } x = 0, a \quad (5.23)$$

and,

$$-D_{12}w_{xx} - D_{22}w_{yy} = 0 \quad \text{at } y = 0, b \quad (5.24)$$

The load acting on the plate can be expanded in Fourier sine series as:

$$P(x, y) = \sum_{m=1}^{\infty} \sum_{n=1}^{\infty} P_{mn} \sin \alpha_m x \sin \beta_n y \quad (5.25)$$

Where $\alpha_m = m\pi/x$ and $\beta_n = n\pi/y$ with the coefficient P_{mn} given by:

$$P_{mn} = (4/ab) \int_0^b \int_0^a P(x, y) \sin \alpha_m x \sin \beta_n y \, dx dy \quad (5.26)$$

The solution for deflection can be expressed as:

$$w(x, y) = \sum_{m=1}^{\infty} \sum_{n=1}^{\infty} C_{mn} \sin \alpha_m x \sin \beta_n y \quad (5.27)$$

which satisfies the boundary conditions stated by Eq. (5.23) and Eq. (5.24). The coefficient C_{mn} is given as:

$$C_{mn} = \frac{a^4 P_{mn}}{\pi^4 D_{mn}} \quad (5.28)$$

where,

$$D_{mn} = D_{11}m^4 + 2(D_{12} + 2D_{66})(mnr)^2 + D_{22}(nr)^4 \quad (5.29)$$

with $r = a/b$ being the aspect ratio. The stresses σ_{xx}^k , σ_{yy}^k and τ_{xy}^k at the k-th layer are computed using the below three equations:

$$\sigma_{xx}^k = \frac{a^2}{\pi^2} z \sum_{m=1}^{\infty} \sum_{n=1}^{\infty} \frac{P_{mn}}{D_{mn}} (\bar{Q}_{11}^k m^2 + \bar{Q}_{12}^k n^2 r^2) \sin \alpha_m x \sin \beta_n y \quad (5.30)$$

$$\sigma_{yy}^k = \frac{a^2}{\pi^2} z \sum_{m=1}^{\infty} \sum_{n=1}^{\infty} \frac{P_{mn}}{D_{mn}} (\bar{Q}_{12}^k m^2 + \bar{Q}_{22}^k n^2 r^2) \sin \alpha_m x \sin \beta_n y \quad (5.31)$$

$$\tau_{xy}^k = -2 \frac{a^2}{\pi^2} r \bar{Q}_{66}^k z \sum_{m=1}^{\infty} \sum_{n=1}^{\infty} \frac{P_{mn}}{D_{mn}} mn \cos \alpha_m x \cos \beta_n y \quad (5.32)$$

where \bar{Q}_{11}^k , \bar{Q}_{12}^k and \bar{Q}_{22}^k are the reduced stiffnesses of the k-th layer. Using the above theory along with the appropriate micromechanical techniques, as studied in previous chapters, the flexural response of the plate element can be analysed for different conditions.

5.6. Results

A square plate, simply supported along its edges and with an evenly distributed load applied in the transverse direction is analysed (Figure 5-7). Commercially available software, MATLAB R2014b was chosen to perform the analysis (Appendix A.1.5. and A.1.6.). As seen in Figure 5-6 and Figure 5-7 the plate is placed in the X-Y plane where Θ_x and Θ_y represents the rotation along the x-axis and y-axis respectively. The plate is considered to have thickness t and the mid-plane of the plate is located at $t/2$ ($z = 0$, at the plate mid-surface). The length and width of the plate is set to $a=1\text{m}$ and $b=1\text{m}$.

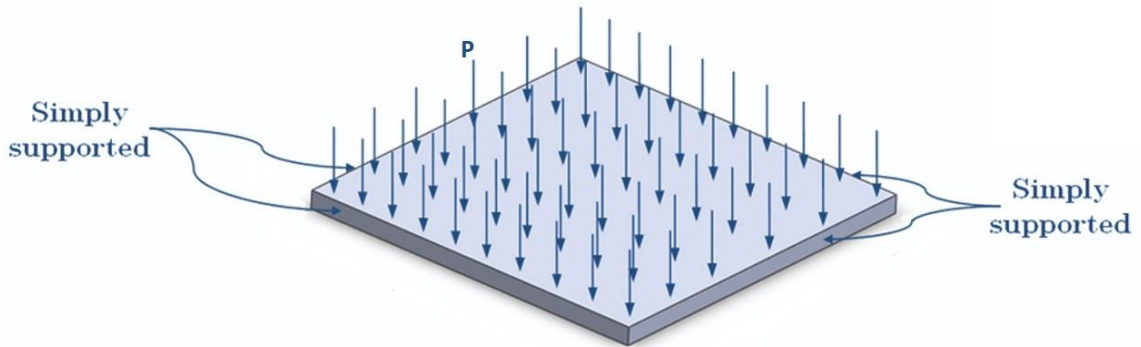


Figure 5-7: Plate with distributed load

The same properties as shown in Table 3-1 and Table 3-2 were used to model the two and three-phase composites. The deflection at the centre of the plate is analysed under a uniform transverse pressure. Table 5-1 summarises the plate properties used in the analyses unless otherwise stated. The engineering constants used are obtained from the micromechanical studies performed in the previous chapters.

Table 5-1 : Plate properties

Plate Property	Value
Plate thickness (t)	0.1m
Length of plate (a)	1m
Width of plate (b)	1m
Pressure (P)	1N
Number of layers	8
Layup	[90/0/90/0] _s
Fibre reinforcement	45%

Firstly, the effect of nanotube diameter is analysed for increasing CNT volume fraction. Here it's seen that as the nanotube diameter decreases so does the amount of deflection at the centre of the plate (W_c) as a function of a pure epoxy plate bending under similar conditions (W_0). The same outcome is present in both Figure 5-8 and Figure 5-9, representing carbon and glass fibre reinforced composites respectively. It should be noted that for both scenarios 45% fibre reinforcement is considered with an aspect ratio of 1. These diameters were chosen to allow for comparison with two-phase data from literature. The effect of nanotube agglomeration is neglected in these analyses. It should also be noted from the two figures that the carbon fibre reinforced composite experiences less deflection compared to the glass fibre alternative. This is due to the impressive properties of carbon fibres.

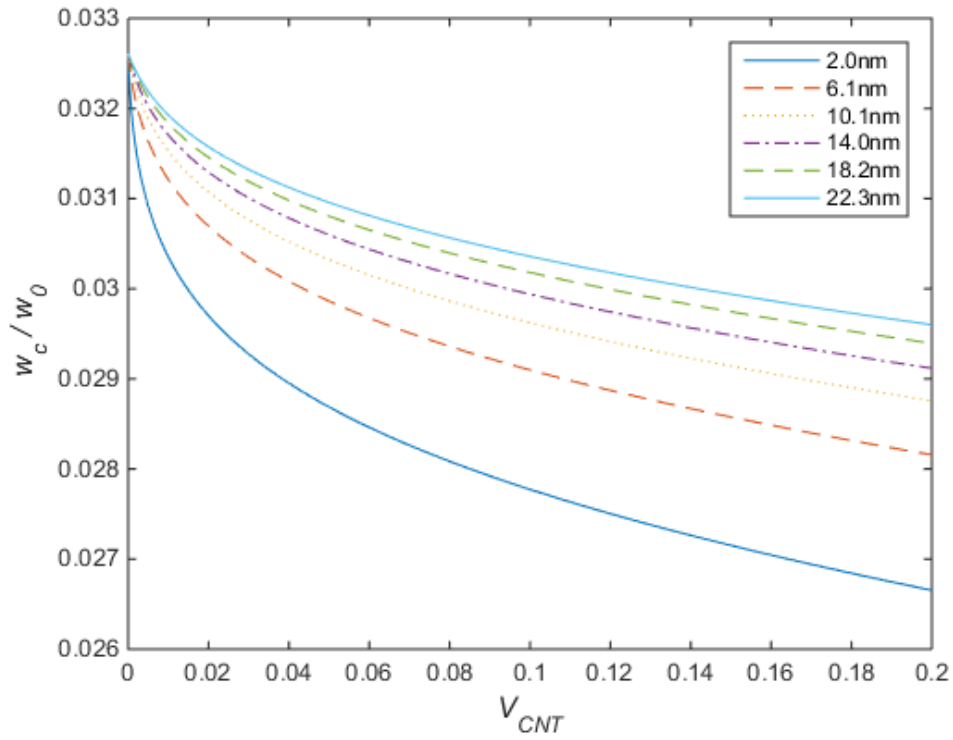


Figure 5-8: Effect of nanotube diameter on the deflection at the centre of the plate (W_c) as a function of a pure epoxy plate in bending (W_0) on carbon fibre reinforced nanocomposites for increasing nanotube volume fraction

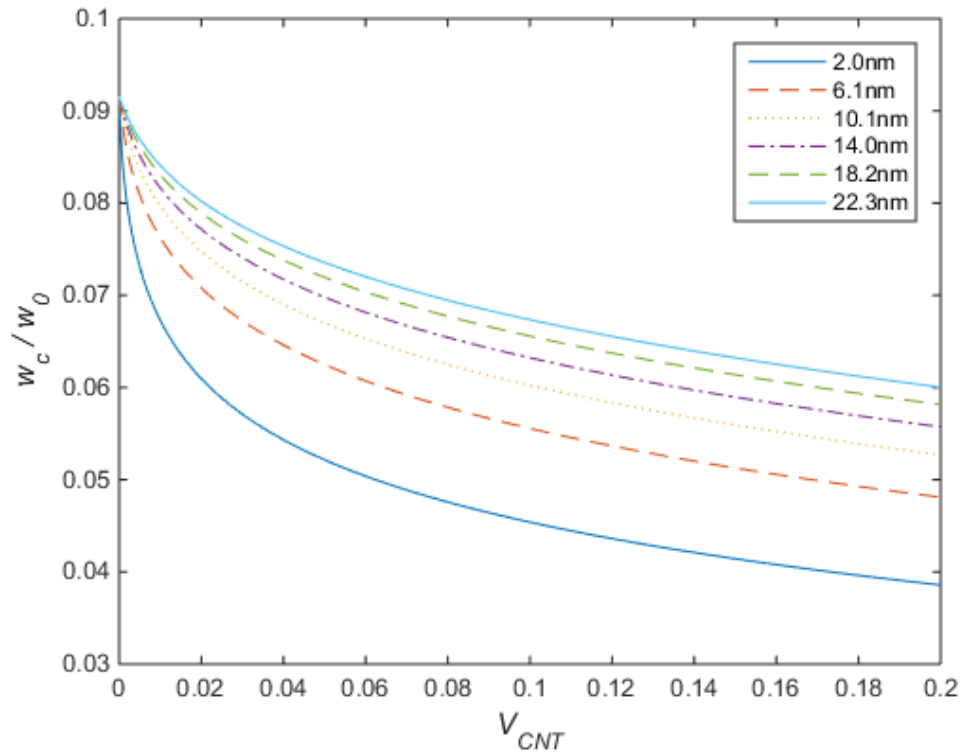


Figure 5-9: Effect of nanotube diameter on the deflection at the centre of the plate (W_c) as a function of a pure epoxy plate in bending (W_0) on glass fibre reinforced nanocomposites for increasing nanotube volume fraction

Figure 5-10 shows the impact of fibre volume fraction on the flexural behaviour of the three-phase composites. Here, the carbon fibre reinforced nanocomposite experienced less deflection. It can also be seen that for low volume fractions of nanotube reinforcement, the glass fibre reinforced composites experience a significant change in stiffness. The increase in fibre volume fraction (30% to 60%) evidently decreases the amount of deflection experienced. This is due to the increase in elastic moduli for increasing nanotube and fibre reinforcement as studied in previous chapters.

Figure 5-11 depicts a similar analysis as performed in Figure 5-10, however the effect of nanotube agglomeration is taken into consideration. Similar trends can be observed between the two figures, but it should be noted that for low nanotube volume fraction, initially the deflection decreases less rapidly and displays more linear material properties. It should be noted that this analysis was performed for $\mu=0.4$.

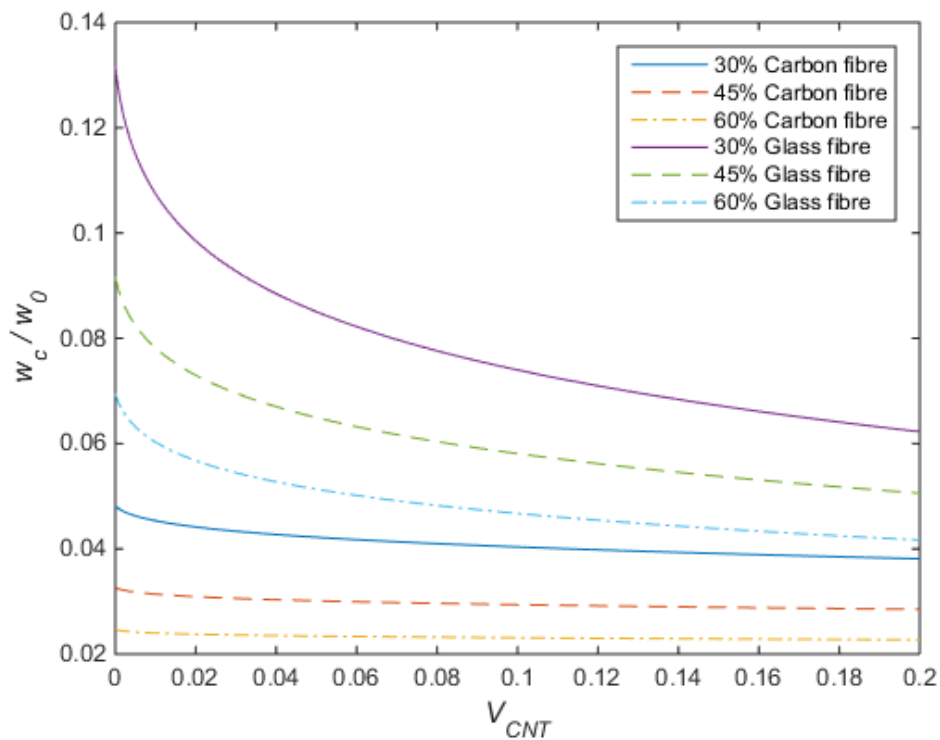


Figure 5-10: Deflection ratio plotted against CNT content for various fibre contents, randomly oriented CNTs

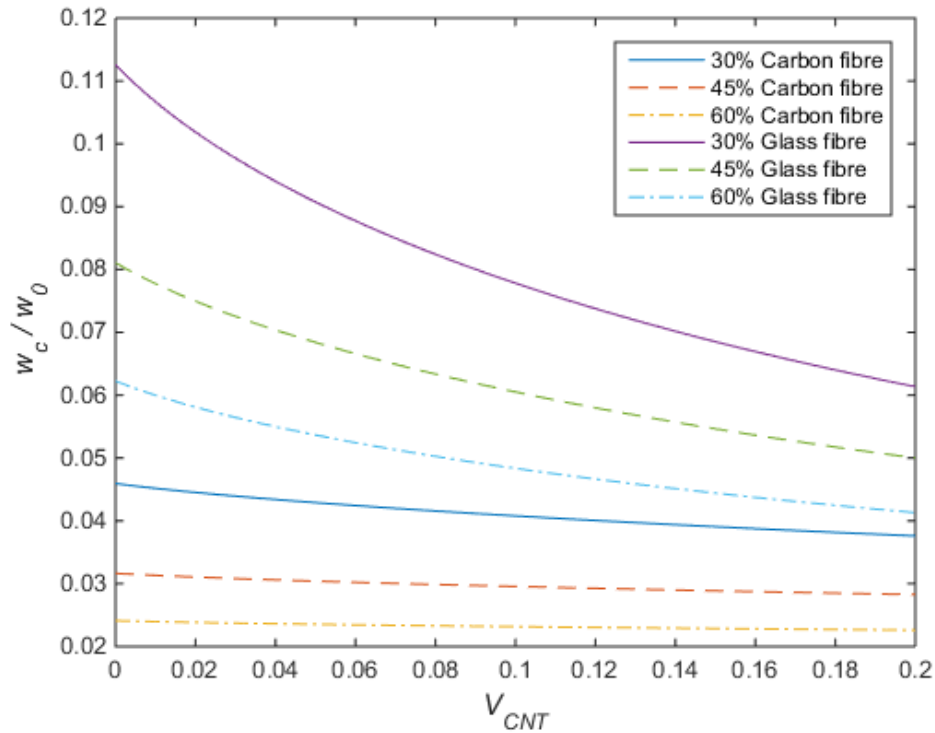


Figure 5-11: Deflection ratio plotted against CNT content for various fibre contents, agglomerated CNTs

The effect of nanotube agglomeration is studied more closely in Figure 5-12, Figure 5-13, Figure 5-14 and Figure 5-15. Firstly the effect of 40 and 60% nanotube agglomeration is studied for carbon fibre reinforced composites for increasing volume fractions (30%, 45% and 60% fibre reinforcement) in Figure 5-12, Figure 5-13 and Figure 5-14 respectively. Here a similar pattern is observed for all cases where at approximately 1.2% CNT volume fraction the deflection is the same irrespective of the amount of agglomeration present. However, it should be noted that for increasing fibre volume fractions the amount of deflection present decreases.

Figure 5-15 takes into consideration the same conditions mentioned above however glass fibre, instead of carbon fibre, reinforcement is used. Here the deflection for all three cases of 30%, 45% and 60% fibre reinforcement are significantly more than that of carbon fibre reinforced nanocomposites. Again, a similar trend is viewed where at approximately 1.2% CNT volume fraction the deflection is the same irrespective of the amount of the amount of agglomeration present.

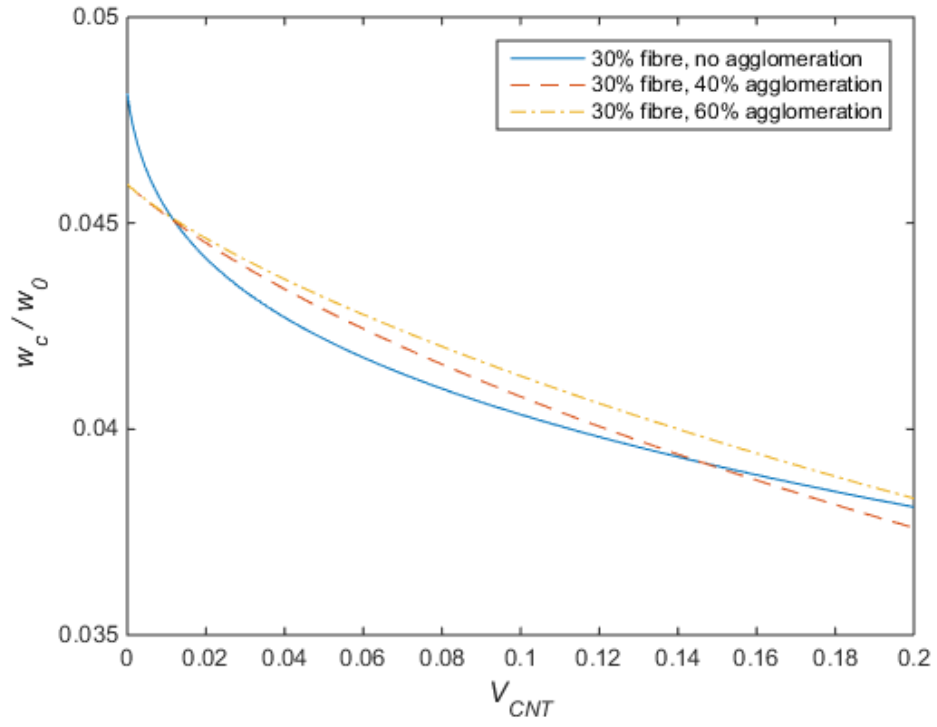


Figure 5-12: Deflection ratio plotted against CNT content with and without agglomeration and with 30% carbon fibre content

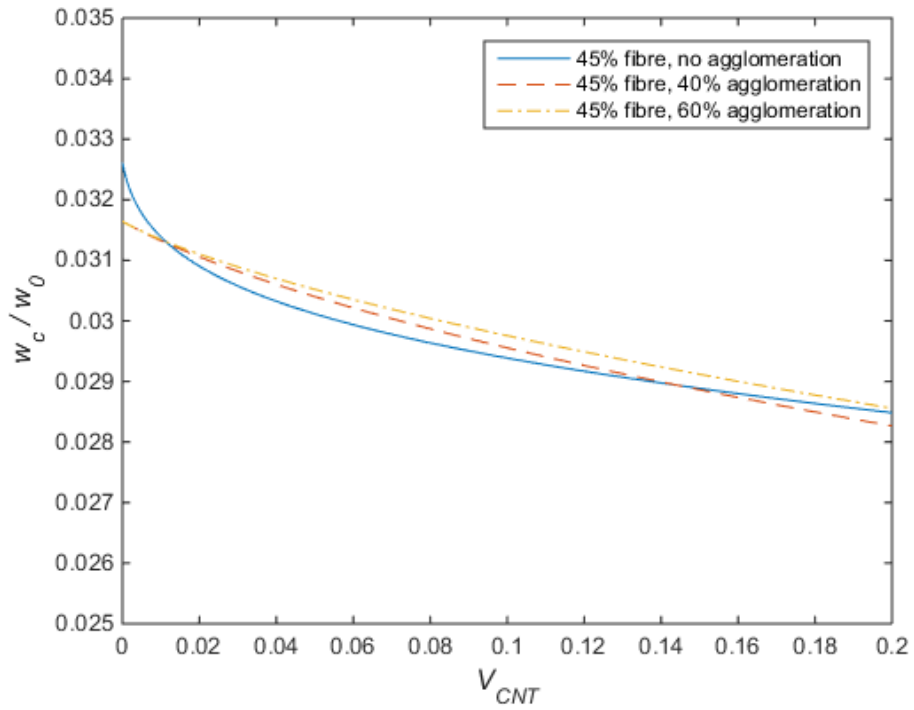


Figure 5-13: Deflection ratio plotted against CNT content with and without agglomeration and 45% carbon fibre content

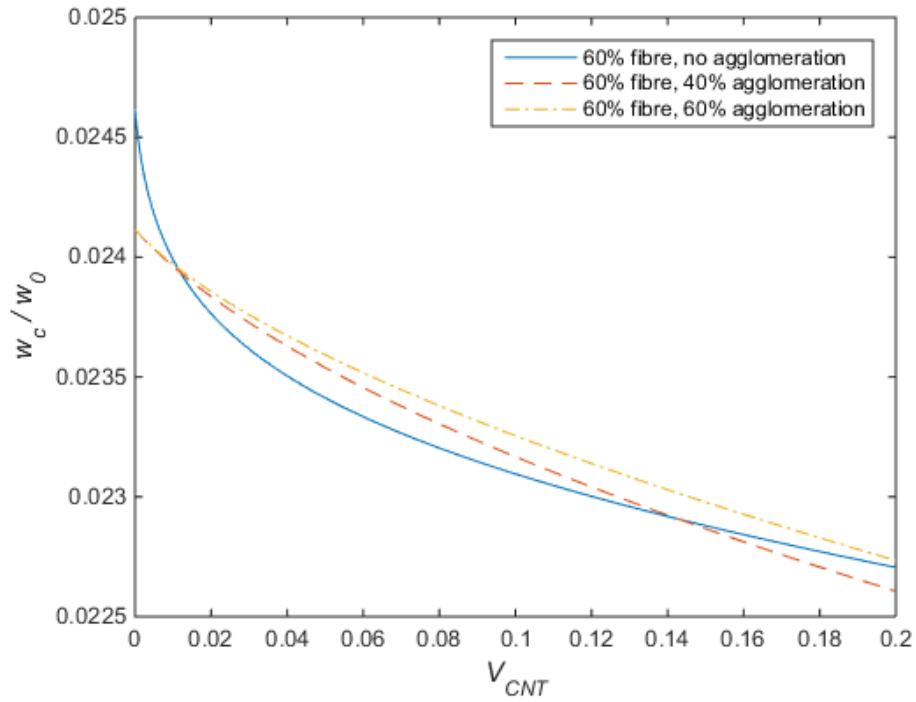


Figure 5-14: Deflection ratio plotted against CNT content with and without agglomeration and 60% carbon fibre content

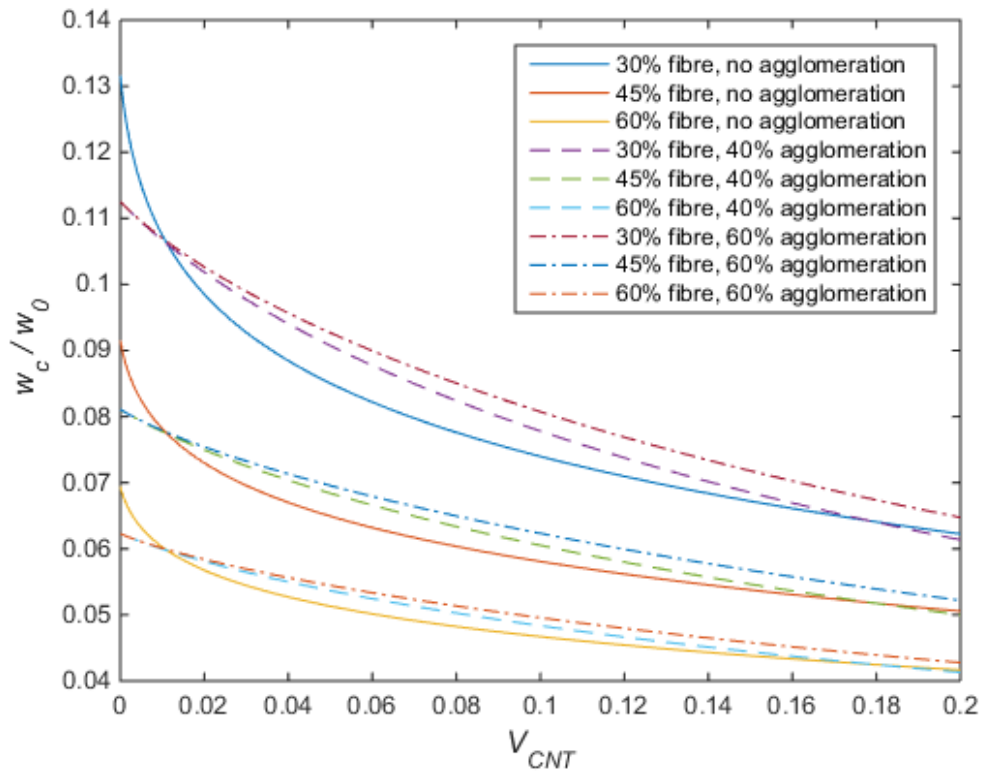


Figure 5-15: Effect of nanotube agglomeration on glass fibre reinforced nanocomposites

Next the impact of fibre orientation is analysed where both aligned, and randomly orientated scenarios are studied for carbon and glass fibre reinforcement respectively. Comparing Figure 5-16 to Figure 5-17 it's seen here that the glass fibre reinforced nanocomposite is subject to increased deflection but for aligned CNTs the impact of nanotube orientation reduces as the nanotube volume fraction increases. In both cases it can also be observed that aligned nanotubes result in less deflection, this significant difference however, could also possibly be due to the difference in micromechanical methods used. It should also be noted that 45% fibre reinforcement is used in these analyses.

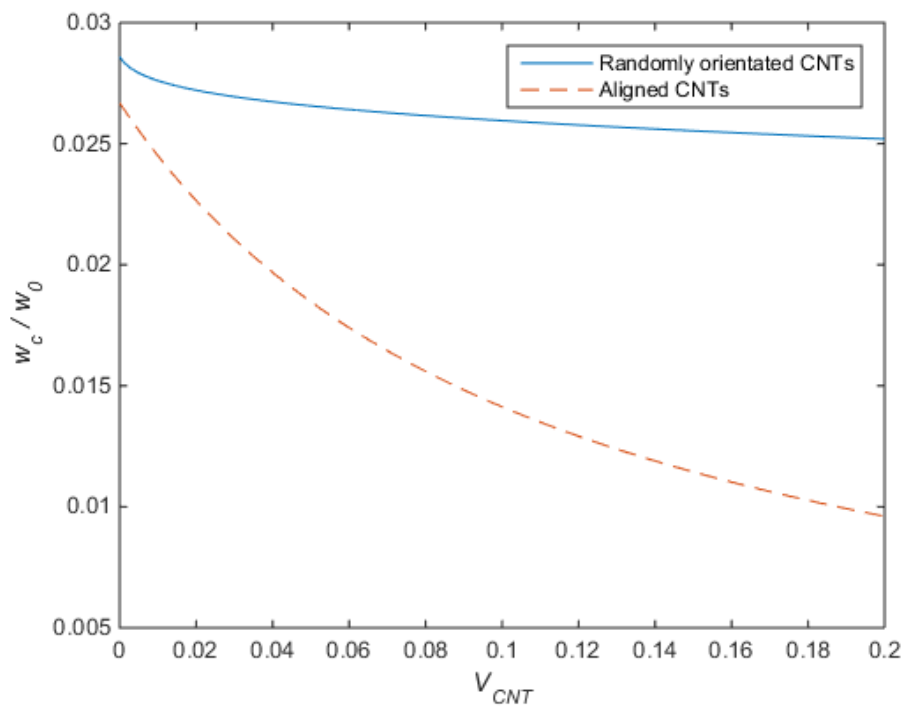


Figure 5-16: Carbon fibre reinforced nanocomposites

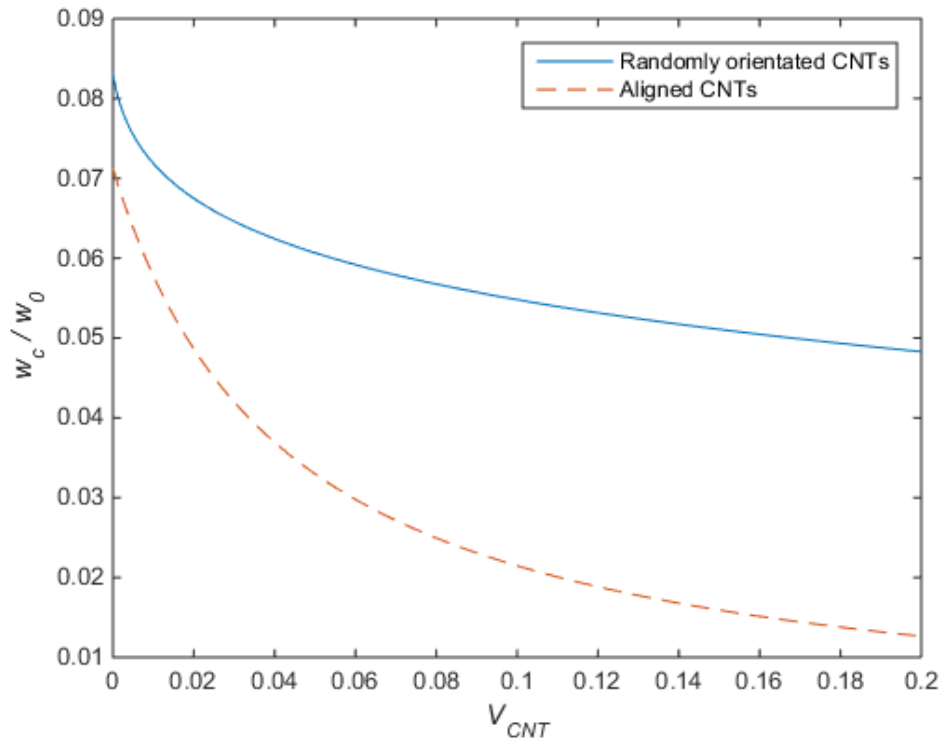


Figure 5-17: Glass fibre reinforced nanocomposites

Figure 5-18 analyses the effect of laminate layup for increasing nanotube volume fraction. Here for both the carbon and glass fibre scenarios, the implementation of the cross-ply laminate results in significantly less deflection. Again 45% fibre volume fraction is used.

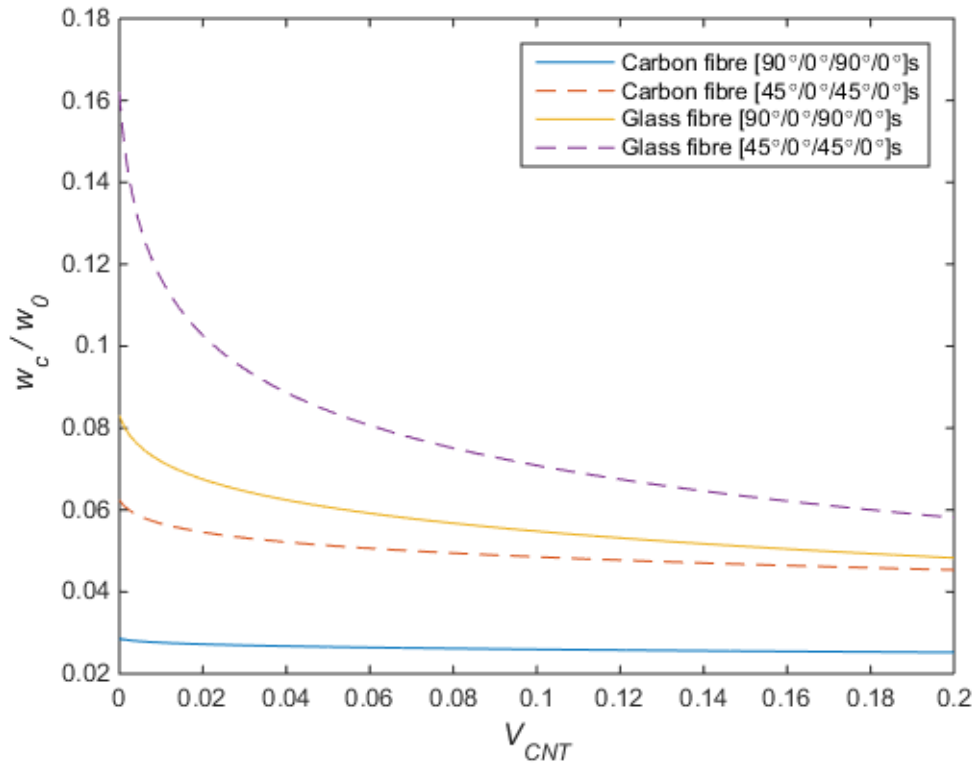


Figure 5-18: Fibre reinforced nanocomposite with various layups

Figure 5-19 and Figure 5-20 compare two-phase to three-phase nanocomposites for increasing nanotube volume fraction. Here 45% fibre reinforcement is used. In both figures, for low nanotube volume fractions, a significant decrease in deflection is experienced for two-phase nanocomposites. Figure 5-19 and Figure 5-20 depict at zero nanotube volume fraction, both instances have a w_c/w_0 equal to 0.67 for the two-phase nanocomposites compared to 0.09 and 0.03 for glass and carbon three-phase nanocomposites respectively. It should also be noted that for both two-phase and three-phase reinforced glass fibre composites the amount of deflection is equal at 13.06% nanotube volume fraction. At 45% reinforcement the addition of glass fibre yields no significant results for nanotube volume fractions greater than 13.06% and the two-phase nanocomposite yields better results at these volumes.

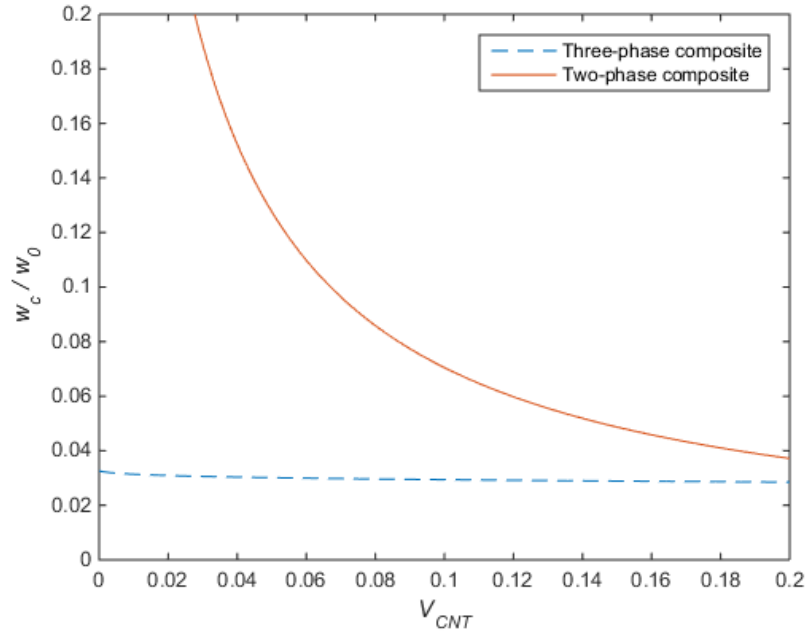


Figure 5-19: Carbon fibre reinforced three-phase vs two-phase nanocomposite

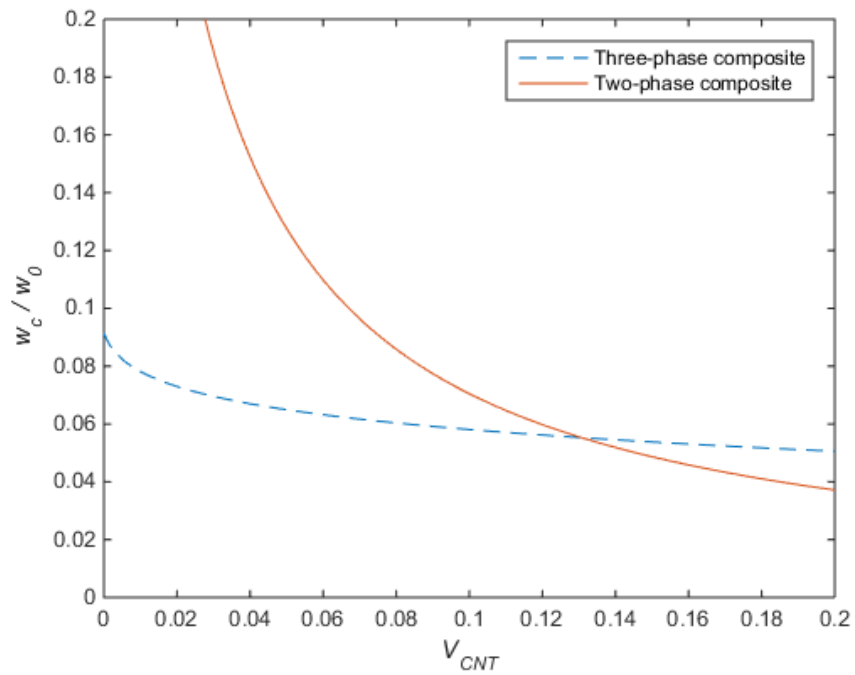


Figure 5-20: Glass fibre reinforced three-phase vs two-phase nanocomposite

Lastly, contour pots of w_c/w_o were generated for increasing nanotube (x-axis) and fibre volume fractions (y-axis) for both glass and carbon fibre reinforcement (Figure 5-21 and Figure 5-24). Furthermore, the effects of agglomeration were studied for similar conditions in Figure 5-23 and Figure 5-24.

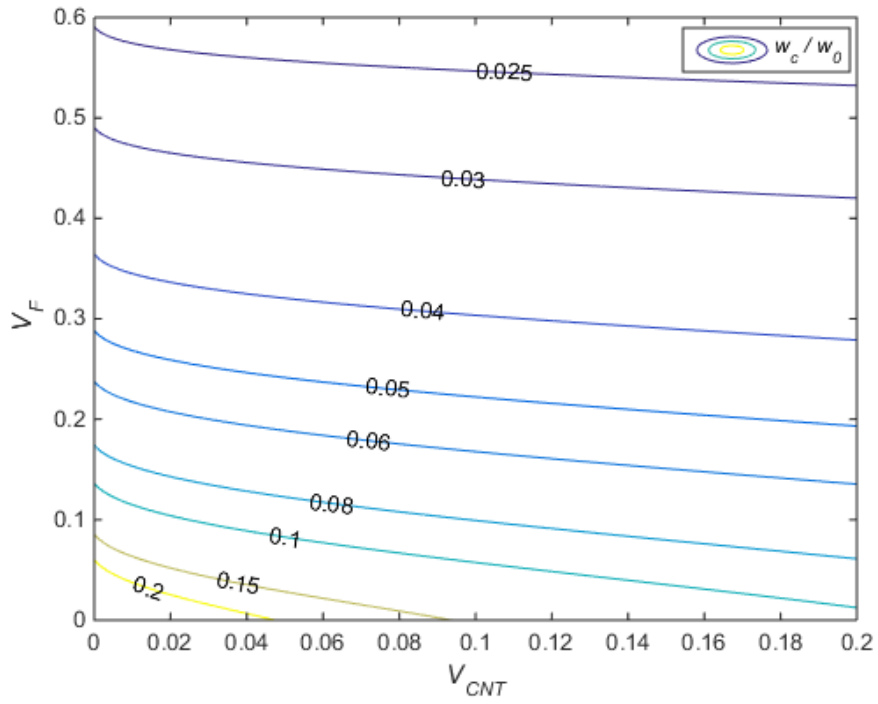


Figure 5-21: Carbon fibre reinforced deflection contour for increasing reinforcement volume fraction (randomly orientated CNT)

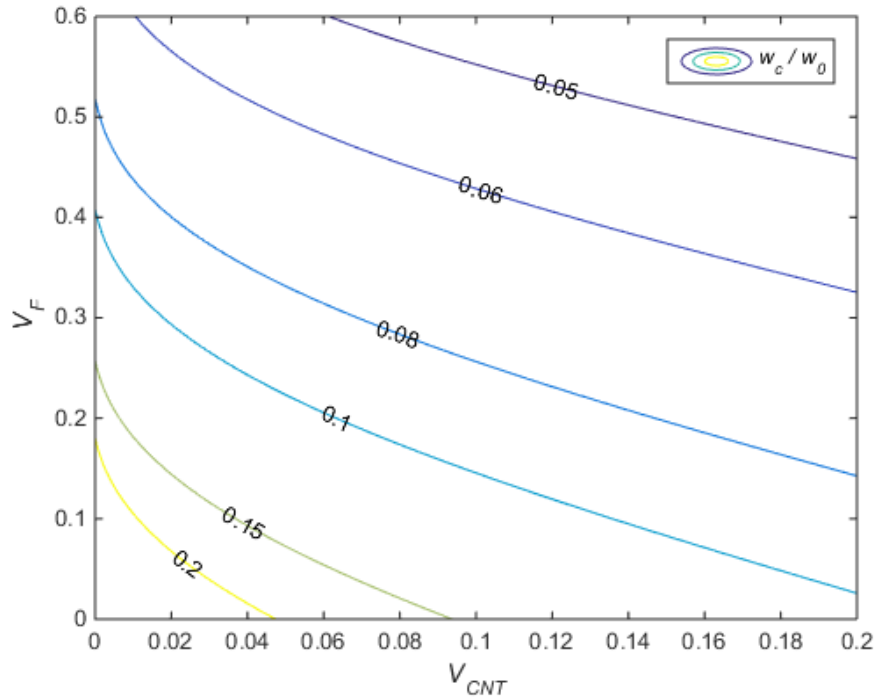


Figure 5-22: Glass fibre reinforced deflection contour for increasing reinforcement volume fraction (randomly orientated CNT)

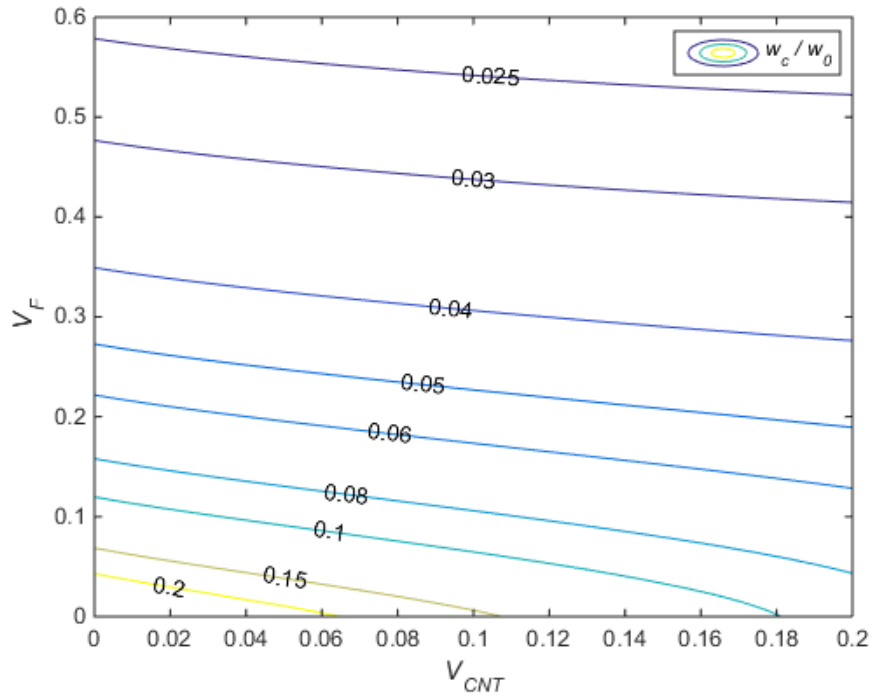


Figure 5-23: Carbon fibre reinforced deflection contour for increasing reinforcement volume fraction with agglomeration

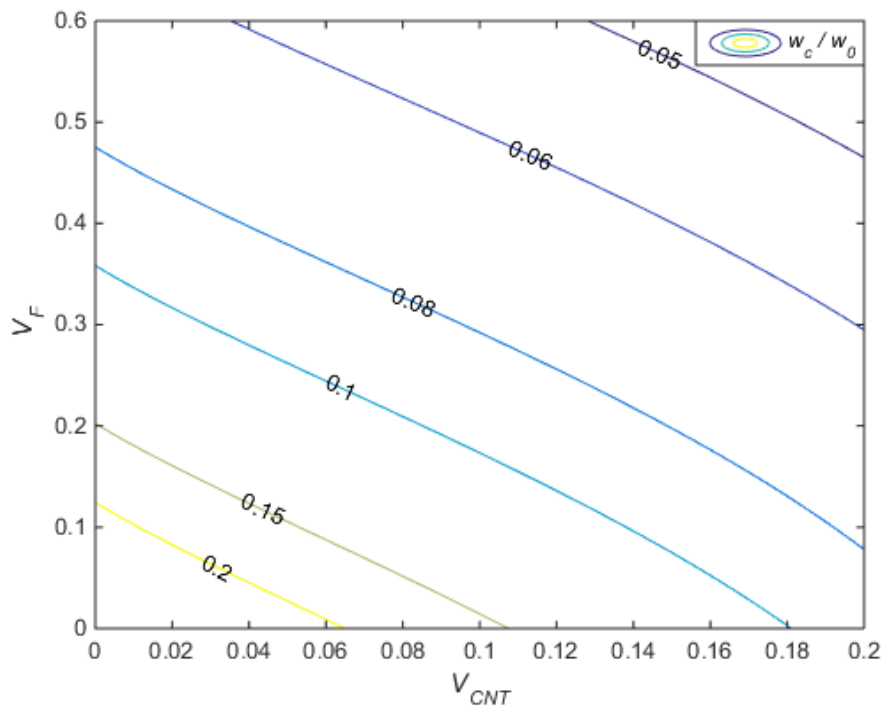


Figure 5-24: Glass fibre reinforced deflection contour for increasing reinforcement volume fraction with agglomeration

5.7. Chapter summary

The deflection behaviour of CNT reinforced epoxy plates was examined in the case of three-phase laminates through the use of micromechanical equations to study the elastic behaviour in terms of fibre volume fraction. Various factors influencing the deflection behaviour of the plate element was also studied.

Firstly, the influence of nanotube diameter on the deflection constant (w_c/w_o) was examined and it was found that as the nanotube diameter decreases so does the degree of deflection, as a result of the nanotube aspect ratio. Next the impact of fibre type was analysed where both carbon and glass fibre reinforcement were taken into consideration. Here, due to the outstanding properties of carbon fibre, the subsequent composites had reduced deflection at the centre of the plate. It can also be concluded that the nanotube reinforcement had a more pertinent effect on the glass fibre reinforced composites.

The reduction of nanotube agglomeration is an active research area as previous studies have found that agglomeration decreases the elastic moduli and subsequently the stiffness. As such the effect of nanotube agglomeration was studied for both carbon and glass fibre reinforced composites. Here, both 40% and 60% nanotube agglomeration scenarios were analysed, and it was found to be in excellent agreement with previous studies where increasing nanotube agglomeration decreases the material stiffness. Next the nanotube orientation and laminate layups were studied. It was found that aligned CNTs possessed superior stiffness compared to the randomly orientated CNTs. A cross-ply laminate was seen to decrease the bending constant. Two-phase and three-phase nanocomposites were compared and the addition of the third constituent resulted in a significantly stiffer material. However, it should be noted that for nanotube volume fractions greater than (13.06%) the addition of glass fibre had less of an impact on the material stiffness compared to the two-phase counterpart. Lastly, contour plots of deflection were generated which analyse the effect of both fibre and nanotube volume fractions. These models were further extended to take into consideration the impact of CNT agglomeration.

It is concluded that the numerical results given in this study provided a quantitative assessment of the effects of different reinforcement scenarios and the volume fractions on the static behaviour of laminated composites.

6. Discussion

The effect of CNT orientation and agglomeration on the flexural properties of CNT reinforced epoxy nanocomposites were examined using micromechanical methods. Epoxy matrix reinforced with evenly distributed, aligned CNTs, randomly orientated CNTs and agglomerated CNTs were analysed respectively. The straight, aligned CNT model showed a rapid increase in Young's longitudinal modulus for increasing nanotube volume fraction. Though, the transverse modulus normal to the fibre direction only increased initially with increasing nanotube volume fraction as this is due to the transversely isotropic properties of nanotubes but tapered off significantly at $V_{CNT}=0.007$.

Using a modified Mori-Tanaka approach, significant improvements on the elastic properties of epoxy was observed for the addition of straight, randomly oriented CNTs. These results suggest the possibility of tailoring the properties of CNT based composites by controlling the orientation of the nanotubes. Experimental studies on nanotube-reinforced epoxy-based composites have shown limited ability to control the dispersion of CNTs within the matrix. The influence of distribution of the nanotubes within the matrix was analysed using an Eshelby's inclusion model, where spherical inclusions with concentrated nanotube clusters are assumed. The results obtained showed a significant impact on the elastic properties when nanotubes are concentrated in agglomerations.

The effective elastic modulus vs carbon nanotube weight fraction was analysed and compared to practical results obtained by Shokrieh et al. (2017). It was found that the results obtain from the theoretical micromechanical analyses correlated closely to those of the practical results. An average difference of 0.64% was found between 0 and 1% weight fraction when comparing theoretical and practical results. Furthermore, an inversely linear relationship was observed between the longitudinal modulus and agglomeration effect. The relationship showed that as agglomeration decreases, the longitudinal modulus increases.

The analysis was furthered by developing computational models to analyse the effects of three-phase nanocomposites. Three scenarios were analysed. Firstly, the engineering constants for three-phase nanocomposites with straight, aligned CNTs were analysed for both glass and carbon fibre reinforced composites. Secondly, the same scenario was extended to straight, randomly orientated CNTs, and lastly the effects of nanotube agglomeration on three-phase composites were analysed.

An outstanding agreement was found between the present results obtained and those provided in literature for 45% reinforced carbon fibre nanocomposites. Experimental data for hybrid composites has been investigated extensively by academics such as Gholami et al. (2018). It was found that the RoHM can, with reasonable accuracy, predict the transverse and longitudinal moduli of hybrid composites (Banerjee et al. 2014). This is in agreement with the results presented in this dissertation. However, the RoHM can only predict the longitudinal Young's modulus with reasonable accuracy for low mass fraction of carbon. Considering the effect of nanotube agglomeration, a stronger resemblance between the experimental data from literature and the results obtained in this dissertation can be observed.

It was seen that for increasing volume fraction of carbon nanotubes, a noticeable impact was noted on the flexural response of glass fibre reinforced composites as opposed to the carbon fibre reinforced composites. This is as a result of the outstanding elastic properties of the carbon fibre constituent. Furthermore, the results obtained from the three-phase micromechanical analysis can be used to model composite structures.

The deflection behaviour of CNT reinforced epoxy plates was examined in the case of three-phase laminates by using micromechanical techniques to evaluate the elastic behaviour with regards to fibre volume fraction. Furthermore, the influence of factors such as nanotube diameter, composite layup and varying material compositions on the deflection behaviour was also studied.

Firstly, the impact of nanotube diameter on the deflection constant was examined and it was found that as the nanotube diameter decreases so does the degree of deflection, as a result of the nanotube aspect ratio. Next the impact of fibre type was analysed where both carbon and glass fibre reinforcement were taken into consideration. Here, due to the outstanding properties of carbon fibre, the subsequent composites had reduced deflection at the centre of the plate. It can also be concluded that the nanotube reinforcement had a more pertinent effect on the glass fibre reinforced composites.

The reduction of nanotube agglomeration is an active research area as previous studies have found that agglomeration decreases the elastic moduli and subsequently the material stiffness. As such the effect of nanotube agglomeration was studied for both carbon and glass fibre reinforced composites. Here 40% and 60% nanotube agglomeration models were analysed, and the results obtained agreed with previous literature where increasing nanotube agglomeration decreases the material stiffness. Next the effect of nanotube orientation and

laminate layups were studied. It was found that aligned CNTs possessed superior stiffness properties compared to the randomly orientated CNTs. A cross-ply laminate layup was seen to decrease the bending constant. Two-phase and three-phase nanocomposites were compared and the addition of the third constituent resulted in a significantly stiffer material. However, it should be noted that for nanotube volume fractions greater than 13.06%, the addition of glass fibre had less of an impact on the material stiffness compared to the two-phase counterpart. Lastly, contour plots of deflection were generated which analyse the effect of both fibre and nanotube volume fractions. These models were further extended to take into consideration the effect of nanotube agglomeration.

Future optimisation of the analysis may include the effect of nanotube waviness (analyses of curved nanotubes) as research has previously shown this to impact the material properties of nanotube reinforced composites. Furthermore, perfect bonding between the matrix and fibre should not be assumed and the impact of this should be taken into consideration when assessing the correction factor. The replacement and comparison of CNTs with graphene platelets would align the dissertation with current capabilities in practical research of nanotechnology. The dissertation would also benefit from extending the current research to different material layups and loading conditions, whilst supporting the findings with concurring practical results. Additionally, the effects of temperature, strain rate and the variances in structural behaviour of different CNT arrangements will make for an interesting and in-depth research topic.

7. Conclusion

In this dissertation the addition of nanomaterials to conventional composites as reinforcement resulted in a new generation of composites, namely, multiscale composites. Multiscale composites comprise of reinforcements from two or more different length scales such as macro, micro and nano (three-phase), hence the name multiscale. This dissertation detailed the analysis of carbon nanotube reinforced composites. The key focus areas included micromechanical modelling of both two and three phase nanocomposites along with their applications to structural elements. Furthermore, the flexural behaviour of a simply supported hybrid plate element subjected to a uniform transverse pressure was analysed under various conditions. These composites exhibit high strength and stiffness to weight ratios as compared to fibre composites.

Firstly, the effects of CNT orientation and agglomeration on the flexural properties of CNT reinforced epoxy nanocomposites (two-phase nanocomposites) were examined using micromechanical methods. Epoxy matrix reinforced with evenly distributed, aligned CNTs, randomly orientated CNTs and agglomerated CNTs were analysed respectively. The straight, aligned CNT model showed a rapid increase in Young's longitudinal modulus for increasing nanotube volume fraction. Though, the transverse modulus normal to the fibre direction only increased initially with increasing nanotube volume fraction as a result of the transversely isotropic properties of nanotubes but tapered off significantly at $V_{CNT}=0.7\%$.

Significant improvements in the elastic properties of epoxy were demonstrated for the addition of straight, randomly oriented CNTs. These results suggest the possibility of tailoring the properties of CNT based composites by controlling the orientation of the nanotubes. However, assumptions such as the distribution, length and waviness need to be considered for a more detailed analysis. Experimental studies on nanotube-reinforced epoxy-based composites have shown limited ability to control the dispersion of CNTs within the matrix. The influence of distribution of the nanotubes within the matrix was analysed using Eshelby's inclusion model. Analysis of the results reveals that the value of elastic modulus for agglomerated composites has a maximum value when the nanotubes are completely dispersed within the matrix, i.e. $\xi=1$. The value of elastic modulus then decreases rapidly with increasing agglomeration parameter ξ .

Additionally, the effects of CNT orientation and agglomeration on the flexural properties of CNT-reinforced epoxy nanocomposites (three-phase nanocomposites) were investigated. Three scenarios were analysed. Firstly, the engineering constants for three-phase

nanocomposites with straight, aligned nanotubes were analysed for glass and carbon fibre reinforced composites. Secondly, the same scenario was extended to straight, randomly orientated CNTs, and lastly the effects of nanotube agglomeration on three-phase composites were analysed. An excellent agreement can be found between the present results and those provided in literature with an average difference in Young's modulus of 0.64% for 0-1 wt% CNT.

Experimental data for hybrid composites has been studied extensively by academics such as Gholami et al. (2018) and Banerjee et al. (2014) who found that the RoHM can be used to predict the longitudinal and transverse moduli of hybrid composites. This is consistent with the results presented in this dissertation. However, it was found that the RoHM can only predict the longitudinal Young's modulus with reasonable accuracy for low mass fraction of CNTs, typically less than 0.5% CNT weight fraction. Also, for increasing nanotube volume fraction, a more pronounced impact on the flexural response of glass fibre reinforced composites as opposed to the carbon fibre reinforced composites can be observed. This is due to the outstanding material properties of carbon fibre, with a Young's modulus three times that of glass fibre thus resulting in the nanotubes having less of an influence on carbon fibre composites.

Furthermore, the results obtained from the three-phase micromechanical analysis was then utilised to model nano-structures to study the deflection behaviour of CNT reinforced epoxy plates for three-phase laminates through the use of micromechanical equations for varying fibre volume fraction. Various factors influencing the deflection behaviour of the plate element was also studied. Firstly, the influence of nanotube diameter on the plate deflection was examined and it was found that as the nanotube diameter increases the degree of deflection decreases, with an average decrease in deflection of 66% for CNT volume fraction greater than 10% when increasing the nanotube diameter from 2nm to 22.3nm.

Next the impact of fibre type was analysed where both carbon and glass fibre reinforcement were taken into consideration. Here, due to the outstanding properties of carbon fibre, with a Young's modulus 3 times that of glass fibre, the subsequent composites experienced reduced deflection at the centre of the plate. It can also be concluded that the nanotube reinforcement had a more pertinent effect on the glass fibre reinforced composites.

The reduction of nanotube agglomeration is an active research area as previous studies have found that agglomeration decreases the elastic moduli and subsequently the stiffness. As such

the effect of nanotube agglomeration was studied for both carbon and glass fibre reinforced composites. Here, both 40% and 60% nanotube agglomeration scenarios were analysed, and it was found to be in excellent agreement with previous studies where increasing nanotube agglomeration decreases the material stiffness.

Next the nanotube orientation and laminate layups were studied. It was found that aligned CNTs possessed superior stiffness compared to the randomly orientated CNTs. For 45% carbon fibre reinforced composites, aligned nanotubes resulted in a 51% reduction in deflection for a 20% CNT volume fraction hybrid composite. Furthermore, a cross-ply laminate, $[90^\circ/0^\circ/90^\circ/0^\circ]_s$, was seen to decrease the bending constant by 85% for a 10% CNT volume fraction hybrid composite when compared to a $[45^\circ/0^\circ/45^\circ/0^\circ]_s$ layup. Two-phase and three-phase nanocomposites were compared and the addition of the third constituent resulted in a significantly stiffer material.

Lastly, contour plots of deflection were generated which analyse the effect of both fibre and nanotube volume fractions. These models were further extended to take into consideration the impact of CNT agglomeration able to depict the deflection of both carbon and glass fibre reinforced hybrid plates in bending for increasing volume fraction. As expected, the plate deflection decreases for increasing fibre and nanotube volume fraction.

It is concluded that the numerical results given in this study provides a quantitative analysis of the effects of different types of CNT parameters, fibre reinforcements and the volume fractions on the static behaviour of laminated composites.

8. References

- Ahmadi, M, Ansari, R, Rouhi, H, 2017. Multi-scale bending, buckling and vibration analyses of carbon fibre/carbon nanotube-reinforced polymer nanocomposite plates with various shapes. *Physica E*, 93, 17–25.
- Ahmadi, M, Ansari, R, Rouhi, H, 2018. Free vibration analysis of carbon fiber-carbon nanotube-polymer matrix composite plates by a finite element-based multi-scale modelling approach. *Journal of Multiscale Modelling*, 9(1).
- Al-Saleh, MH, Sundararaj, U, 2011. Review of the mechanical properties of carbon nanofiber/polymer composites. *Composites Part A: Applied Science and Manufacturing*, 42(12), 2126–2142.
- Amiot, C, Xu, S, Liang, S, Pan, L, Zhao, J, 2008. Near-Infrared Fluorescent Materials for Sensing of Biological Targets. *Sensors*, 8(5), 3082–3105.
- Anumandla, V, Gibson, RF, 2006. A comprehensive closed form micromechanics model for estimating the elastic modulus of nanotube-reinforced composites. *Composites A: Appl Sci Manuf*, 37, 2178–2185.
- Aqel, A, El-Nour, K, Ammar, R, Al-Warthan, A, 2012. Carbon nanotubes, science and technology part (I) structure, synthesis and characterisation. *Arabian Journal of Chemistry*, 5(1), 1–23.
- Arash, B, Wang, Q, Varadan, VK, 2014. Mechanical properties of carbon nanotube/polymer composites. *Science Reports*, 4(6479).
- Arroyo, M, Belytschko, T, 2004. Finite crystal elasticity of carbon nanotubes based on the exponential Cauchy-Born rule. *Phys. Rev. B*, 69, 115415.
- Ávila, A, 2008. Molecular mechanics applied to single-walled carbon nanotubes. *Materials Research*. Available at: http://www.scielo.br/scielo.php?script=sci_arttext&pid=S1516-14392008000300016.
- Azam, M, 2017. Review—Critical Considerations of High Quality Graphene Synthesized by Plasma-Enhanced Chemical Vapor Deposition for Electronic and Energy Storage Devices. *ECS Journal of Solid State Science and Technology*, 6, 3035-3048.
- Banerjee, S, Sankar, BV, 2014. Mechanical properties of hybrid composites using finite element method based micromechanics. *Composites Part B: Engineering*, 58, 318–327.

- Batra, RC, Sears, A, 2007. Uniform radial expansion/contraction of carbon nanotubes and their transverse elastic moduli. *Modelling and Simulation in Materials Science and Engineering*, 15, 835-844.
- Bekyarova, E, Thostenson, ET, Yu, A, Kim, H, Gao, J, Tang, J, Hahn, HT, Chou, TW, Itkis, ME, Haddon, RC, 2007. Multiscale carbon nanotube–carbon fiber reinforcement for advanced epoxy composites. *Langmuir*, 23, 3970–3974.
- Belytschko, T, Xiao, SP, Schatz, GC, Ruoff, RS, 2002. Atomistic simulations of nanotube fracture. *Physical Review B*, 65(23).
- Bethune, DS, Kiang, CH, de Vries, MS, Gorman, G, Savoy, R, Vazquez, J, Beyers, R, 1993. Cobalt-catalysed growth of carbon nanotubes with single-atomic-layer walls. *Nature*, 363(6430), 605–607.
- Birman, V, 2011. *Plate structures*. 1st ed. Missouri: Springer Science & Business Media.
- Brcic, M, Canadija, M, Brnic, J, 2013. Estimation of material properties of nanocomposite structures. *Meccanica*, 48, 2209-2220.
- Chang, T, Gao, H, 2003. Size-dependent elastic properties of a single-walled carbon nanotube via a molecular mechanics model. *Journal of the Mechanics and Physics of Solids*, 51, 1059-1074.
- Chang, T, 2010. A molecular based anisotropic shell model for single-walled carbon nanotubes. *Journal of the Mechanics and Physics of Solids*, 58, 1422-1433.
- Cheng, HC, Liu, YL, Hsu, YC, Chen, WH, 2009. Atomistic-continuum modeling for mechanical properties of single-walled carbon nanotubes. *International Journal of Solids and Structures*, 46, 1695 - 1704.
- Cho, SJ, Boo, JH, 2012. A study on the characteristics of plasma polymer thin film with controlled nitrogen flow rate. *Nanoscale Research Letters*, 7(1), 62.
- Collins, PG, Bradley, K, Ishigami, M, Zettl, A, 2000. Extreme Oxygen Sensitivity of Electronic Properties of Carbon Nanotubes. *Science, New Series*, 287(5459), 1801-1804.
- Contreras, ML, Ávila, D, Alvarez, J, Rozas, R, 2012. Computational algorithms for fast-building 3D carbon nanotube models with defects. *Journal of Molecular Graphics and Modelling*, 38, 389-395.

- Dekker, C, 1999. Carbon Nanotubes as Molecular Quantum Wires. *Physics Today*, 52(5), 22–28.
- Dresselhaus, D, Gene, A, Phaedon, M, 2000. *Carbon Nanotubes: Synthesis, Structure, Properties, and Applications*. 1st ed. Berlin Heidelberg: Springer-Verlag.
- Elbadry, EA, GA, A, M, A, EA, O, 2018. Effect of Glass Fibers Stacking Sequence on the Mechanical Properties of Glass Fiber/Polyester Composites. *Journal of Material Science & Engineering*, 07(1).
- Ermakova, MA, Ermakov, DY, Chuvilin, AL, Kuvshinov, GG, 2001. Decomposition of Methane over Iron Catalysts at the Range of Moderate Temperatures: The Influence of Structure of the Catalytic Systems and the Reaction Conditions on the Yield of Carbon and Morphology of Carbon Filaments. *Journal of Catalysis*, 201(2), 183–197.
- Fan, S, 1999. Self-Oriented Regular Arrays of Carbon Nanotubes and Their Field Emission Properties. *Science*, 283(5401), 512–514.
- Fisher, FT, Bradshaw, RD, Brinson, LC, 2002. Effects of nanotube waviness on the modulus of nanotube-reinforced polymers. *Applied Physics Letters*, 80(24), 4647–4649.
- Fisher, FT, Bradshaw, RD, Brinson, LC, 2003. Fiber waviness in nanotube-reinforced polymer composites—I: Modulus predictions using effective nanotube properties. *Composite Science and Technology*, 63, 1689–1703.
- Foroughi, H, 2013. Mechanical Buckling of Thick Composite Plates Reinforced with Randomly Oriented, Straight, Single-Walled Carbon Nanotubes Resting on an Elastic Foundation using the Finite Strip Method. *Journal of Nanomechanics and Micromechanics*, 3, 10.
- Francisco, J, 2010. *Sensors Based on Nanostructured Materials*. 2nd ed. United States: Springer Science & Business Media.
- Ganji, MD, Mirnejad, A, Najafi, A, 2010. Theoretical investigation of methane adsorption onto boron nitride and carbon nanotubes. *Science and Technology of Advanced Materials*, 11(4).
- Gao, X, 2005. A shear-lag model for carbon nanotube-reinforced polymer composites. *International Journal of Solids and Structures*, 42(6), 1649-1667.
- Ghavanloo, A, Rafii-Tabar, H, Fazelzadeh, S, 2019. *Computational Continuum Mechanics of Nanoscopic Structures: Nonlocal Elasticity Approaches*. 1st ed. London: Springer International Publishing.

- Ghasemi, AR, Mohammadi, MM, Mohandes, MA, 2015. The Role of Carbon Nanofibers on Thermo Mechanical Properties of Polymer Matrix Composites and Their Effect on Reduction of Residual Stresses. *Composites Part B: Engineering*, 77.
- Gholami, R, Ansari, R, Gholami, Y, 2018. Numerical study on the nonlinear resonant dynamics of carbon nanotube/fiber/polymer multiscale laminated composite rectangular plates with various boundary conditions. *Aerospace Science and Technology*, 78, 118–129.
- Gholami, R, Ansari, R, 2017. Large deflection geometrically nonlinear analysis of functionally graded multilayer graphene platelet-reinforced polymer composite rectangular plates. *Composite Structures*, 180, 760–771.
- Gholami, R, Ansari, R, 2018. Nonlinear harmonically excited vibration of third order shear deformable functionally graded graphene platelet-reinforced composite rectangular plates. *Engineering Structures*, 156, 197–209.
- Gholami, R, Ansari, R, 2018. Nonlinear harmonically excited vibration of third-order shear deformable functionally graded graphene platelet-reinforced composite rectangular plates. *Engineering Structures*, 156, 197-209.
- Green, KJ, Dean, DR, Vaidya, UK, Nyairo, E, 2009. Multiscale fiber reinforced composites based on a carbon nanofiber/epoxy nanophased polymer matrix: Synthesis, mechanical, and thermomechanical behaviour. *Composites, Part A, Appl. Sci. Manuf.*, 40, 1470–1475.
- Halpin, JC, Kardos, JL, 1976. The Halpin–Tsai equations: A review. *Polymer and Engineering Science*, 16, 344–352.
- Harris, P, 1999. *Carbon Nanotubes and Related Structures: New Materials for the Twenty-first Century*. 1st ed. Cambridge: Cambridge University Press.
- Hassan, S, Suzuki, M, Mori, S, El-Moneim, AA, 2014. MnO₂/carbon nanowalls composite electrode for supercapacitor application. *Journal of Power Sources*, 249, 21–27.
- Hassan, A, Yahya, R, Rafiq, MIM, Hussin, A, Sheikh, MRK, Hornsby, PR, 2011. Interfacial shear strength and tensile properties of injection-molded, short- and long-glass fiber-reinforced polyamide 6,6 composites. *Journal of Reinforced Plastics and Composites*, 30(14), 1233–1242.

- He, X, Rafiee, M, Mareishi, S, Liew, K, 2015. Large amplitude vibration of fractionally damped viscoelastic CNTs/fiber/polymer multiscale composite beams. *Composite Structures*, 131, 1111–1123.
- Hernández, E, Goze, C, Bernier, P, Rubio, A, 1998. Elastic Properties of C and BxCyNz Composite Nanotubes. *Physical Review Letters*, 80(20), 4502–4505.
- Hill, R, 1965. A Self-Consistent Mechanics of Composite Materials. *Mech. Phys. Solids*, 13, 213-222.
- Hu, Y, Liew, K, Wang, Q, He, X, Yakonson, B, 2008. Nonlocal shell model for elastic wave propagation in single- and double-walled carbon nanotubes. *Journal of the Mechanics and Physics of Solids*, 56(12), 3475–3485.
- Janas, D, Koziol, KK, 2016. Carbon nanotube fibers and films: synthesis, applications and perspectives of the direct-spinning method. *Nanoscale*, 8(47), 19475–19490.
- Journet, C, Maser, WK, Bernier, P, Loiseau, A, de la Chapelle, ML, Lefrant, S, Fischer, JE, 1997. Large-scale production of single-walled carbon nanotubes by the electric-arc technique. *Nature*, 388(6644), 756–758.
- Kamarian, S, 2016. Free vibration analysis of conical shells reinforced with agglomerated Carbon Nanotubes. *International Journal of Mechanical Sciences*, 108, 157-165.
- Kamarian, S, Shakeri, M, Yas, MH, 2018. CNT/fiber/polymer hybrid composites plates using Mori-Tanaka approach, GDQ technique, and firefly algorithm. *Polymer Composites*, 39, 1433–1446.
- Karthikeyan, S, Mahalingam, P, Karthik, M, 2009. Large Scale Synthesis of Carbon Nanotubes. *E-Journal of Chemistry*, 6(1), 1–12.
- Katili, I, 1993. A new discrete Kirchhoff-Mindlin element based on Mindlin-Reissner plate theory and assumed shear strain fields—part I: An extended DKT element for thick-plate bending analysis. *International Journal for Numerical Methods in Engineering*, 36, 1859-1883.
- Krishnan, A, Dujardin, E, Ebbesen, TW, Yianilos, PN, Treacy, MMJ, 1998. Young's modulus of single-walled nanotubes. *Phys. Rev. B*, 58, 14013-14019.
- Kundalwal, SI, Ray, MC, 2013. Effect of carbon nanotube waviness on the elastic properties of the fuzzy fiber reinforced composites. *Journal of Applied Mechanics*, 80(2).

Li, C, Chou, TA, 2003. A structural mechanics approach for the analysis of carbon nanotubes. *International Journal of Solids and Structures*, 40, 2487-2499.

Iijima, S, Ichihashi, T, 1993. Single-shell carbon nanotubes of 1-nm diameter. *Nature*, 363(6430), 603–605.

Liu, YJ, Chen, XL, 2003. Evaluations of the effective material properties of carbon nanotube-based composites using a nanoscale representative volume element. *Mechanics of Materials*, 1, 69-81.

Loos, M, 2014. *Carbon Nanotube Reinforced Composites: CNT Polymer Science and Technology*. 1st ed. Western Reserve University: William Andrew.

Lu, JP, 1997. Elastic Properties of Carbon Nanotubes and Nanoropes. *Physical Review Letters*, 79(7), 1297–1300.

Miyagawa, H, Sato, C, Mase, T, Drown, E, Drzal, LT, Ikegami, K, 2005. Transverse elastic modulus of carbon fibers measured by Raman spectroscopy. *Materials Science and Engineering: A*, 412(1-2), 88–92.

Montazeri, N, 2011. The Effect of Sonication Time and Dispersing Medium on the Mechanical Properties of Multiwalled Carbon Nanotube (MWCNT)/Epoxy Composite. *Journal of Polymer Analysis and Characterization*, 16(7), 465-476.

Mori, T, Tanaka, K, 1973. Average stress in matrix and average elastic energy of materials with misfitting inclusions. *Acta Metallurgica*, 21(5), 571–574.

Mehta, G, 2014. Carbon nanotubes: A promising tool in drug delivery. *International Journal of Pharma and Bio Sciences*, 5, 533-555.

Meo, M, Rossi, M, 2006. Tensile failure prediction of single wall carbon nanotube. *Engineering Fracture Mechanics*, 73, 2589-2599.

Mura, T, 1987. *Micromechanics of Defects in Solids*, Martinus Nijhoff Publishers, Dordrecht.

MWCNT TEM & SEM 분석 사진. 2018. *MWCNT TEM & SEM 분석 사진*. Available at: http://www.carbonnano.co.kr/english/product/win/mwcnt_win05.htm.

NASA, 2015. NASA Technology Roadmaps. Available at: https://www.nasa.gov/sites/default/files/atoms/files/2015_nasa_technology_roadmaps_ta_10_nanotechnology_final.pdf.

Odegard, G, Clancy, T, Gates T, 2005. Modeling of the mechanical properties of nanoparticle/polymer composites. *Polymer*, 46, 553–562.

Pan, SS, Xie, BH, Chang, LF, Sun, WY, Zhou, G, Wang, ZW, 1999. Direct growth of aligned open carbon nanotubes by chemical vapor deposition. *Arabian Journal of Chemistry*, 9(2), 171-178.

Pan, Z, 2000. Carbon nanotube arrays. *Materials Science and Engineering: A*, 286, 11-15.

Poncharal, P, Wang, ZL, Ugarte, D, de Heer, WA, 1999. Electrostatic Deflections and Electromechanical Resonances of Carbon Nanotubes. *Science*, 283, 1513-1516.

Popov, VN, Van Doren, VE, Balkanski, M, 2000. Elastic properties of crystals of single-walled carbon nanotubes. *Solid State Communications*, 114(7), 395–399.

Prasek, J, Drbohlavova, J, Chomoucka, J, Hubalek, J, Jasek, O, Adam, V, Kizek, R, 2011. Methods for carbon nanotubes synthesis—review. *Journal of Materials Chemistry*, 21(40), 15872.

Purohit, R, Purohit, K, Rana, S, Rana, RS, Patel, V, 2014. Carbon Nanotubes and Their Growth Methods. *Procedia Materials Science*, 6, 716–728.

Quantopticon Ltd, 2018. Optical Activity of a Carbon Nanotube. Available at: https://www.google.co.za/search?q=unit+cell+and+chiral+vector&safe=off&rlz=1C1CAFA_enZA641ZA642&source=Inms&tbn=isch&sa=X&ved=0ahUKEwilqqbRpZfeAhVIOhokHYjyD9EQ_AUIDigB&biw=1366&bih=577#imgrc=nQ8xk_guPihrmM.

Rafiee, M, He, X, Mareishi, S, Liew, K, 2014. Modeling and stress analysis of smart CNTs/fiber/polymer multiscale composite plates. *Int. J. of Applied Mechanics*, 6.

Ray, HB, Anvar, AZ, de Heer, W, 2002. Carbon Nanotubes: The Route toward Applications. *Science*, 297(5582), 787-792.

Roatta, A, Bolmaro, RE, 1997. An Eshelby inclusion-based model for the study of stresses and plastic strain localization in metal matrix composites I: General formulation and its application to round particles. *Materials Science and Engineering: A*, 229(1-2), 182–191.

- Roldo, M, Fatouros, DG, 2013. Biomedical applications of carbon nanotubes. Annual Reports Section "C" (Physical Chemistry), 109, 10.
- Ru, CQ, 2000. Effective bending stiffness of carbon nanotubes. Physical Review B, 62(15), 9973–9976.
- Saetta, A, 1990. A finite element formulation for shells of arbitrary geometry. Computers and structures, 37, 781-793.
- Saifuddin, N, Raziah, AZ, Junizah, AR, 2012. Carbon Nanotubes: A Review on Structure and Their Interaction with Proteins. Journal of Chemistry, 2013.
- Saito, R, Takeya, T, Kimura, T, Dresselhaus, G, Dresselhaus, MS, 1998. Raman intensity of single-wall carbon nanotubes. Physical Review B, 57(7), 4145–4153.
- Salvetat, JP, Bonard, JM, Thomson, NH, Kulik, AJ, Forró, L, Benoit, W, Zuppiroli, L, 1999. Mechanical properties of carbon nanotubes. Applied Physics A, 69, 255–260.
- Sánchez-Portal, D, Artacho, E, Soler, JM, Rubio, A, Ordejón, P, 1999. Ab initio structural, elastic, and vibrational properties of carbon nanotubes. Physical Review B, 59(19), 12678–12688.
- Schlittler, RR, Seo, JW, Gimzewski, JK, Durkan, C, Saifullah, MSM, Welland, ME, 2001. Single Crystals of Single-Walled Carbon Nanotubes Formed by Self-Assembly. Science, New Series, 292, 1136-1139.
- Seidel, GD, Lagoudas, DC, 2006. Micromechanical analysis of the effective elastic properties of carbon nanotube reinforced composites. Mechanics of Materials, 38, 884–907.
- Seidi, J, Kamarian, S, 2017. Free vibrations of non-uniform CNT/fiber/polymer nanocomposite beams. Curved and Layered Structures, 4(1).
- Shao, LH, 2009. Prediction of effective moduli of carbon nanotube–reinforced composites with waviness and debonding. Composite Structures, 87, 274–281.
- Shokrieh, M, Rafiee, R, 2010. A review of the mechanical properties of isolated carbon nanotubes and carbon nanotube composites. Mechanics of Composite Materials, 46, 155–172.
- Shokrieh, MM, Rafiee, R, 2010. Prediction of Young's modulus of graphene sheets and carbon nanotubes using nanoscale continuum mechanics approach. Materials & Design, 31(2), 790–795.

- Sheng, N, Boyce, MC, Parks, DM, 2004. Multiscale micromechanical modelling of polymer/clay nanocomposites and the effective clay particle. *Polymer*, 45, 487–506.
- Shi, DL, Feng, XQ, Huang, YY, Hwang, KC, Gao, H, 2004. The Effect of Nanotube Waviness and Agglomeration on the Elastic Property of Carbon Nanotube-Reinforced Composites. *Journal of Engineering Materials and Technology*, 126(3), 250.
- Shokrieh, MM, Daneshvar, A, 2017. A Novel Technique to Simulate Reduced Residual Stresses in Laminated Composites Using Nanoparticles. *Iranian Journal of Science and Technology, Transactions of Mechanical Engineering*.
- Silvestre, N, Wang, CM, Zhang, YY, Xiang, Y, 2011. Sanders shell model for buckling of single-walled carbon nanotubes with small aspect ratio. *Composite Structures*, 93, 1683-1691.
- Smith, A, Wilkinson, SJ, Reynolds, WN, 1974. The elastic constants of some epoxy resins. *Journal of Materials Science*, 9(4), 547–550.
- Szabó, A, Perri, C, Csató, A, Giordano, G, Vuono, D, Nagy, JB, 2010. Synthesis Methods of Carbon Nanotubes and Related Materials. *Materials*, 3(5), 3092–3140.
- Tadmor, EB, Phillips, R, Ortiz, M, 1996. Mixed Atomistic and Continuum Models of Deformation in Solids. *Langmuir*, 12, 4529-4534.
- Takenaka, S, Shigeta, Y, Tanabe, E, Otsuka, K, 2003. Methane decomposition into hydrogen and carbon nanofibers over supported Pd–Ni catalysts. *Journal of Catalysis*, 220(2), 468–477.
- Terrones, M, Terrones, H, Banhart, F, Charlier, JC, Ajayan, PM, 2000. Coalescence of Single-Walled Carbon Nanotubes. *Science, New Series*, 288(5469) 1226-1229.
- Tersoff, J, 1992. Energies of fullerenes. *Phys. Rev. B*, 46, 15546-15549.
- Thostenson, ET, Li, W, Wang, D, 2002. Carbon nanotube/carbon fiber hybrid multiscale composites. *J Applied Physics*, 91, 6034–6037.
- Thostenson, ET, Ren, Z, Chou, TW, 2001. Advances in the science and technology of carbon nanotubes and their composites: a review. *Composites Science and Technology*, 61(13), 1899–1912.
- Treacy, MMJ, Ebbesen, TW, Gibson, JM, 1996. Exceptionally high Young's modulus observed for individual carbon nanotubes. *Nature*, 381(6584), 678–680.

Vajtai, R, 2013. Springer Handbook of Nanomaterials. 1st ed. Berlin Heidelberg: Springer Science & Business Media.

Vodenitcharova, T, Zhang, LC, 2006. Bending and local buckling of a nanocomposite beam reinforced by a single-walled carbon nanotube. *International Journal of Solids and Structures*, 43, 3006-3024.

Vidya-mitra: Integrated e-Content Portal, 2018. Introduction to Plate Bending Problems. Available at: http://content.inflibnet.ac.in/data-server/eacharya-documents/55da9cb2e41301e54e2caeb7_INFIEP_206/1211/ET/206-1211-ET-V1-S1__32.pdf.

Wang, CM, Roy, CAN, Koh, SJA, Zhang, YY, 2014. Molecular Dynamics Simulation and Continuum Shell Model for Buckling Analysis of Carbon Nanotubes. *Modeling of Carbon Nanotubes, Graphene and their Composites*, 188.

Wang, Y, Wang, X, Ni, X, 2004. Atomistic simulation of the torsion deformation of carbon nanotubes. *Modelling and Simulation in Materials Science and Engineering*, 12, 1099-1107.

Wang, CY, Zhang, LC, 2008. A critical assessment of the elastic properties and effective wall thickness of single-walled carbon nanotubes. *Nanotechnology*, 19, 075705.

Wernik, JM, Meguid, SA, 2010. Atomistic-based continuum modeling of the nonlinear behavior of carbon nanotubes. *Acta Mechanica*, 212, 167-179.

Wong, EW, Sheehan, PE, Lieber, CM, 1997. Nanobeam Mechanics: Elasticity, Strength, and Toughness of Nanorods and Nanotube. *Science*, 277, 1971-1975.

Wu, J, Hwang, KC, Huang, Y, 2008. An atomistic-based finite-deformation shell theory for single-wall carbon nanotubes. *Journal of the Mechanics and Physics of Solids*, 56, 279-292.

Wuite, J, 2005. Deflection and stress behaviour of nanocomposite reinforced beams using a multiscale analysis. *Composite Structures*, 71(4), 388-396.

Yakobson, BI, Brabec, CJ, Bernholc, J, 1996. Nanomechanics of Carbon Tubes: Instabilities beyond Linear Response. *Physical Review Letters*, 76(14), 2511–2514.

Yeoh, WM, Lee, KY, Chai, SP, Lee, KT, Mohamed, AR, 2009. Synthesis of high purity multi-walled carbon nanotubes over Co–Mo/MgO catalyst by the catalytic chemical vapor deposition of methane. *Carbon*, 47(12), 2941.

Yu, J, 2011. Classical micromechanics modeling of nanocomposites with carbon nanofibers and interphase. *J Composite Materials*, 45, 2401–2413.

Yu, M, Files, BS, Arepalli, S, Ruoff, RS, 2000. Tensile Loading of Ropes of Single Wall Carbon Nanotubes and their Mechanical Properties. *Phys. Rev. Lett.*, 84, 5552.

Yu, MF, 2004. Fundamental Mechanical Properties of Carbon Nanotubes: Current Understanding and the Related Experimental Studies. *Journal of Engineering Materials and Technology*, 126(3), 271.

Zeng, Q, Li, Z, Zhou, Y, 2006. Synthesis and Application of Carbon Nanotubes. *Journal of Natural Gas Chemistry*, 15(3), 235–246.

Zhang, CL, Shen, HS, 2008. Predicting the elastic properties of double-walled carbon nanotubes by molecular dynamics simulation. *Journal of Physics D: Applied Physics*, 41, 055404.

Zhao, J, Jiang, JW, Jia, Y, Guo, W, Rabczuk, T, 2013. A theoretical analysis of cohesive energy between carbon nanotubes, graphene and substrates. *Carbon*, 57, 108-119.

Appendix A

Samples of MATLAB script files used in the analyses throughout the dissertation.

A.1.1. Reinforcement using straight, aligned carbon nanotubes on two-phase nanocomposites

```
clear all;
```

```
% Reinforcement using straight, aligned carbon nanotubes on two-phase nanocomposites
```

```
% Inputs
```

```
% Carbon nanotube properties (cn):
```

```
kr=30; % (GPa)
```

```
lr=10; % (GPa)
```

```
mr=1; % (GPa)
```

```
nr=450; % (GPa)
```

```
pr=1; % (GPa)
```

```
% Matrix properties (m):
```

```
Em=3.5; % Young's modulus (GPa)
```

```
vm=0.4; % Poisson's ratio
```

```
% Calculations:
```

```
N=1000;
```

```
t=0.2/N;
```

```
Vcn=0:t:0.2;
```

```
for i=1:N+1
```

```
% Volume fraction of matrix:
```

```
Vm(i)=1-Vcn(i);
```

```
% Hill's elastic properties:
```

```
k(i)=(Em*(Em*Vm(i)+2*kr*(1+vm)*(1+Vcn(i)*(1-2*vm)))/(2*(1+vm)*(Em*(1+Vcn(i)-2*vm)+2*Vm(i)*kr*(1-vm-2*vm^2))));
```

```
l(i)=(Em*(Vm(i)*vm*(Em+2*kr*(1+vm))+2*Vcn(i)*lr*(1-vm^2)))/((1+vm)*(2*Vm(i)*kr*(1-vm-2*vm^2)+Em*(1+Vcn(i)-2*vm)));
```

```
n(i)=(Em^2*Vm(i)*(1+Vcn(i)-Vm(i)*vm)+2*Vm(i)*Vcn(i)*(kr*nr-lr^2)*(1+vm)^2*(1-2*vm))/((1+vm)*(2*Vm(i)*kr*(1-vm-2*vm^2)+Em*(1+Vcn(i)-2*vm)))+(Em*(2*Vm(i)^2*kr*(1-vm)+Vcn(i)*nr*(1-2*vm+Vcn(i))-4*Vm(i)*lr*vm)/(2*Vm(i)*kr*(1-vm-2*vm^2)+Em*(1+Vcn(i)-2*vm)));
```

```
p(i)=(Em*(Em*Vm(i)+2*(1+Vcn(i))*pr*(1+vm)))/(2*(1+vm)*(Em*(1+Vcn(i))+2*Vm(i)*pr*(1+vm)));
```

```
m(i)=(Em*(Em*Vm(i)+2*mr*(1+vm)*(3+Vcn(i)-4*vm)))/(2*(1+vm)*(Em*(Vm(i)+4*Vcn(i)*(1-vm))+2*Vm(i)*mr*(3-vm-4*vm^2)));
```

```

% Engineering constants:
E11(i)=n(i)-(l(i)^2/k(i));
v12(i)=l(i)/(2*k(i));
E22(i)=(4*m(i)*(k(i)*n(i)-l(i)^2))/(k(i)*n(i)-l(i)^2+m(i)*n(i));
v21(i)=v12(i)*(E22(i)/E11(i));
v23(i)=(k(i)*n(i)-l(i)^2-m(i)*n(i))/(k(i)*n(i)-l(i)^2+m(i)*n(i));
G12(i)=-2*p(i);
G23(i)=2*m(i);

```

```
end
```

```
% Outputs
```

```
% Graph of effective E11 vs Vcn
```

```

figure(1)
semilogy(Vcn,E11 ,Vcn,E22,'--')
xlabel('\it{V_{CNT}}','FontSize',12)
ylabel('Effective elastic modulus (GPa)','FontSize',12)
%title('Effective elastic modulus')
legend('\it{E_{11}}','\it{E_{22}}')
plottedit on

```

```
% Graph of effective Poisson's ratio vs Vcn
```

```

figure(2)
plot(Vcn,v12)
xlabel('\it{V_{CNT}}','FontSize',12)
ylabel('\it{v_{12}}','FontSize',12)
%title('Effective Poisson's ratio')

```

```
% Graph of effective G12 vs Vcn
```

```

figure(3)
plot(Vcn,G12)
xlabel('\it{V_{CNT}}','FontSize',12)
ylabel('\it{G_{12}} (GPa)','FontSize',12)
%title('Effective shear modulus')
plottedit on

```

A.1.2. Effect of carbon nanotube agglomeration on two-phase nanocomposites

```
clear all
```

```
% Effect of carbon nanotube agglomeration on two-phase nanocomposites
```

```
% Inputs
```

```
% Carbon nanotube properties (cn):
```

```
E11cn=1000; % Young's modulus (Gpa)
```

```

kr=30;    % (GPa)
lr=10;    % (GPa)
mr=1;     % (GPa)
nr=450;   % (GPa)
pr=1;     % (GPa)
rhocn=1680; % Mass density (kg/m^3)
%Vcn=;    % Volume fraction

```

```
% Matrix properties (m):
```

```

Em=3.5;    % Young's modulus (GPa)
rhom=1200; % Mass density (kg/m^3)
vm=0.4;    % Poisson's ratio
Km=4.95;   % Bulk modulus (GPa)
Gm=1.25;   % Shear modulus (GPa)
%Vm=;      % Volume fraction

```

```

u=0.5;    % Agglomeration parameter
n=1;      % Agglomeration parameter

```

```
% Preliminary calculations:
```

```

ar=(3*(Km+Gm)+kr-lr)/(3*(Gm+kr));
br=(1/5)*(((4*Gm+2*kr+lr)/(3*(Gm+kr)))+(4*Gm)/(Gm+pr))+((2*(Gm*(3*Km+Gm)+Gm*(3*Km+7*Gm))/(Gm*(3*Km+Gm)+mr*(3*Km+7*Gm))));
dr=(1/3)*(nr+2*lr+((2*kr+lr)*(3*Km+2*Gm-lr))/(Gm+kr));
nnr=(1/5)*(((2/3)*(nr-lr))+((8*Gm*pr)/(Gm+pr))+((8*mr*Gm*((3*Km)+(4*Gm)))/(3*Km*(mr+Gm)+Gm*(7*mr+Gm)))+(2*(kr-lr)*(2*Gm+lr))/(3*(Gm+kr)));

```

```
% Calculations:
```

```

N=1000;
t=0.2/N;
Vcn=0:t:0.2;

```

```
for i=1:N+1
```

```
% Volume fraction of matrix:
```

```
Vm(i)=1-Vcn(i);
```

```

Kin(i)=Km+((Vcn(i)*n*(dr-3*Km*ar))/(3*(u-Vcn(i)*n+Vcn(i)*n*ar));
Kout(i)=Km+((Vcn(i)*(1-n)*(dr-3*Km*ar))/(3*(1-u-Vcn(i)*(1-n)+Vcn(i)*(1-n)*ar));
Gin(i)=Gm+((Vcn(i)*n*(nnr-2*Gm*br))/(2*(u-Vcn(i)*n+Vcn(i)*n*br));
Gout(i)=Gm+((Vcn(i)*(1-n)*(nnr-2*Gm*br))/(2*(1-u-Vcn(i)*(1-n)+Vcn(i)*(1-n)*br));

```

```

vout(i)=((3*Kout(i)-2*Gout(i))/(2*(3*Kout(i)+Gout(i)));
a(i)=(1+vout(i))/(3*(1-vout(i)));
b(i)=(2*(4-5*vout(i)))/(15*(1-vout(i)));

```

```
K(i)=Kout(i)*(1+(u*((Kin(i)/Kout(i))-1)))/(1+a(i)*(1-u)*((Kin(i)/Kout(i))-1));
```

```
G(i)=Gout(i)*(1+(u*((Gin(i)/Gout(i))-1))/(1+b(i)*(1-u)*((Gin(i)/Gout(i))-1)));
```

```
% Properties of nanocomposite (CNT & matrix):
```

```
E(i)=(9*K(i)*G(i))/(3*K(i)+G(i));
```

```
v(i)=(3*K(i)-2*G(i))/(6*K(i)+2*G(i));
```

```
G(i)=(E(i))/(2*(1+v(i)));
```

```
end
```

```
% Outputs
```

```
% Graph of effective E11 vs Vcn
```

```
figure(1)
```

```
plot(Vcn,E)
```

```
xlabel('\it{V_{CNT}}','FontSize',12)
```

```
ylabel('\it{E_{11}} (GPa)','FontSize',12)
```

```
%legend('30% Carbon fibre','45% Carbon fibre','60% Carbon fibre','30% Glass fibre','45% Glass fibre','60% Glass fibre')
```

```
%title('Effective Elastic Modulus')
```

```
%axis([0 0.2 0 220])
```

```
% Graph of effective G12 vs Vcn
```

```
figure(3)
```

```
plot(Vcn,G)
```

```
xlabel('\it{V_{CNT}}','FontSize',12)
```

```
ylabel('\it{G_{12}} (GPa)','FontSize',12)
```

```
%legend('30% Carbon fibre','45% Carbon fibre','60% Carbon fibre','30% Glass fibre','45% Glass fibre','60% Glass fibre')
```

```
%title('Effective Shear Modulus')
```

```
%axis([0 0.2 1 7])
```

```
% Graph of effective Poisson's ratio vs Vcn
```

```
figure(4)
```

```
plot(Vcn,v)
```

```
xlabel('\it{V_{CNT}}','FontSize',12)
```

```
ylabel('\it{v_{12}}','FontSize',12)
```

```
%legend('30% Carbon fibre','45% Carbon fibre','60% Carbon fibre','30% Glass fibre','45% Glass fibre','60% Glass fibre')
```

```
%title('Effective Poissons Ratio')
```

```
%axis([0 0.2 0.25 0.4])
```

A.1.3. Three-phase, randomly orientated CNT micromechanical analysis

```
clear all
```

```
% Three-phase, randomly orientated CNT micromechanical analysis
```

```
% Inputs (****)
```

```
% Carbon nanotube properties (cn):
```

lcn=8.5e-6; % Length (m)
 dcn=8e-9; % Outer diameter (m)
 tcn=0.8e-9; % Thickness (m)
 E11cn=1000; % Young's modulus (GPa)
 rhocn=1680; % Mass density (kg/m³)
 %Vcn=; % Volume fraction
 %wcn=; % Mass fraction

% Matrix properties (m):

Em=3.5; % Young's modulus (GPa)
 rhom=1200; % Mass density (kg/m³)
 vm=0.4; % Poisson's ratio
 %Vm=; % Volume fraction

% Fibre properties (cf):

Vcf30=0.30; % Volume fraction at 30%
 Vcf45=0.45; % Volume fraction at 45%
 Vcf60=0.60; % Volume fraction at 60%
 E11cf=227; % Young's modulus (GPa)
 E22cf=8; % Young's modulus (GPa)
 vcf=0.3; % Poisson's ratio
 G12cf=27.3; % Shear modulus (Gpa)
 rhocf=1740; % Mass density (kg/m³)

% Glass fibre properties (gf):

Vgf30=0.30; % Volume fraction at 30%
 Vgf45=0.45; % Volume fraction at 45%
 Vgf60=0.60; % Volume fraction at 60%
 E11gf=73.5; % Young's modulus (GPa)
 E22gf=72; % Young's modulus (GPa)
 vgf=0.22; % Poisson's ratio
 G12gf=33; % Shear modulus (Gpa)
 rhogf=2570; % Mass density (kg/m³)

% Matrix of nanocomposite (mnc) properties:

%Vmnc=; % Volume fraction
 %Emnc=; % Young's modulus (GPa)
 %vmnc=; % Poisson's ratio
 %Gmnc=; % Shear modulus (GPa)
 %rhomnc=; % Mass density (kg/m³)

% Preliminary calculations:

Bdl=(((E11cn/Em)-(dcn/4*tcn))/((E11cn/Em)+(lcn/2*tcn)));
 Bdd=(((E11cn/Em)-(dcn/4*tcn))/((E11cn/Em)+(dcn/2*tcn)));
 vmnc=vm;

```

% Calculations:

% 30% carbon fibre volume fraction

N=1000;
t=0.2/N;
Vcn=0:t:0.2;

for i=1:N+1

% Volume fraction of carbon nanotubes based on mass fraction:
Vm(i)=1-Vcf30-Vcn(i);

% Properties of nanocomposite (CNT & matrix):
Vmnc(i)=Vm(i)+Vcn(i);
Emnc(i)=((Em/8)*(5*((1+2*Bdd*Vcn(i))/(1-Bdd*Vcn(i)))+3*((1+2*(lcn/dcn)*Bdl*Vcn(i))/(1-
Bdl*Vcn(i))))^0.4;
Gmnc(i)=(Emnc(i))/(2*(1+vmnc));

% Young's modulus:
E1130(i)=(Vcf30*E11cf)+(Vmnc(i)*Emnc(i));
E2230(i)=(1)/((Vcf30/E22cf)+(Vmnc(i)/Emnc(i))-
(Vcf30*Vmnc(i))*(((vcf^2)*Emnc(i))/(E22cf))+((vmnc^2)*E22cf)/(Emnc(i))-
(2*vcf*vmnc))/((Vcf30*E22cf)+(Vmnc(i)*Emnc(i))));

% Shear modulus:
G1230(i)=(1)/(((Vcf30)/(G12cf))+((Vmnc(i))/(Gmnc(i))));

% Poison's ratio:
v1230(i)=(Vcf30*vcf)+(Vmnc(i)*vmnc);

% Density:
rhomnc(i)=(Vcn(i)*rhocn)+(Vm(i)*rhom);
rho(i)=(Vcf30*rhocf)+(Vmnc(i)*rhomnc(i));

end

% 45% carbon fibre volume fraction

N=1000;
t=0.2/N;
wcn=0:t:0.2;

for i=1:N+1

% Volume fraction of carbon nanotubes based on mass fraction:
Vm(i)=1-Vcf45-Vcn(i);

% Properties of nanocomposite (CNT & matrix):
Vmnc(i)=Vm(i)+Vcn(i);

```

```

Emnc(i)=(Em/8)*(5*((1+2*Bdd*Vcn(i))/(1-Bdd*Vcn(i)))+3*((1+2*(lcn/dcn)*Bdl*Vcn(i))/(1-
Bdl*Vcn(i))))^0.4;
Gmnc(i)=(Emnc(i))/(2*(1+vmnc));

```

```

% Young's modulus:

```

```

E1145(i)=(Vcf45*E11cf)+(Vmnc(i)*Emnc(i));
E2245(i)=(1)/((Vcf45/E22cf)+(Vmnc(i)/Emnc(i))-
(Vcf45*Vmnc(i))*(((vcf^2)*Emnc(i))/(E22cf))+((vmnc^2)*E22cf)/(Emnc(i))-
(2*vcf*vmnc))/((Vcf45*E22cf)+(Vmnc(i)*Emnc(i))));

```

```

% Shear modulus:

```

```

G1245(i)=(1)/(((Vcf45)/(G12cf))+((Vmnc(i))/(Gmnc(i))));

```

```

% Poison's ratio:

```

```

v1245(i)=(Vcf45*vcf)+(Vmnc(i)*vmnc);

```

```

% Density:

```

```

rhomnc(i)=(Vcn(i)*rhocn)+(Vm(i)*rhom);
rho(i)=(Vcf45*rhocf)+(Vmnc(i)*rhomnc(i));

```

```

end

```

```

% 60% carbon fibre volume fraction

```

```

N=1000;
t=0.2/N;
Vcn=0:t:0.2;

```

```

for i=1:N+1

```

```

% Volume fraction of carbon nanotubes based on mass fraction:

```

```

Vm(i)=1-Vcf60-Vcn(i);

```

```

% Properties of nanocomposite (CNT & matrix):

```

```

Vmnc(i)=Vm(i)+Vcn(i);
Emnc(i)=(Em/8)*(5*((1+2*Bdd*Vcn(i))/(1-Bdd*Vcn(i)))+3*((1+2*(lcn/dcn)*Bdl*Vcn(i))/(1-
Bdl*Vcn(i))))^0.4;
Gmnc(i)=(Emnc(i))/(2*(1+vmnc));

```

```

% Young's modulus:

```

```

E1160(i)=(Vcf60*E11cf)+(Vmnc(i)*Emnc(i));
E2260(i)=(1)/((Vcf60/E22cf)+(Vmnc(i)/Emnc(i))-
(Vcf60*Vmnc(i))*(((vcf^2)*Emnc(i))/(E22cf))+((vmnc^2)*E22cf)/(Emnc(i))-
(2*vcf*vmnc))/((Vcf60*E22cf)+(Vmnc(i)*Emnc(i))));

```

```

% Shear modulus:

```

```

G1260(i)=(1)/(((Vcf60)/(G12cf))+((Vmnc(i))/(Gmnc(i))));

```

```

% Poison's ratio:

```

```

v1260(i)=(Vcf60*vcf)+(Vmnc(i)*vmnc);

```

```

% Density:
rhomnc(i)=(Vcn(i)*rhocn)+(Vm(i)*rhom);
rho(i)=(Vcf60*rhocf)+(Vmnc(i)*rhomnc(i));

end

% 30% carbon fibre volume fraction

N=1000;
t=0.2/N;
Vcn=0:t:0.2;

for i=1:N+1

% Volume fraction of carbon nanotubes based on mass fraction:
Vm(i)=1-Vgf30-Vcn(i);

% Properties of nanocomposite (CNT & matrix):
Vmnc(i)=Vm(i)+Vcn(i);
Emnc(i)=((Em/8)*(5*((1+2*Bdd*Vcn(i))/(1-Bdd*Vcn(i)))+3*((1+2*(lcn/dcn)*Bdl*Vcn(i))/(1-
Bdl*Vcn(i))))^0.4;
Gmnc(i)=(Emnc(i))/(2*(1+vmnc));

% Young's modulus:
E1130gf(i)=(Vgf30*E11gf)+(Vmnc(i)*Emnc(i));
E2230gf(i)=(1)/(((Vgf30/E22gf)+(Vmnc(i)/Emnc(i))-
(Vgf30*Vmnc(i))*(((vgf^2)*Emnc(i))/(E22gf))+(((vmnc^2)*E22gf)/(Emnc(i)))-
(2*vgf*vmnc))/((Vgf30*E22gf)+(Vmnc(i)*Emnc(i))));

% Shear modulus:
G1230gf(i)=(1)/(((Vgf30)/(G12gf))+((Vmnc(i))/(Gmnc(i))));

% Poison's ratio:
v1230gf(i)=(Vgf30*vgf)+(Vmnc(i)*vmnc);

% Density:
rhomnc(i)=(Vcn(i)*rhocn)+(Vm(i)*rhom);
rho(i)=(Vgf30*rhogf)+(Vmnc(i)*rhomnc(i));

end

% 45% carbon fibre volume fraction

N=1000;
t=0.2/N;
wcn=0:t:0.2;

for i=1:N+1

% Volume fraction of carbon nanotubes based on mass fraction:
Vm(i)=1-Vgf45-Vcn(i);

```

% Properties of nanocomposite (CNT & matrix):

```
Vmnc(i)=Vm(i)+Vcn(i);  
Emnc(i)=((Em/8)*(5*((1+2*Bdd*Vcn(i))/(1-Bdd*Vcn(i)))+3*((1+2*(lcn/dcn)*Bdl*Vcn(i))/(1-  
Bdl*Vcn(i))))))^0.4;  
Gmnc(i)=(Emnc(i))/(2*(1+vmnc));
```

% Young's modulus:

```
E1145gf(i)=(Vgf45*E11gf)+(Vmnc(i)*Emnc(i));  
E2245gf(i)=(1)/((Vgf45/E22gf)+(Vmnc(i)/Emnc(i))-  
(Vgf45*Vmnc(i))*(((vgf^2)*Emnc(i))/(E22gf))+(((vmnc^2)*E22gf)/(Emnc(i)))-  
(2*vgf*vmnc))/((Vgf45*E22gf)+(Vmnc(i)*Emnc(i))));
```

% Shear modulus:

```
G1245gf(i)=(1)/(((Vgf45)/(G12gf))+((Vmnc(i))/(Gmnc(i))));
```

% Poison's ratio:

```
v1245gf(i)=(Vgf45*vgf)+(Vmnc(i)*vmnc);
```

% Density:

```
rhomnc(i)=(Vcn(i)*rhocn)+(Vm(i)*rhom);  
rho(i)=(Vgf45*rhogf)+(Vmnc(i)*rhomnc(i));
```

end

% 60% carbon fibre volume fraction

```
N=1000;  
t=0.2/N;  
Vcn=0:t:0.2;
```

```
for i=1:N+1
```

% Volume fraction of carbon nanotubes based on mass fraction:

```
Vm(i)=1-Vgf60-Vcn(i);
```

% Properties of nanocomposite (CNT & matrix):

```
Vmnc(i)=Vm(i)+Vcn(i);  
Emnc(i)=((Em/8)*(5*((1+2*Bdd*Vcn(i))/(1-Bdd*Vcn(i)))+3*((1+2*(lcn/dcn)*Bdl*Vcn(i))/(1-  
Bdl*Vcn(i))))))^0.4;  
Gmnc(i)=(Emnc(i))/(2*(1+vmnc));
```

% Young's modulus:

```
E1160gf(i)=(Vgf60*E11gf)+(Vmnc(i)*Emnc(i));  
E2260gf(i)=(1)/((Vgf60/E22gf)+(Vmnc(i)/Emnc(i))-  
(Vgf60*Vmnc(i))*(((vgf^2)*Emnc(i))/(E22gf))+(((vmnc^2)*E22gf)/(Emnc(i)))-  
(2*vgf*vmnc))/((Vgf60*E22gf)+(Vmnc(i)*Emnc(i))));
```

% Shear modulus:

```
G1260gf(i)=(1)/(((Vgf60)/(G12gf))+((Vmnc(i))/(Gmnc(i))));
```

```

% Poison's ratio:
v1260gf(i)=(Vgf60*vgf)+(Vmnc(i)*vmnc);

% Density:
rhomnc(i)=(Vcn(i)*rhocn)+(Vm(i)*rhom);
rho(i)=(Vgf60*rhogf)+(Vmnc(i)*rhomnc(i));

end

% Outputs

% Graph of effective E11 vs Vcn
figure(1)
plot(Vcn,E1130,'-')
hold on
plot(Vcn,E1145,'--')
plot(Vcn,E1160,'-.')
plot(Vcn,E1130gf,'-')
plot(Vcn,E1145gf,'--')
plot(Vcn,E1160gf,'-.')
hold off
xlabel('\it{V_{CNT}}','FontSize',12)
ylabel('\it{E_{11}} (GPa)','FontSize',12)
legend('30% Carbon fibre','45% Carbon fibre','60% Carbon fibre','30% Glass fibre','45% Glass fibre','60% Glass fibre')
%title('Effective Elastic Modulus')
axis([0 0.2 0 220])

% Graph of effective E22 vs Vcn
figure(2)
plot(Vcn,E2230,'-')
hold on
plot(Vcn,E2245,'--')
plot(Vcn,E2260,'-.')
plot(Vcn,E2230gf,'-')
plot(Vcn,E2245gf,'--')
plot(Vcn,E2260gf,'-.')
hold off
xlabel('\it{V_{CNT}}','FontSize',12)
ylabel('\it{E_{22}} (GPa)','FontSize',12)
legend('30% Carbon fibre','45% Carbon fibre','60% Carbon fibre','30% Glass fibre','45% Glass fibre','60% Glass fibre')
%title('Effective Transverse Modulus')
axis([0 0.2 0 30])

% Graph of effective G12 vs Vcn
figure(3)
plot(Vcn,G1230,'-')
hold on
plot(Vcn,G1245,'--')
plot(Vcn,G1260,'-.')

```

```

plot(Vcn,G1230gf,'-')
plot(Vcn,G1245gf,'--')
plot(Vcn,G1260gf,'-.')
hold off
xlabel('\it{V_{CNT}}','FontSize',12)
ylabel('\it{G_{12}} (GPa)','FontSize',12)
legend('30% Carbon fibre','45% Carbon fibre','60% Carbon fibre','30% Glass fibre','45% Glass fibre','60% Glass fibre')
%title('Effective Shear Modulus')
axis([0 0.2 0 10])

```

% Graph of effective Poisson's ratio vs Vcn

```

figure(4)
plot(Vcn,v1230,'-')
hold on
plot(Vcn,v1245,'--')
plot(Vcn,v1260,'-.')
plot(Vcn,v1230gf,'-')
plot(Vcn,v1245gf,'--')
plot(Vcn,v1260gf,'-.')
hold off
xlabel('\it{V_{CNT}}','FontSize',12)
ylabel('\it{v_{12}}','FontSize',12)
legend('30% Carbon fibre','45% Carbon fibre','60% Carbon fibre','30% Glass fibre','45% Glass fibre','60% Glass fibre')
%title('Effective Poissons Ratio')
axis([0 0.2 0.28 0.42])

```

A.1.4. Effect of nanotube agglomeration on the mechanical properties of three-phase hybrid composites

```
clear all
```

% Effect of carbon nanotube agglomeration

% Inputs (****)

% Carbon nanotube properties (cn):

```

E11cn=1000; % Young's modulus (Gpa)
kr=30; % (GPa)
lr=10; % (GPa)
mr=1; % (GPa)
nr=450; % (GPa)
pr=1; % (GPa)
rhocn=1680; % Mass density (kg/m^3)
%Vcn=; % Volume fraction

```

% Matrix properties (m):

Em=3.5; % Young's modulus (GPa)
 rhom=1200; % Mass density (kg/m³)
 vm=0.4; % Poisson's ratio
 Km=4.95; % Bulk modulus (GPa)
 Gm=1.25; % Shear modulus (GPa)
 %Vm=; % Volume fraction

% Fiber properties (cf):

Vcf30=0.30; % volume fraction at 30%
 Vcf45=0.45; % volume fraction at 45%
 Vcf60=0.60; % volume fraction at 60%
 E11cf=227; % Young's modulus (GPa)
 E22cf=8; % Young's modulus (GPa)
 vcf=0.3; % Poisson's ratio
 G12cf=27.3; % Shear modulus (GPa)
 rhocf=1740; % Mass density (kg/m³)

% Glass fibre properties (gf):

Vgf30=0.30; % Volume fraction at 30%
 Vgf45=0.45; % Volume fraction at 45%
 Vgf60=0.60; % Volume fraction at 60%
 E11gf=73.5; % Young's modulus (GPa)
 E22gf=72; % Young's modulus (GPa)
 vgf=0.22; % Poisson's ratio
 G12gf=33; % Shear modulus (Gpa)
 rhogf=2570; % Mass density (kg/m³)

% Matrix of nanocomposite (mnc) properties:

%Vmnc=; % Volume fraction
 %Emnc=; % Young's modulus (GPa)
 %vmnc=; % Poisson's ratio
 %Gmnc=; % Shear modulus (GPa)
 %rhomnc=; % Mass density (kg/m³)

u=0.5; % Agglomeration parameter
 n=1; % Agglomeration parameter

% Preliminary calculations:

$$ar = \frac{3 \cdot (Km + Gm) + kr - lr}{3 \cdot (Gm + kr)}$$

$$br = \frac{1}{5} \cdot \left(\frac{4 \cdot Gm + 2 \cdot kr + lr}{3 \cdot (Gm + kr)} + \frac{4 \cdot Gm}{Gm + pr} + \frac{2 \cdot (Gm \cdot (3 \cdot Km + Gm) + Gm \cdot (3 \cdot Km + 7 \cdot Gm))}{Gm \cdot (3 \cdot Km + Gm) + mr \cdot (3 \cdot Km + 7 \cdot Gm)} \right)$$

$$dr = \frac{1}{3} \cdot (nr + 2 \cdot lr + \frac{(2 \cdot kr + lr) \cdot (3 \cdot Km + 2 \cdot Gm - lr)}{Gm + kr})$$

$$nnr = \frac{1}{5} \cdot \left(\frac{2}{3} \cdot (nr - lr) + \frac{8 \cdot Gm \cdot pr}{Gm + pr} + \frac{8 \cdot mr \cdot Gm \cdot ((3 \cdot Km) + (4 \cdot Gm))}{3 \cdot Km \cdot (mr + Gm) + Gm \cdot (7 \cdot mr + Gm)} + \frac{2 \cdot (kr - lr) \cdot (2 \cdot Gm + lr)}{3 \cdot (Gm + kr)} \right)$$

% Calculations:

% 30% carbon fibre volume fraction

N=1000;
t=0.2/N;
Vcn=0:t:0.2;

for i=1:N+1

% Volume fraction of matrix:

Vm(i)=1-Vcf30-Vcn(i);

Kin(i)=Km+((Vcn(i)*n*(dr-3*Km*ar))/(3*(u-Vcn(i)*n+Vcn(i)*n*ar)));
Kout(i)=Km+((Vcn(i)*(1-n)*(dr-3*Km*ar))/(3*(1-u-Vcn(i)*(1-n)+Vcn(i)*(1-n)*ar)));
Gin(i)=Gm+((Vcn(i)*n*(nnr-2*Gm*br))/(2*(u-Vcn(i)*n+Vcn(i)*n*br)));
Gout(i)=Gm+((Vcn(i)*(1-n)*(nnr-2*Gm*br))/(2*(1-u-Vcn(i)*(1-n)+Vcn(i)*(1-n)*br)));

vout(i)=((3*Kout(i)-2*Gout(i))/(2*(3*Kout(i)+Gout(i))));
a(i)=(1+vout(i))/(3*(1-vout(i)));
b(i)=(2*(4-5*vout(i)))/(15*(1-vout(i)));

Kmnc(i)=Kout(i)*(1+(u*((Kin(i)/Kout(i))-1))/(1+a(i)*(1-u*((Kin(i)/Kout(i))-1))));
Gmnc(i)=Gout(i)*(1+(u*((Gin(i)/Gout(i))-1))/(1+b(i)*(1-u*((Gin(i)/Gout(i))-1))));

% Properties of nanocomposite (CNT & matrix):

Vmnc(i)=Vm(i)+Vcn(i);
Emnc(i)=(9*Kmnc(i)*Gmnc(i))/(3*Kmnc(i)+Gmnc(i));
vmnc(i)=(3*Kmnc(i)-2*Gmnc(i))/(6*Kmnc(i)+2*Gmnc(i));
Gmnc(i)=(Emnc(i))/(2*(1+vmnc(i)));

% Young's modulus:

E1130(i)=(Vcf30*E11cf)+(Vmnc(i)*Emnc(i));
E2230(i)=(1)/((Vcf30/E22cf)+(Vmnc(i)/Emnc(i))-
(Vcf30*Vmnc(i)*(((vcf^2)*Emnc(i))/(E22cf))+((vmnc(i)^2)*E22cf)/(Emnc(i)))-
(2*vcf*vmnc(i)))/((Vcf30*E22cf)+(Vmnc(i)*Emnc(i))));

% Shear modulus:

G1230(i)=(1)/(((Vcf30)/(G12cf))+((Vmnc(i))/(Gmnc(i))));

% Poison's ratio:

v1230(i)=(Vcf30*vcf)+(Vmnc(i)*vmnc(i));

end

% 45% carbon fibre volume fraction

N=1000;
t=0.2/N;
Vcn=0:t:0.2;

for i=1:N+1

% Volume fraction of matrix:

$V_m(i) = 1 - V_{cf45} - V_{cn}(i);$

$K_{in}(i) = K_m + ((V_{cn}(i) * n * (dr - 3 * K_m * ar)) / (3 * (u - V_{cn}(i) * n + V_{cn}(i) * n * ar)));$

$K_{out}(i) = K_m + ((V_{cn}(i) * (1 - n) * (dr - 3 * K_m * ar)) / (3 * (1 - u - V_{cn}(i) * (1 - n) + V_{cn}(i) * (1 - n) * ar)));$

$G_{in}(i) = G_m + ((V_{cn}(i) * n * (nnr - 2 * G_m * br)) / (2 * (u - V_{cn}(i) * n + V_{cn}(i) * n * br)));$

$G_{out}(i) = G_m + ((V_{cn}(i) * (1 - n) * (nnr - 2 * G_m * br)) / (2 * (1 - u - V_{cn}(i) * (1 - n) + V_{cn}(i) * (1 - n) * br)));$

$v_{out}(i) = ((3 * K_{out}(i) - 2 * G_{out}(i)) / (2 * (3 * K_{out}(i) + G_{out}(i))));$

$a(i) = (1 + v_{out}(i)) / (3 * (1 - v_{out}(i)));$

$b(i) = (2 * (4 - 5 * v_{out}(i))) / (15 * (1 - v_{out}(i)));$

$K_{mnc}(i) = K_{out}(i) * (1 + (u * ((K_{in}(i) / K_{out}(i)) - 1)) / (1 + a(i) * (1 - u) * ((K_{in}(i) / K_{out}(i)) - 1)));$

$G_{mnc}(i) = G_{out}(i) * (1 + (u * ((G_{in}(i) / G_{out}(i)) - 1)) / (1 + b(i) * (1 - u) * ((G_{in}(i) / G_{out}(i)) - 1)));$

% Properties of nanocomposite (CNT & matrix):

$V_{mnc}(i) = V_m(i) + V_{cn}(i);$

$E_{mnc}(i) = (9 * K_{mnc}(i) * G_{mnc}(i)) / (3 * K_{mnc}(i) + G_{mnc}(i));$

$v_{mnc}(i) = (3 * K_{mnc}(i) - 2 * G_{mnc}(i)) / (6 * K_{mnc}(i) + 2 * G_{mnc}(i));$

$G_{mnc}(i) = (E_{mnc}(i)) / (2 * (1 + v_{mnc}(i)));$

% Young's modulus:

$E_{1145}(i) = (V_{cf45} * E_{11cf}) + (V_{mnc}(i) * E_{mnc}(i));$

$E_{2245}(i) = (1) / (((V_{cf45} / E_{22cf}) + (V_{mnc}(i) / E_{mnc}(i)) -$

$(V_{cf45} * V_{mnc}(i)) * (((v_{cf}^2 * E_{mnc}(i)) / (E_{22cf})) + (((v_{mnc}(i))^2 * E_{22cf}) / (E_{mnc}(i))) -$

$(2 * v_{cf} * v_{mnc}(i))) / ((V_{cf45} * E_{22cf}) + (V_{mnc}(i) * E_{mnc}(i))));$

% Shear modulus:

$G_{1245}(i) = (1) / (((V_{cf45} / (G_{12cf})) + (V_{mnc}(i) / (G_{mnc}(i))));$

% Poison's ratio:

$v_{1245}(i) = (V_{cf45} * v_{cf}) + (V_{mnc}(i) * v_{mnc}(i));$

end

% 60% carbon fibre volume fraction

N=1000;

t=0.2/N;

Vcn=0:t:0.2;

for i=1:N+1

% Volume fraction of matrix:

$V_m(i) = 1 - V_{cf60} - V_{cn}(i);$

$K_{in}(i) = K_m + ((V_{cn}(i) * n * (dr - 3 * K_m * ar)) / (3 * (u - V_{cn}(i) * n + V_{cn}(i) * n * ar)));$

$K_{out}(i) = K_m + ((V_{cn}(i) * (1 - n) * (dr - 3 * K_m * ar)) / (3 * (1 - u - V_{cn}(i) * (1 - n) + V_{cn}(i) * (1 - n) * ar)));$

$G_{in}(i) = G_m + ((V_{cn}(i) * n * (nnr - 2 * G_m * br)) / (2 * (u - V_{cn}(i) * n + V_{cn}(i) * n * br)));$

$G_{out}(i) = G_m + ((V_{cn}(i) * (1 - n) * (nnr - 2 * G_m * br)) / (2 * (1 - u - V_{cn}(i) * (1 - n) + V_{cn}(i) * (1 - n) * br)));$

```

vout(i)=((3*Kout(i)-2*Gout(i))/(2*(3*Kout(i)+Gout(i)));
a(i)=(1+vout(i))/(3*(1-vout(i)));
b(i)=(2*(4-5*vout(i)))/(15*(1-vout(i)));

Kmnc(i)=Kout(i)*(1+(u*((Kin(i)/Kout(i))-1))/(1+a(i)*(1-u)*((Kin(i)/Kout(i))-1)));
Gmnc(i)=Gout(i)*(1+(u*((Gin(i)/Gout(i))-1))/(1+b(i)*(1-u)*((Gin(i)/Gout(i))-1)));

% Properties of nanocomposite (CNT & matrix):
Vmnc(i)=Vm(i)+Vcn(i);
Emnc(i)=(9*Kmnc(i)*Gmnc(i))/(3*Kmnc(i)+Gmnc(i));
vmnc(i)=(3*Kmnc(i)-2*Gmnc(i))/(6*Kmnc(i)+2*Gmnc(i));
Gmnc(i)=(Emnc(i))/(2*(1+vmnc(i)));

% Young's modulus:
E1160(i)=(Vcf60*E11cf)+(Vmnc(i)*Emnc(i));
E2260(i)=(1)/((Vcf60/E22cf)+(Vmnc(i)/Emnc(i))-
(Vcf60*Vmnc(i)*(((vcf^2)*Emnc(i))/(E22cf))+((vmnc(i)^2)*E22cf)/(Emnc(i)))-
(2*vcf*vmnc(i)))/((Vcf60*E22cf)+(Vmnc(i)*Emnc(i)));

% Shear modulus:
G1260(i)=(1)/(((Vcf60)/(G12cf))+((Vmnc(i))/(Gmnc(i))));

% Poison's ratio:
v1260(i)=(Vcf60*vcf)+(Vmnc(i)*vmnc(i));

end

% 30% carbon fibre volume fraction

N=1000;
t=0.2/N;
Vcn=0:t:0.2;

for i=1:N+1

% Volume fraction of matrix:
Vm(i)=1-Vgf30-Vcn(i);

Kin(i)=Km+((Vcn(i)*n*(dr-3*Km*ar))/(3*(u-Vcn(i)*n+Vcn(i)*n*ar)));
Kout(i)=Km+((Vcn(i)*(1-n)*(dr-3*Km*ar))/(3*(1-u-Vcn(i)*(1-n)+Vcn(i)*(1-n)*ar)));
Gin(i)=Gm+((Vcn(i)*n*(nnr-2*Gm*br))/(2*(u-Vcn(i)*n+Vcn(i)*n*br)));
Gout(i)=Gm+((Vcn(i)*(1-n)*(nnr-2*Gm*br))/(2*(1-u-Vcn(i)*(1-n)+Vcn(i)*(1-n)*br)));

vout(i)=((3*Kout(i)-2*Gout(i))/(2*(3*Kout(i)+Gout(i)));
a(i)=(1+vout(i))/(3*(1-vout(i)));
b(i)=(2*(4-5*vout(i)))/(15*(1-vout(i)));

Kmnc(i)=Kout(i)*(1+(u*((Kin(i)/Kout(i))-1))/(1+a(i)*(1-u)*((Kin(i)/Kout(i))-1)));
Gmnc(i)=Gout(i)*(1+(u*((Gin(i)/Gout(i))-1))/(1+b(i)*(1-u)*((Gin(i)/Gout(i))-1)));

```

```

% Properties of nanocomposite (CNT & matrix):
Vmnc(i)=Vm(i)+Vcn(i);
Emnc(i)=(9*Kmnc(i)*Gmnc(i))/(3*Kmnc(i)+Gmnc(i));
vmnc(i)=(3*Kmnc(i)-2*Gmnc(i))/(6*Kmnc(i)+2*Gmnc(i));
Gmnc(i)=(Emnc(i))/(2*(1+vmnc(i)));

% Young's modulus:
E1130gf(i)=(Vgf30*E11gf)+(Vmnc(i)*Emnc(i));
E2230gf(i)=(1)/((Vgf30/E22gf)+(Vmnc(i)/Emnc(i))-
(Vgf30*Vmnc(i))*(((Vgf^2)*Emnc(i))/(E22gf))+(((vmnc(i)^2)*E22gf)/(Emnc(i)))-
(2*vgf*vmnc(i)))/((Vgf30*E22gf)+(Vmnc(i)*Emnc(i))));

% Shear modulus:
G1230gf(i)=(1)/(((Vgf30)/(G12gf))+((Vmnc(i))/(Gmnc(i))));

% Poison's ratio:
v1230gf(i)=(Vgf30*vgf)+(Vmnc(i)*vmnc(i));

end

% 45% carbon fibre volume fraction

N=1000;
t=0.2/N;
Vcn=0:t:0.2;

for i=1:N+1

% Volume fraction of matrix:
Vm(i)=1-Vgf45-Vcn(i);

Kin(i)=Km+((Vcn(i)*n*(dr-3*Km*ar))/(3*(u-Vcn(i)*n+Vcn(i)*n*ar)));
Kout(i)=Km+((Vcn(i)*(1-n)*(dr-3*Km*ar))/(3*(1-u-Vcn(i)*(1-n)+Vcn(i)*(1-n)*ar)));
Gin(i)=Gm+((Vcn(i)*n*(nnr-2*Gm*br))/(2*(u-Vcn(i)*n+Vcn(i)*n*br)));
Gout(i)=Gm+((Vcn(i)*(1-n)*(nnr-2*Gm*br))/(2*(1-u-Vcn(i)*(1-n)+Vcn(i)*(1-n)*br)));

vout(i)=((3*Kout(i)-2*Gout(i)))/(2*(3*Kout(i)+Gout(i)));
a(i)=(1+vout(i))/(3*(1-vout(i)));
b(i)=(2*(4-5*vout(i)))/(15*(1-vout(i)));

Kmnc(i)=Kout(i)*(1+(u*((Kin(i)/Kout(i))-1))/(1+a(i)*(1-u)*((Kin(i)/Kout(i))-1)));
Gmnc(i)=Gout(i)*(1+(u*((Gin(i)/Gout(i))-1))/(1+b(i)*(1-u)*((Gin(i)/Gout(i))-1)));

% Properties of nanocomposite (CNT & matrix):
Vmnc(i)=Vm(i)+Vcn(i);
Emnc(i)=(9*Kmnc(i)*Gmnc(i))/(3*Kmnc(i)+Gmnc(i));
vmnc(i)=(3*Kmnc(i)-2*Gmnc(i))/(6*Kmnc(i)+2*Gmnc(i));
Gmnc(i)=(Emnc(i))/(2*(1+vmnc(i)));

% Young's modulus:
E1145gf(i)=(Vgf45*E11gf)+(Vmnc(i)*Emnc(i));

```

```

E2245gf(i)=(1)/((Vgf45/E22gf)+(Vmnc(i)/Emnc(i))-
(Vgf45*Vmnc(i))*(((vgf^2)*Emnc(i))/(E22gf))+(((vmnc(i)^2)*E22gf)/(Emnc(i)))-
(2*vgf*vmnc(i)))/((Vgf45*E22gf)+(Vmnc(i)*Emnc(i))));

% Shear modulus:
G1245gf(i)=(1)/(((Vgf45)/(G12gf))+((Vmnc(i))/(Gmnc(i))));

% Poison's ratio:
v1245gf(i)=(Vgf45*vgf)+(Vmnc(i)*vmnc(i));

end

% 60% carbon fibre volume fraction

N=1000;
t=0.2/N;
Vcn=0:t:0.2;

for i=1:N+1

% Volume fraction of matrix:
Vm(i)=1-Vgf60-Vcn(i);

Kin(i)=Km+((Vcn(i)*n*(dr-3*Km*ar))/(3*(u-Vcn(i)*n+Vcn(i)*n*ar)));
Kout(i)=Km+((Vcn(i)*(1-n)*(dr-3*Km*ar))/(3*(1-u-Vcn(i)*(1-n)+Vcn(i)*(1-n)*ar)));
Gin(i)=Gm+((Vcn(i)*n*(nnr-2*Gm*br))/(2*(u-Vcn(i)*n+Vcn(i)*n*br)));
Gout(i)=Gm+((Vcn(i)*(1-n)*(nnr-2*Gm*br))/(2*(1-u-Vcn(i)*(1-n)+Vcn(i)*(1-n)*br)));

vout(i)=((3*Kout(i)-2*Gout(i))/(2*(3*Kout(i)+Gout(i)));
a(i)=(1+vout(i))/(3*(1-vout(i)));
b(i)=(2*(4-5*vout(i)))/(15*(1-vout(i)));

Kmnc(i)=Kout(i)*(1+(u*((Kin(i)/Kout(i))-1))/(1+a(i)*(1-u)*((Kin(i)/Kout(i))-1)));
Gmnc(i)=Gout(i)*(1+(u*((Gin(i)/Gout(i))-1))/(1+b(i)*(1-u)*((Gin(i)/Gout(i))-1)));

% Properties of nanocomposite (CNT & matrix):
Vmnc(i)=Vm(i)+Vcn(i);
Emnc(i)=(9*Kmnc(i)*Gmnc(i))/(3*Kmnc(i)+Gmnc(i));
vmnc(i)=(3*Kmnc(i)-2*Gmnc(i))/(6*Kmnc(i)+2*Gmnc(i));
Gmnc(i)=(Emnc(i))/(2*(1+vmnc(i)));

% Young's modulus:
E1160gf(i)=(Vgf60*E11gf)+(Vmnc(i)*Emnc(i));
E2260gf(i)=(1)/((Vgf60/E22gf)+(Vmnc(i)/Emnc(i))-
(Vgf60*Vmnc(i))*(((vgf^2)*Emnc(i))/(E22gf))+(((vmnc(i)^2)*E22gf)/(Emnc(i)))-
(2*vgf*vmnc(i)))/((Vgf60*E22gf)+(Vmnc(i)*Emnc(i))));

% Shear modulus:
G1260gf(i)=(1)/(((Vgf60)/(G12gf))+((Vmnc(i))/(Gmnc(i))));

% Poison's ratio:

```

```
v1260gf(i)=(Vgf60*vgf)+(Vmnc(i)*vmnc(i));
```

```
end
```

```
% Outputs
```

```
% Graph of effective E11 vs Vcn
```

```
figure(1)
```

```
plot(Vcn,E1130,'-')
```

```
hold on
```

```
plot(Vcn,E1145,'--')
```

```
plot(Vcn,E1160,'-.')
```

```
plot(Vcn,E1130gf,'-')
```

```
plot(Vcn,E1145gf,'--')
```

```
plot(Vcn,E1160gf,'-.')
```

```
hold off
```

```
xlabel('\it{V}_{CNT}','FontSize',12)
```

```
ylabel('\it{E}_{11} (GPa)','FontSize',12)
```

```
legend('30% Carbon fibre','45% Carbon fibre','60% Carbon fibre','30% Glass fibre','45% Glass fibre','60% Glass fibre')
```

```
%title('Effective Elastic Modulus')
```

```
axis([0 0.2 0 220])
```

```
% Graph of effective E22 vs Vcn
```

```
figure(2)
```

```
plot(Vcn,E2230,'-')
```

```
hold on
```

```
plot(Vcn,E2245,'--')
```

```
plot(Vcn,E2260,'-.')
```

```
plot(Vcn,E2230gf,'-')
```

```
plot(Vcn,E2245gf,'--')
```

```
plot(Vcn,E2260gf,'-.')
```

```
hold off
```

```
xlabel('\it{V}_{CNT}','FontSize',12)
```

```
ylabel('\it{E}_{22} (GPa)','FontSize',12)
```

```
legend('30% Carbon fibre','45% Carbon fibre','60% Carbon fibre','30% Glass fibre','45% Glass fibre','60% Glass fibre')
```

```
%title('Effective Transverse Modulus')
```

```
axis([0 0.2 0 20])
```

```
% Graph of effective G12 vs Vcn
```

```
figure(3)
```

```
plot(Vcn,G1230,'-')
```

```
hold on
```

```
plot(Vcn,G1245,'--')
```

```
plot(Vcn,G1260,'-.')
```

```
plot(Vcn,G1230gf,'-')
```

```
plot(Vcn,G1245gf,'--')
```

```
plot(Vcn,G1260gf,'-.')
```

```
hold off
```

```
xlabel('\it{V}_{CNT}','FontSize',12)
```

```

ylabel('\it{G}_{12}} (GPa)', 'FontSize', 12)
legend('30% Carbon fibre', '45% Carbon fibre', '60% Carbon fibre', '30% Glass fibre', '45% Glass fibre', '60% Glass fibre')
%title('Effective Shear Modulus')
axis([0 0.2 1 7])

% Graph of effective Poisson's ratio vs Vcn
figure(4)
plot(Vcn, v1230, '-.')
hold on
plot(Vcn, v1245, '-.')
plot(Vcn, v1260, '-.')
plot(Vcn, v1230gf, '-.')
plot(Vcn, v1245gf, '-.')
plot(Vcn, v1260gf, '-.')
hold off
xlabel('\it{V}_{CNT}}', 'FontSize', 12)
ylabel('\it{v}_{12}}', 'FontSize', 12)
legend('30% Carbon fibre', '45% Carbon fibre', '60% Carbon fibre', '30% Glass fibre', '45% Glass fibre', '60% Glass fibre')
%title('Effective Poissons Ratio')
axis([0 0.2 0.25 0.4])

```

A.1.5. Fibre reinforced deflection contour for increasing reinforcement volume

fraction (randomly orientated CNT)

```

clear all

% Inputs

% Carbon nanotube properties (cn):

lcn=8.5e-6; % Length (m)
dcn=8e-9; % Outer diameter (m)
tcn=0.8e-9; % Thickness (m)
E11cn=1000; % Young's modulus (GPa)
rhocn=1680; % Mass density (kg/m^3)
%Vcn=; % Volume fraction
%wcn=; % Mass fraction

% Matrix properties (m):

Em=3.5; % Young's modulus (GPa)
rhom=1200; % Mass density (kg/m^3)
vm=0.4; % Poisson's ratio
%Vm=; % Volume fraction

% Fibre properties (cf):

%Vcf=0.30; % Volume fraction

```

```

%E11cf=227; % Young's modulus (GPa)
%E22cf=8; % Young's modulus (GPa)
%vcf=0.3; % Poisson's ratio
%G12cf=27.3; % Shear modulus (Gpa)
%rhocf=1740; % Mass density (kg/m^3)

% Glass fibre properties (gf):

%Vgf=0.30; % Volume fraction at 30%
E11cf=73.5; % Young's modulus (GPa)
E22cf=72; % Young's modulus (GPa)
vcf=0.22; % Poisson's ratio
G12cf=33; % Shear modulus (Gpa)
rhocf=2570; % Mass density (kg/m^3)

% Matrix of nanocomposite (mnc) properties:

%Vmnc=; % Volume fraction
%Emnc=; % Young's modulus (GPa)
%vmnc=; % Poisson's ratio
%Gmnc=; % Shear modulus (GPa)
%rhomnc=; % Mass density (kg/m^3)

% Laminate properties:

M=8; % no of layers

orient=[pi/2 0 pi/2 0 pi/2 0 pi/2 0]; % orientation

h=[-0.5 -0.375 -0.25 -0.125 0 0.125 0.25 0.375 0.5]; % thickness

% Beam properties:

P=1; %force[N]
L=1; %length [mm]
bredth=1; %bredth [mm]
r=L/bredth;

% Preliminary calculations:

Bdl=(((E11cn/Em)-(dcn/4*tcn))/((E11cn/Em)+(lcn/2*tcn)));
Bdd=(((E11cn/Em)-(dcn/4*tcn))/((E11cn/Em)+(dcn/2*tcn)));
vmnc=vm;

% Calculations

N=1000;
t=0.2/N;
Vcn=0:t:0.2;

for i=1:N+1

```

```

N=1000;
t=0.6/N;
Vcf=0:t:0.6;

for k=1:N+1

% Volume fraction of matrix:
Vm(k,i)=1-Vcf(k)-Vcn(i);

% Properties of nanocomposite (CNT & matrix):
Vmnc(k,i)=Vm(k,i)+Vcn(i);
Emnc(k,i)=((Em/8)*(5*((1+2*Bdd*Vcn(i))/(1-Bdd*Vcn(i)))+3*((1+2*(lcn/dcn)*Bdl*Vcn(i))/(1-
Bdl*Vcn(i))))^0.4;
Gmnc(k,i)=(Emnc(k,i))/(2*(1+vmnc));

% Young's modulus:
E11(k,i)=(Vcf(k)*E11cf)+(Vmnc(k,i)*Emnc(k,i));
E22(k,i)=(1)/((Vcf(k)/E22cf)+(Vmnc(k,i)/Emnc(k,i))-
(Vcf(k)*Vmnc(k,i))*(((vcf^2)*Emnc(k,i))/(E22cf))+(((vmnc^2)*E22cf)/(Emnc(k,i)))-
(2*vcf*vmnc))/((Vcf(k)*E22cf)+(Vmnc(k,i)*Emnc(k,i))));

% Shear modulus:
G12(k,i)=(1)/(((Vcf(k))/(G12cf))+((Vmnc(k,i))/(Gmnc(k,i))));

% Poison's ratio:
v12(k,i)=(Vcf(k)*vcf)+(Vmnc(k,i)*vmnc);
v21(k,i)=(v12(k,i))*(E22(k,i)/E11(k,i));

% Laminate calculations:
Q11=E11(k,i)/(1-(v12(k,i)*v21(k,i)));
Q22=E22(k,i)/(1-(v12(k,i)*v21(k,i)));
Q12=v21(k,i)*E11(k,i)/(1-(v12(k,i)*v21(k,i)));
Q33=G12(k,i);
Qtheta0=[Q11 Q12 0; Q12 Q22 0; 0 0 Q33];

for j=1:M

theta=orient(j);
m=cos(theta);
n=sin(theta);

T=[m^2 n^2 2*m*n; n^2 m^2 -2*m*n; -m*n m*n m^2-n^2];R=[1 0 0;0 1 0;0 0 2];
Qtheta=(T^-1)*Qtheta0*R*T*(R^-1);

d11(j)=(Qtheta(1,1))*(h(j+1)^3-h(j)^3);
d12(j)=(Qtheta(1,2))*(h(j+1)^3-h(j)^3);
d13(j)=(Qtheta(1,3))*(h(j+1)^3-h(j)^3);
d21(j)=(Qtheta(2,1))*(h(j+1)^3-h(j)^3);
d22(j)=(Qtheta(2,2))*(h(j+1)^3-h(j)^3);
d23(j)=(Qtheta(2,3))*(h(j+1)^3-h(j)^3);

```

```

d31(j)=(Qthetal(3,1))*(h(j+1)^3-h(j)^3);
d32(j)=(Qthetal(3,2))*(h(j+1)^3-h(j)^3);
d33(j)=(Qthetal(3,3))*(h(j+1)^3-h(j)^3);
end

D(1,1)=sum(d11)/3;
D(1,2)=sum(d12)/3;
D(1,3)=sum(d13)/3;
D(2,1)=sum(d21)/3;
D(2,2)=sum(d22)/3;
D(2,3)=sum(d23)/3;
D(3,1)=sum(d31)/3;
D(3,2)=sum(d32)/3;
D(3,3)=sum(d33)/3;
Dstar(1,1)=D(1,1)*M^4+2*(D(1,2)+2*D(3,3))*(M*N*r)^2+D(2,2)*(N*r)^4;

% Plate deflection:

wc(k,i)=P*L^4/(pi^4*Dstar(1,1));
wcc(k,i)=wc(k,i)/(7.114e-14);
wwcc(k,i)=wcc(k,i);
Vcnn(k,i)=Vcn(i);
Vcff(k,i)=Vcf(k);

end
end

% Display
figure(1)
v=[0.025 0.03 0.04 0.05 0.06 0.08 0.1 0.15 0.2];
[C,h] = contour(Vcnn,Vcff,wwcc,v)
clabel(C,h,'manual')
xlabel('\it{V_{CNT}}')
ylabel('\it{V_{F}}')
legend('\it{w_{c}} / w_{0}')
%title('Graph of deflection for increasing glass reinforcement')
plottedit on

```

A.1.6. Effect of nanotube diameter on the mechanical properties of a reinforced structural element

```
clear all
```

```
% Inputs
```

```
% Carbon nanotube properties (cn):
```

```
lcn=8.5e-6; % Length (m)
%dcn=8e-9; % Outer diameter (m)
tcn=0.8e-9; % Thickness (m)
```

```
E11cn=1000; % Young's modulus (GPa)
rhocn=1680; % Mass density (kg/m^3)
%Vcn=; % Volume fraction
%wcn=; % Mass fraction
```

```
% Matrix properties (m):
```

```
Em=3.5; % Young's modulus (GPa)
rhom=1200; % Mass density (kg/m^3)
vm=0.4; % Poisson's ratio
%Vm=; % Volume fraction
```

```
% Fibre properties (cf):
```

```
%Vcf=0.45; % Volume fraction at 30%
%E11cf=227; % Young's modulus (GPa)
%E22cf=8; % Young's modulus (GPa)
%vcf=0.3; % Poisson's ratio
%G12cf=27.3; % Shear modulus (Gpa)
%rhocf=1740; % Mass density (kg/m^3)
```

```
% Glass fibre properties (gf):
```

```
Vcf=0.45; % Volume fraction at 30%
E11cf=73.5; % Young's modulus (GPa)
E22cf=72; % Young's modulus (GPa)
vcf=0.22; % Poisson's ratio
G12cf=33; % Shear modulus (Gpa)
rhocf=2570; % Mass density (kg/m^3)
```

```
% Matrix of nanocomposite (mnc) properties:
```

```
%Vmnc=; % Volume fraction
%Emnc=; % Young's modulus (GPa)
%vmnc=; % Poisson's ratio
%Gmnc=; % Shear modulus (GPa)
%rhomnc=; % Mass density (kg/m^3)
```

```
% Laminate properties:
```

```
M=8; % no of layers
```

```
orientt=[pi/2 0 pi/2 0 pi/2 0 pi/2 0]; % orientation
```

```
h=[-0.5 -0.375 -0.25 -0.125 0 0.125 0.25 0.375 0.5]; % thickness
```

```
dcn=[2.0e-9; 6.1e-9; 10.1e-9; 14.0e-9; 18.2e-9; 22.3e-9]; % nanotube diameter
```

```
% Beam properties:
```

```
P=1; %force[N]
```

```

L=1; %length [mm]
bredth=1; %bredth [mm]
r=L/bredth;

% Preliminary calculations:

vmnc=vm;

% Calculations

N=1000;
t=0.2/N;
Vcn=0:t:0.2;

for k=1:6

dcnn=dcn(k,:);

for i=1:N+1

% Volume fraction of matrix:
Vm(i)=1-Vcf-Vcn(i);

% Variable calculations:
Bdl=(((E11cn/Em)-(dcnn/4*tcn))/((E11cn/Em)+(lcn/2*tcn)));
Bdd=(((E11cn/Em)-(dcnn/4*tcn))/((E11cn/Em)+(dcnn/2*tcn)));

% Properties of nanocomposite (CNT & matrix):
Vmnc(i)=Vm(i)+Vcn(i);
Emnc(i)=((Em/8)*(5*((1+2*Bdd*Vcn(i))/(1-Bdd*Vcn(i)))+3*((1+2*(lcn/dcnn)*Bdl*Vcn(i))/(1-Bdl*Vcn(i))))^0.4;
Gmnc(i)=(Emnc(i))/(2*(1+vmnc));

% Young's modulus:
E11(i)=(Vcf*E11cf)+(Vmnc(i)*Emnc(i));
E22(i)=(1)/((Vcf/E22cf)+(Vmnc(i)/Emnc(i))-
(Vcf*Vmnc(i))*((((vcf^2)*Emnc(i))/(E22cf))+(((vmnc^2)*E22cf)/(Emnc(i)))-
(2*vcf*vmnc))/((Vcf*E22cf)+(Vmnc(i)*Emnc(i))));

% Shear modulus:
G12(i)=(1)/(((Vcf)/(G12cf))+((Vmnc(i))/(Gmnc(i))));

% Poison's ratio:
v12(i)=(Vcf*vcf)+(Vmnc(i)*vmnc);
v21(i)=(v12(i))*(E22(i)/E11(i));

% Laminate calculations:
Q11=E11(i)/(1-(v12(i)*v21(i)));
Q22=E22(i)/(1-(v12(i)*v21(i)));
Q12=v21(i)*E11(i)/(1-(v12(i)*v21(i)));
Q33=G12(i);

```

```

Qtheta0=[Q11 Q12 0; Q12 Q22 0; 0 0 Q33];

for j=1:M

theta=orientt(j);
m=cos(theta);
n=sin(theta);

T=[m^2 n^2 2*m*n; n^2 m^2 -2*m*n; -m*n m*n m^2-n^2];R=[1 0 0;0 1 0;0 0 2];
Qthetal=(T^-1)*Qtheta0*R*T*(R^-1);

d11(j)=(Qthetal(1,1))*(h(j+1)^3-h(j)^3);
d12(j)=(Qthetal(1,2))*(h(j+1)^3-h(j)^3);
d13(j)=(Qthetal(1,3))*(h(j+1)^3-h(j)^3);
d21(j)=(Qthetal(2,1))*(h(j+1)^3-h(j)^3);
d22(j)=(Qthetal(2,2))*(h(j+1)^3-h(j)^3);
d23(j)=(Qthetal(2,3))*(h(j+1)^3-h(j)^3);
d31(j)=(Qthetal(3,1))*(h(j+1)^3-h(j)^3);
d32(j)=(Qthetal(3,2))*(h(j+1)^3-h(j)^3);
d33(j)=(Qthetal(3,3))*(h(j+1)^3-h(j)^3);
end

D(1,1)=sum(d11)/3;
D(1,2)=sum(d12)/3;
D(1,3)=sum(d13)/3;
D(2,1)=sum(d21)/3;
D(2,2)=sum(d22)/3;
D(2,3)=sum(d23)/3;
D(3,1)=sum(d31)/3;
D(3,2)=sum(d32)/3;
D(3,3)=sum(d33)/3;
Dstar(1,1)=D(1,1)*M^4+2*(D(1,2)+2*D(3,3))*(M*N*r)^2+D(2,2)*(N*r)^4;

% Plate deflection:

wc(i)=P*L^4/(pi^4*Dstar(1,1));
wcc(i)=wc(i)/(7.114e-14);
wwcc(k,i)=wcc(i);
%Vcnn(i)=Vcn(i);

end
end

dc=dcn(k,:);

% Display
figure(1)
%v=[0.001 0.01 0.1 0.5 1 10];
plot(Vcn,wwcc(1,:),'-')
hold on
plot(Vcn,wwcc(2,:),'-')

```

```
plot(Vcn,wwcc(3,:),':')
plot(Vcn,wwcc(4,:),'-.')
plot(Vcn,wwcc(5,:),'-.-')
plot(Vcn,wwcc(6,:),'-')
hold off
xlabel('\it{V_{CNT}}','FontSize',12)
ylabel('\it{w_{c} / w_{0}}','FontSize',12)
%title('Effect of nanotube diameter on glass fibre composite')
legend('2.0nm', '6.1nm', '10.1nm', '14.0nm', '18.2nm', '22.3nm')
plottedit on
```